The Gas-Phase Ligand Exchange of Palladium β-diketonate Complexes

by

Jennifer Christina Pekar

Submitted in Partial Fulfillment of the Requirements

for the Degree of

Master of Science

in the

Chemistry

Program

YOUNGSTOWN STATE UNIVERSITY

August 2014

The Gas-Phase Ligand Exchange of Palladium β-diketonate Complexes

Jennifer Christina Pekar

I hereby release this thesis to the public. I understand that this thesis will be made available from the OhioLINK ETD Center and the Maag Library Circulation Desk for public access. I also authorize the University or other individuals to make copies of this thesis as needed for scholarly research.

Signature:

Jennifer C. Pekar, Student Date

Approvals:

Dr. Brian D. Leskiw, Thesis Advisor Date

Dr. Howard D. Mettee, Committee Member Date

Dr. Ganesaratnam K. Balendiran, Committee Member Date

Dr. Salvatore A. Sanders, Associate Dean of Graduate Studies Date

Abstract

A series of gas-phase reactions were performed via co-sublimation using a triple quadrupole electron impact mass spectrometer. Novel palladium β-diketonate complexes, along with several other species containing different metals and ligands were synthesized and observed to readily undergo ligand exchange in the gas phase and are reported herein for the first time. Selective reactions were also conducted involving Pd and Ni complexes utilizing the collision cell of the mass spectrometer as a reaction vessel. Results from these gas-phase reactions shed light on the mechanism of ligand exchange for this class of metal β-diketonate complexes.

Acknowledgements

First and foremost I would like to thank God, my family, and friends for their constant support through graduate school and all of my life. It has taken a lot of hard work and dedication to get where I am today and I could not have done it without their support.

I would also like to thank the YSU chemistry department for the knowledge I have gained in the Master's program and in life. My acceptance and completion of this program has opened many career opportunities for me that I would not have previously had.

Dr. Brian Leskiw deserves a multitude of thanks for being such a supportive and helpful advisor. He took extra time to help me and my colleagues through this process without question. His criticism and motivation was essential in the production of this final work.

I would also like to thank my committee members, Dr. Howard Mettee, and Dr. Ganesaratnam Balendiran for their support and time in my thesis preparation and presentation.

Finally, I would like to thank Ray Hoff and Dr. Wang for their assistance with all of the instrumental issues experienced in this process.

Table of Contents

List of Figures

List of Tables

List of Equations

Chapter 1: Literature Review

1.1 β-Diketonate Compounds

β-diketonate complexes are coordination compounds that are highly studied, versatile, and are used in an array of different scientific fields. More specifically, metal β-diketonate complexes are used in the production and vapor deposition of thin films[1] as well as the general catalysis of a multitude of different chemical[2,3] and biological[4] reactions. In recent years, these valuable compounds have even been utilized in influencing how molecules bind to DNA[5], facilitate reactions that remove heavy metals from water[6], and help to create compounds that readily luminesce.[7]

β-diketone complexes bound with azomethine nitrogen and phenolic oxygen have been observed to assist in DNA binding.[5] These β-diketone-Schiff base complexes were synthesized in the lab containing different metal centers such as Ni(II), Cu(II), Co(II), Zn(II), and VO(IV). Once synthesized and characterized by FAB-MS (fast atom bombardment), the compounds were analyzed for their binding affinity to calf thymus DNA (CT-DNA) using electronic absorption spectroscopy. The authors reported that all of the complexes, except for the VO(IV) complex, showed significant binding affinity to the CT-DNA. These findings may provide insight on the ability of a new class of compounds binding to DNA and become a stepping stone to creating new DNA cleaving agents.

Another group found that polyvinyl chloride (PVC) could be heat stabilized by binding β-diketonates with calcium stearate.[8] Results of this study showed that the natural stability of PVC was enhanced upon the addition of the β-diketonate component. $HCl_{(aq)}$

absorption was also enhanced, which is also essential in the overall stability of PVC and was confirmed by X-Ray diffraction. With PVC being utilized in countless applications, the ability of β-diketonates to improve the function of this material can have substantial implications in an array of applications.

β-diketonates have also previously been shown to remove heavy metals from water. Kumar et.al.[6] showed that by using β-diketonate functionalized styrene molecules, heavy metals such as nickel, chromium, and lead were able to be removed from water. The team investigated the effectiveness of these compounds on the removal of heavy metals from water by measuring the kinetic absorption reactions of these complexes as a function of these heavy metals. Each heavy metal was effectively removed using the functionalized styrene and gives rise to the potential application of β-diketonates to environmental chemistry and environmental health.

Frangoza-Mar et. al.[9] investigated the anti-corrosive properties of a 1,3-diketone malonate compound. After synthesis of these compounds, they were solvated in a mild solution of diluted $HCl_{(aq)}$ and placed on a small sample of mild steel in a static, oxygen containing environment. Another control sample of steel was placed in the same environment without the inhibitor mixture. Corrision inhibition was measured on both samples by gravimetric (weight loss) analysis, electrochemical tests, as well as Scanning Electron Microscopy (SEM). Results confirmed that the steel sample exposed to the 1,3-diketone malonate compound did indeed have a corrosion inhibition efficiency of approximately 75-96% from both the keto and enol forms of the tautonomer.

As the studies of β-diketonates continue to evolve, there will surely be many more useful applications for this already versatile group of compounds, making this study and the ones to follow of great importance in several areas of interest.

1.2 Coordination Compounds

Coordination compounds, like metal β-diketonate complexes, are typically inorganic species that can be described as a metal atom(s) covalently bonded to one or more ligands. The behavior of coordination compounds is characteristic Lewis acid/Lewis base chemistry. The ligand portion of a coordination compound is typically an anion or polar organic species with the presence of an acidic hydrogen. The ligand behaves as a Lewis base (electron donor) while the metal center behaves as the Lewis acid (electron acceptor). The overall stability of this class of coordination compounds is further explained by the hybridization of the *s*, *p*, and *d* orbitals of the metal center.

The bonding behavior of several coordination compounds is best described by the Ligand Field Theory and is similar to Crystal Field Theory. Ligand Field describes the freedom of electrons to move from ligand to metal, and vice versa in a mutual, covalent hybridization or chelation. This theory can also be used to describe the common geometric arrangements of coordination complexes such as octahedral, tetrahedral, and square planar. More specifically, these geometric properties can be used to describe the magnetic and optical properties of coordination compounds from the quantum level. Wyatt et. al.[10] applied this theory in an attempt to explain the observed fragmentation patterns of the mass spectra of various metal β-diketonate complexes.

1.3 Bonding and Reactivity Characteristics of β-Diketonate Compounds

The research presented herein investigates the gas-phase ligand exchange of different metal β-diketonate complexes including the ligands 2,4-pentanedione (acetylacetonate; H(acac)), 1,1,1-trifluoro-5,5-dimethylhexanedione (trifluorotrimethylacetylacetonate; H(tftm)), 3,5-heptanedione (diethylacetylacetonate; H(eeac)), 1,1,1-trifluoro-2,4-pentanedione (trifluoroacetylacetonate; H(tfac)), and 1,1,1,5,5,5-hexafluoro-2,4-pentanedione (hexafluoroacetylacetonate; H(hfac)).

An interesting characteristic of these stable, non-chelated β-diketonate ligands is their tendency to undergo keto-enol tautomerization. In the normal keto form, the carbonyl carbon of both the α and the β carbon are sp^2 hybridized. The enol configuration exhibits a protonated β position as seen on the left side of Figure 1.1. That mechanism of tautomerization occurs when the hydrogen that was bonded to the α carbon moves to the oxygen atom attached to the β carbon. This creates a delocalized charge between both oxygen atoms as seen in Figure 1.1 below. This delocalization causes resonant stability in the chelated form of the molecule.

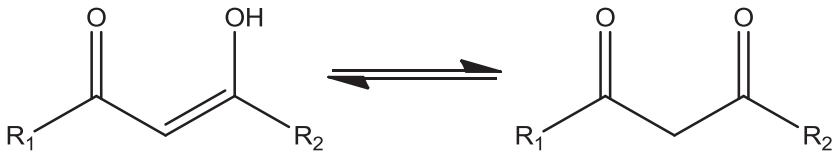

Figure 1.1: Keto-enol tautomerization of a generic β-diketonate ligand

The delocalization of charge in the ligand also defines the bi-dendate characteristic of β-diketonates. When introduced into a basic medium, the acidic hydrogen is stripped from the center carbon, establishing the negative charge of the

ligand. This loss of hydrogen is an essential step to forming a coordination compound because it allows the ligand to bind to each side of the metal, thus fulfilling coordination bonding characteristics and subsequent chelation of the complex. This is not to say, however, that both the keto and the enol stabilized forms are in equilibrium with each other. In fact, the more preferred stable form is highly influenced by the identity of the R groups attached to the ligand. Sloop et. al.[11] have shown that the keto-enol dominant form of a β-diketonate complex is highly dependent on the identity and characteristics of the ligands attached.

To investigate the preference of the keto versus the enol form of trifluoromethyl-β-diketonate molecules, Sloop et. al. used Infrared Spectroscopy (IR), Nuclear Magnetic Resonance (NMR), and Ultraviolet-Visible Spectroscopy (UV-Vis) and determined that the enol form was indeed the preferred form of the β-diketonate. They concluded that this is due to the extended conjugation in the aromatic system, but also proposed that this may be due to the hyperconjugative stabilization in the enol form of the alkyl-substituted trifluoromethyl-β-diketonate. The chelation and stabilization of the ligand as well as the preference of either the keto or enol form is thus heavily influenced by the identity of the R group, whether it is electron-withdrawing or electron-donating. The predominant enol form can be seen below in Figure 1.2

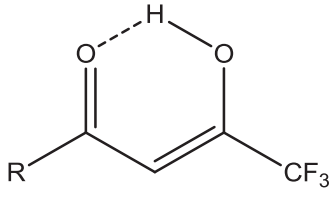

Figure 1.2: The predominant enol form of trifluoro-β-diketonate as described in Sloop et. al.[11]

One of the most appealing characteristics of the β-diketonate compounds, however, is the high level of volatility. Acetylacetonate is generally a highly volatile molecule. The addition of other substituents will influence the volatility of the basic 2,4-pentanedione backbone. For instance, trifluorotrimethylacetylacetonate contains three fluorine atoms (CF_3) per ligand and has a significantly higher overall volatility compared to the unfluorinated ligand. Similarly, a complex with a hexafluoroacetylacetonate containing ligand where two CF_3 groups are present is even more volatile when compared to the trifluorotrimethylacetylacetonate containing species.

1.4 Palladium β-Diketonate Compounds

The study presented herein focuses mainly on palladium β-diketonate complexes and their reactivity in the gas phase by utilizing the collision cell of a triple quadrupole mass spectrometer as a reaction vessel for metal β-diketonate complexes to undergo gas phase ligand exchange reactions. In this study, palladium trifluorotrimethylacetylacetonate ($Pd(tftm)_2$) was successfully synthesized and reacted in the gas phase with other β-diketonate complexes via co-sublimation. This compound has not previously been reported in the literature, therefore further understanding of the importance of the reactivity as well as scientific applications of related compounds such as palladium acetylacetonate ($Pd(acac)_2$), for example, is essential.

One frequently used metal β-diketonate compound is palladium acetylacetonate ($Pd(acac)_2$) seen below in Figure 1.3, and is often complexed with phosphines or other additional organic ligands to enhance and promote catalytic activity.[12]

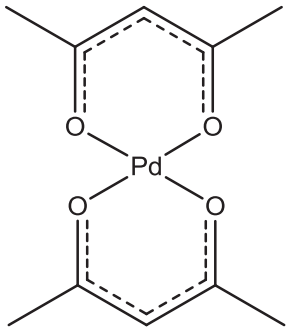

Figure 1.3: $Pd(acac)_2$ complex

For example, Suslov et. al. has coupled $Pd(acac)_2$ with phosphine complexes to improve the catalytic effect of phosphine in the telomerization of 1,3-dienes. One of the most attractive benefits of this approach is that this is a "green" synthetic reaction where there is minimal waste produced in the reaction. Essentially, all components are "recycled" or completely consumed. The product of the β-diketone/phosphine synthesis was also reported to occur at a high yield and the use of the product enhanced the overall performance of the telomerization process, making green chemistry faster, more affordable, and easier to perform.

A group in Finland has used $Pd(acac)_2$ in a very different way. Through the decomposition of $Pd(acac)_2$, they were able to create Pd nano-particles. Nanotechnology is a quickly emerging field in the area of materials chemistry. The applications of nanotechnology are endless and extend to every branch of science. For instance, with the use of these β-diketonate decomposition products, Kukkola et. al.[13] has been able to synthesize a new type of WO_3 nanowire for the detection of hydrogen gas to a level of only 1000 ppm. These wires also exhibit a very low recovery time while maintaining a high sensitivity.

With applications already reported in several areas, $Pd(acac)_2$ is an interesting compound to study. Since $Pd(tftm)_2$ is reported here for the first time, there are plenty of areas of research in which to extend its versatility. Also, with a higher level of volatility, the application possibilities with $Pd(tftm)_2$ are quite promising.

1.5 Synthesis of Metal β-diketonate Complexes

All of the metal β-diketonate complexes (except for any H(hfac) compounds which were purchased commercially from Sigma-Aldrich) used in this study were synthesized using a Lewis acid/Lewis base bench top reaction, adapted from the synthesis of Watson and Lin.[14] A small amount of metal chloride ($PdCl_2$, $CdCl_2$, $NiCl_2$, $CuCl_2$, etc.) was added to approximately 100 mL of de-ionized room temperature water in a 250 mL Erlenmeyer flask on a magnetic stir plate using a plastic coated, nonreactive, magnetic stir bar. Once the metal chloride had dissolved, approximately 0.5 mL of ligand (H(tftm), H(acac), H(tfac), etc.) was also added to the flask. At this point, the water and ligand remained immiscible. Finally, a basic solution of 1:1 (v/v) H_2O:NH_4OH was slowly added to the flask. In most cases, immediate precipitation was observed. To ensure completion of the reaction, however, the reactions were left to stir for approximately 2 hours. Once complete, the precipitates were collected via vacuum filtration and allowed to dry overnight in a dessicator before further analysis by mass spectrometry.

It is also important to note that not all of the metal chlorides were anhydrous. Using a metal chloride hydrate, however, was previously shown in other research to not have an overall effect on reactivity of the compound in either the gas or the solution phase. For instance, Zheng et. al.[16] showed that compounds that were associated with a

hydroxyl group became unassociated with said group upon sublimation in the gas phase. The overall results presented in future chapters tend to agree with the Zheng et. al. findings.

To prepare samples for mass spectrometric analysis, 0.025 M solutions of the metal β-diketonates were prepared using methanol in glass sample vials.

1.6 β-diketonate Molecules and Mass Spectrometry

Though the methods and goals of this study differ from those previously mentioned studies, β-diketonate compounds have long been studied using one of the most common analytical methods in chemistry, Mass Spectrometry (MS). There are many different MS methods that have been used to study β-diketonate compounds. These methods include Electron Impact (EI; used in this study)[16,17,18,19,20], Matrix Assisted Light Desorption Ionization Time-of-Flight (MALDI-TOF)[21], Chemical Ionization (CI)[22], Desorption Ionization Mass Spectrometry (DI)[23], and Liquid Secondary Ion Mass Spectrometry (LSIMS)[24]. A review by Westmore[25] describes a great deal of the previous MS work done regarding β-diketonate complexes where he addresses several important topics including fragmentation patterns and pathways, ionization, and intensity of various β-diketonate compounds.

When synthesized, these metal β-diketonate complexes arrange to form $M(L)_n$, where M is typically a single metal, L is the ligand coordinatively bound, and n = 2 or 3, depending on the oxidation state of the metal. Additionally, homometal or heterometal β-diketonate clusters were observed to form, but were not investigated here.[16] β-diketonate coordination compounds have a delocalization of charge between the two

oxygen atoms on the ligand as well as the possible valence charge or influence of oxidation state from the metal center. With that being said, the generation of a positive molecular ion via electron impact ionization can be summed up in the following equation:

$$ML_n + e^-_{(70eV)} \rightarrow [ML_n]^+ + 2e^- \quad \text{(Eqn 1.1)}$$

The ionization of the metal center of the complex is favored if the metal does not have a full valence shell such as most first row transition metals. The ionization of the ligand is favored in the opposite case and is also influenced by the overall pi-bonding of the system as well as the oxidation state of the metal center.

Another important factor affecting ionization is the identity of the R groups as seen below in Figure 1.4. The presence of fluorine groups on the ligand portion of the compound creates an environment containing many more electron-withdrawing groups. This also increases the charge delocalization across the ligand and makes the compound significantly more ionizable and volatile in the gas phase. In Figure 1.4, the different structures of the metal hexafluoroacetylacetonate (M(hfac)) β-diketonate compounds are presented and illustrate how the structure is influenced by the fluorine subsitituents. For example, the two left species in Figure 1.4 illustrate charge delocalization in the event that the metal center consists of a metal that is not easily oxidized, while the right structure shows how the charge of the metal center can likewise change to accommodate charge delocalization. It is important to note that this behavior varies with the identity of ligand or metal.

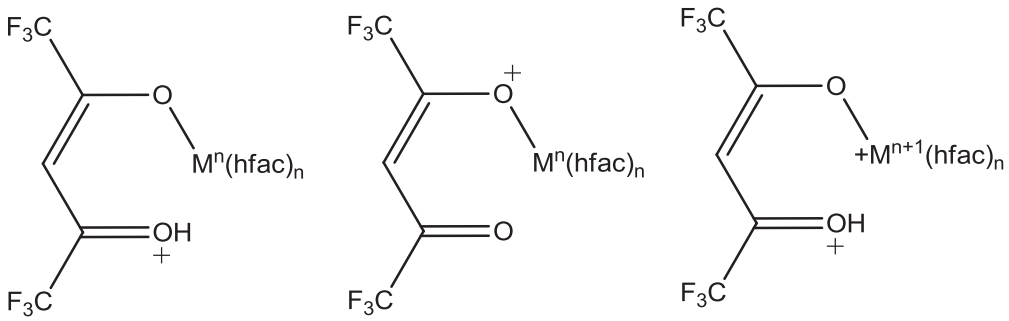

Figure 1.4: The delocalization of charge in the enol form of the $M(hfac)_n$ complex.

1.7 Fragmentation Pathways of β-diketonate Complexes and Ligands

Several previous studies already identified the specific fragmentation patterns associated with common β-diketonate compounds such as hexafluoroacetylacetonate, trifluorotrimethylacetylacetonates, and of course acetylacetonates.[16,17,18,19,20] In this study, the fragmentation patterns of diethylacetylacetonates and trifluoroacetylacetonates were also investigated experimentally. Many metal β-diketonate complexes have been observed to fragment by the loss of an R group. Documenting the fragmentation pattern of the ligands themselves is helpful in order to analyze the fragmentation patterns observed during the gas-phase ligand exchange reactions.

1.7.1 Acetylacetonate (H(acac))

One of the most common loss channels experienced by the acetylacetonate molecule is the loss of a methyl group (*m/z* = 15) resulting in a stable *m/z* = 85 ion. This *m/z* = 85 ion can then further fragment to produce *m/z* = 69, which amounts to the loss of a CH_4 group. A minor loss channel can include the loss of a CO at *m/z* = 72, but this is not an important pathway in this study.

1.7.2 Trifluorotrimethylacetylacetonate ($M(tftm)_2$)

Previous research conducted by Lerach[16] and Hunter[17] has reported how fragmentation patterns are influenced by the chelation of the β-diketonate complex (see Hunter[17] for a full review).

1.8 Gas-Phase Reactions

Gas-phase reactions are not as commonly studied as liquid-phase reactions and materials chemistry. However, there exists an array of chemical reactions that are potentially not possible in common bench-top chemistry, but may be accessible in gas-phase chemistry. Gas-phase reactions offer a different perspective and can shed light on a variety of different topics.

The gas phase reactions of copper and nickel acetylacetonates and trifluorotrimethylacetylacetonates were previously reported in literature[19,20] and were synthesized using the same procedures used in this study. These species were then solvated to 0.025 M in methanol and placed onto a double-looped filament and co-sublimed in the mass spectrometer. The data reported by Hunter et. al. shows the gas-phase ligand exchange between $Cu(acac)_2$ and $Ni(acac)_2$ as well as $Cu(tftm)_2$ and $Ni(tftm)_2$ for the first time. Ligand exchange remains a somewhat unique area of study.

The work presented herein further investigates the gas-phase ligand exhange between metal β-diketonate species with a special emphasis placed on $Pd(tftm)_2$. The reaction mechanisms applicable during the gas-phase ligand exchange involving $Pd(tftm)_2$ with nickel acetylacetonate ($Ni(acac)_2$), nickel diethylacetylacetonate ($Ni(eeac)_2$), nickel hexafluoroacetylacetonate ($Ni(hfac)_2$), and nickel

trifluoroacetylacetonate ($Ni(tfac)_2$) were investigated using the collision cell of the triple quadripole mass spectrometer. The results presented herein from gas-phase ligand exchange reactions are novel, and continue to show great promise for future applications.

Chapter 2: Instrumentation

2.1 Mass Spectrometry

Mass Spectrometry is a versatile and frequently used method of analysis across an array of different fields. Its primary use is to identify the chemical composition of compounds. However, mass spectrometry has evolved over the years to include different types of analysis in the fields of forensics[26], biology[26], environmental health[27], physics[28], biochemistry[29], and pharmaceutical research.[30]

Technological advancements have created several types of mass spectrometers with differences stemming from varying ion sources and mass analyzers. Though this study focuses on electron impact triple quadrupole mass spectrometry, many other techniques have been developed and include electrospray ionization mass spectrometry (ESI-MS), inductively coupled plasma mass spectrometry (ICP-MS), and matrix-assisted light desorption/ionization time-of-flight mass spectrometry (MALDI-TOF-MS) among others. The general components that make up all mass spectrometers is summarized below in Figure 2.1

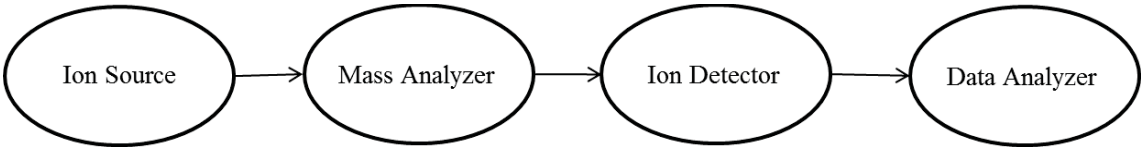

Figure 2.1: The Four Major Parts of a Generic Mass Spectrometer

Mass spectrometers analyze compounds by ionizing the sample to create a charged analyte. The data produced from a mass spectrometer is presented in an *m/z* ratio where *m* is the mass of the analyte and *z* represents the charge of the analyte. For

example, the compound acetylacetonate ($C_5H_8O_2$) has a nominal mass at *m/z* = 100. An acetylacetonate ion with a +1 charge is thus 100/1, or *m/z* = 100. Similarly, and *acac* ion with a +2 charge is 100/2, or *m/z* = 50.

In mass spectrometry, normal integer masses are often used for analysis as opposed to exact masses. The nominal mass is obtained by adding up the number of protons and neutrons of an isotope of an element. The mass for acetylacetone shown above is thus a nominal mass. In this study, considering isotopic values in the nominal mass is essential as palladium has six relatively abundant isotopes that include ^{102}Pd (1.02%), ^{104}Pd (11.14%), ^{105}Pd (22.33%), ^{106}Pd (27.33%), ^{108}Pd (26.46%), and ^{110}Pd (11.72%).[31] The intensity of peaks from species containing Pd thus differs by the natural abundance of each isotope. For example, ^{106}Pd is the most common isotope, while ^{102}Pd is the least abundant. Therefore, ^{106}Pd will show a significantly more intense peak than ^{102}Pd. This also means that for any species containing Pd, a grouping of up to six peaks, one representing each isotope, will be expected. The use of isotopic ratios is quite helpful in correctly assigning a peak as it is analogous to a fingerprint.

2.1.1 Ion Source

The most common difference among all mass spectrometry techniques stems from the ion source, that is, how the ions are initially produced for analysis. This is the most important part of the mass spectrometer because it not only creates the charged ions necessary for spectral analysis, but it also propels these ions to the next section of the mass spectrometer, the mass analyzer. Electron impact (EI) is the ion source used in this study and it can be described as a hard ionization technique meaning that fragmentation

of the species to be analyzed readily occurs. Though this technique is harsh, it is still able to produce the molecular ion. EI works by bombarding a gaseous sample with high energy electrons that are generated from a heated filament that is located within the source. The energy of these electrons is typically 70 eV. This energy is stabilized by the positive charge of the filament and the negative charge of the anode in the system. One advantage of this ionization technique is that the use of such high energy produces fragmentation patterns that are highly reproducible and often aids in mass assignments.

2.1.2 Mass Analyzer

Though the options of mass analyzers is not as extensive as the available ion sources, the mass analyzers within each mass spectrometer can in fact differ in how ions are processed after exiting the source. Mass analyzers function by accelerating the charged species from the ion source and separating them out based upon their *m/z* ratio. Some common mass analyzers include sectors, time-of-flight, and in the case of this study, triple quadrupole mass analyzers.

A single quadrupole mass analyzer is shown below in Figure 2.2 and consists of four parallel, charged rods. A pair of opposing rods has a potential of $+(U+V\cos(\omega t))$ while the other pair has a potential of $-(U+V\cos(\omega t))$. U is the fixed potential, and $V\cos(\omega t)$ is the radio frequency of amplitude V and frequency of ω. These opposite potentials cause the ions introduced from the source to oscillate between the sets of rods. Only ions with a particular *m/z* ratio will successfully pass through onto the next section of the mass spectrometer, the ion detector. Ions consisting of other *m/z* ratios will travel off-axis and will not be detected.

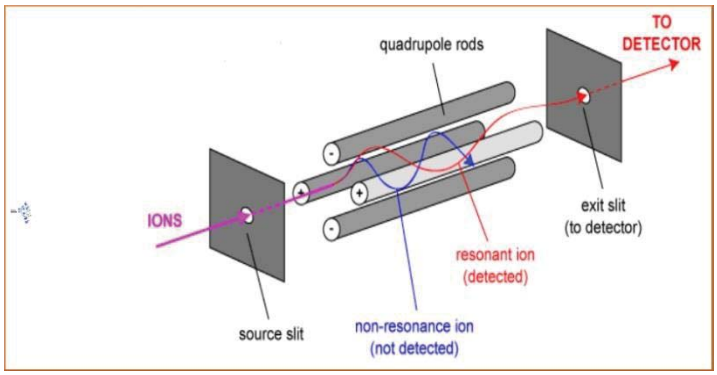

Figure 2.2: Diagram of a Quadrupole Mass Analyzer

(Source: http://www.bris.ac.uk/nerclsmsf/techniques/gcms.html)

As mentioned previously, this study utilizes not a single quadrupole mass analyzer, but a triple quadrupole mass analyzer. In many studies, multiple mass analyzers are utilized in order to select and further induce fragmentation of specific ions. This approach is often referred to as tandem mass spectrometry (MS/MS) where mass analysis occurs at multiple stages. The triple quadrupole mass analyzer used in this study contains two quadrupole mass analyzers with the region between the scanning quadrupoles consisting of a collision cell. The collision cell is unique in the fact that it typically allows for further fragmentation of ions occurring in the gas phase by a process known as collision induced dissociation (CID). A schematic of the triple quadrupole mass spectrometer consisting of one quadrupole, the collision cell, and a third quadrupole can be seen below in Figure 2.3. All ions are created in the source and enter the first quadrupole. An ion with a specific *m/z* ratio survives the scanning of the quadrupoles and enters the collision cell that typically contains an inert gas. In the third quadrupole, the resulting fragments from the collision of the sample with the gas in the collision cell is observed and the entire spectrum is scanned. The information obtained from the CID is regularly used to gain structural information of the analyzed species.

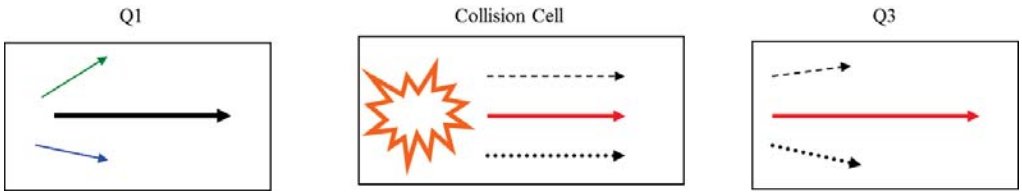

Figure 2.3: Triple Quadrupole Ion Pathway

This research utilized the collision cell of the mass spectrometer in a much more unique way than the intention of the instrument. Instead of introducing an inert gas into the collision cell to simply facilitate further hard dissociation, a neutral metal β-diketonate complex is introduced directly into the chamber. The presence of a reactive species in the collision cell causes the chamber to serve as a reaction vessel instead of a fragmentation aid. For example, $Pd(tftm)_2$ is introduced into the first quadrupole via direct insertion at the source. A mass pertaining to a dominant ion that is present during the co-sublimation experiments is mass selected using the first quadrupole which ensures that only ions of a particular mass are permitted to enter the collision cell. The presence of the other gaseous metal β-diketonate complexes (such as $Ni(acac)_2$) within the collision cell allows select gas-phase reactions to occur during this stage. The third quadrupole scans the entire mass range and provides an analysis of the resulting species. Since a single mass was selected, spectra from these reactions are extremely useful in proposing possible mechanisms describing how reactions among these complexes may occur in the gas phase. These reactions are described later in Chapter 4, and are referred to as "Selective Reactions" since the mass of the dominant ion of interest is selected for gas-phase reactivity.

2.2 Scanning Electron Microscopy

Since $Pd(tftm)_2$ as well as other β-diketonate compounds used in this study are novel and have yet to be reported in literature, scanning electron microscopy paired with electron dispersive spectroscopy was utilized to compliment the mass spectrometric results and to further support the successful synthesis.

Scanning electron microscopy (SEM) is an analytical technique used in the analysis of solid materials. An SEM consists of an electron gun, condenser lens, deflection coils, objective lens, and both a backscattered electron detector and a secondary electron detector. These components allow the microscope to image a sample by scanning it with a focused beam of electrons. A schematic of an SEM can be seen below in Figure 2.4

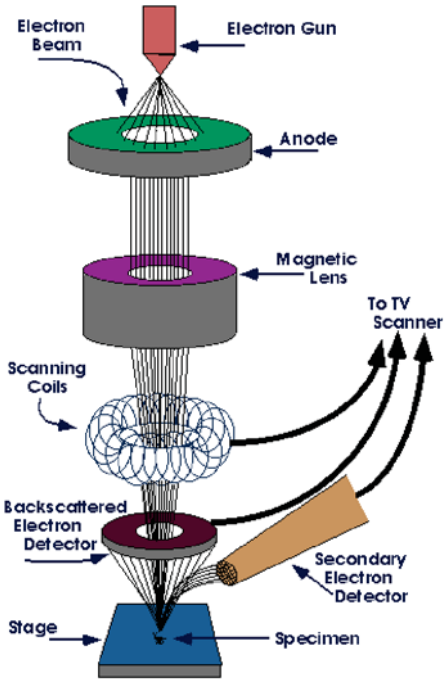

Figure 2.4: Schematic of a Scanning Electron Microscope

(Source: http://www.purdue.edu/ehps/rem/rs/sem.htm)

The electrons from the electron gun interact with the sample at the base of the instrument and release secondary electrons. These secondary electrons are detected by the appropriate detector and are referred to as secondary electron imaging (SEI). This is the primary type of imaging done with the SEM.

Backscattered electrons can also be analyzed and imaged by the SEM. These electrons originate from the electron beam and interact with the nucleus of the atoms in the sample. Backscattered electron imaging (BEI) is helpful and differs from SEI because it can show Z-contrast in a sample. Z-contrast simply means that compounds or elements with a higher atomic number appear brighter than those with a lower atomic number, thus making it easier to identify which part of the material contains the heavier elements.

2.3 Electron Dispersive X-Ray Spectroscopy

Energy Dispersive X-Ray Spectroscopy (EDS) is also an analytical technique that is often paired with SEM imaging because it can identify the chemical composition of the different elements imaged. The same sample that was analyzed in the SEM undergoes X-Ray excitation to produce another unique spectrum. Since each element has a unique atomic structure, each element has a unique signal measured in KeV energy. The incident beam to the sample excites an electron in the inner shell and ejects that electron, producing an electron hole. An electron from a higher energy level then fills that electron hole by emitting a characteristic X-Ray for that element. EDS is ideal for heavier elements since the energy is measured on the KeV scale, while EELS (Electron Energy Loss Spectroscopy) is sufficient for lighter element detection as its energy is measured on the eV scale.

Chapter 3: Experimental

3.1 Introduction

All of the metal acetylacetonate ($M(acac)_2$), metal trifluorotrimethylacetylacetonate ($M(tftm)_2$), metal trifluoroacetylacetonate ($M(tfac)_2$), metal diethylacetylacetonate ($M(eeac)_2$), and metal 3-methyl-2,4-pentanedione ($M(3mac)_2$) compounds were synthesized in the lab. They were not further purified before mass spectrometric analysis. The metal hexfluoroacetylacetonate ($M(hfac)_2$) compounds were purchased commercially from PCR, Inc. (Gainesville, FL, USA). All of the ligands used in each of the synthesis were purchased from Sigma-Aldrich (St. Louis, MO, USA) and were also used in the synthesis without further purification. For mass spectrometric analysis, all samples were prepared in methanol at a concentration of 0.0250 M, which was shown to be an effective concentration for mass spectral analysis by Hunter.[17]

3.2 Metal 2,4-pentanedione ($M(acac)_2$) Synthesis

3.2.1 $Ni(acac)_2$ Synthesis

The addition of 0.5045 g of metal chloride ($NiCl_2 \cdot xH_2O$) and 0.800 mL of acetylacetone to 100 mL of deionized water caused the solution to turn light green in color. Upon the addition of 20 mL of 1:1 (*v/v*) NH_4OH:H_2O, the solution turned light blue with a periwinkle blue color precipitate. The mixture was stirred for two hours with gentle heating. The precipitate was isolated using vacuum filtration, dried overnight in a dessicator, and prepared for mass spectrometric analysis by dissolving in methanol to a concentration of 0.0250 M. The synthesis was confirmed by the mass spectrum

presented in Section 4.2.3 in Figure 4.2 (a). The percent yield for this reaction was 74.3%.

3.2.2 $Fe(acac)_2$ Synthesis

The addition of 0.5821 g of metal chloride ($FeCl_2 \cdot 4H_2O$) and 0.601 mL of acetylacetone to 100 mL of deionized water caused the solution to turn light green in color. Upon the addition of 20 mL of 1:1 (*v/v*) NH_4OH:H_2O, the solution turned a rusty red color. The mixture was stirred for two hours with gentle heating. The precipitate was isolated using vacuum filtration, dried overnight in a dessicator, and prepared for mass spectrometric analysis by dissolving in methanol to a concentration of 0.0250 M. The success of this synthesis was not confirmed by mass spectrometric analysis.

3.3 Metal 1,1,1-trifluoro-5,5-dimethyl-2,4-hexanedione ($M(tftm)_2$) Synthesis

3.3.1 $Pd(tftm)_2$ Synthesis

The addition of 0.3565 g of metal chloride ($PdCl_2$) and 0.696 mL of 1,1,1-trifluoro-5,5-dimethylhexanedione to 100 mL of deionized water caused the solution to remain clear. Upon the addition of 20 mL of 1:1 (*v/v*) NH_4OH:H_2O, the solution remained clear, but an opaque precipitate formed. The mixture was stirred for two hours with gentle heating. The precipitate was isolated using vacuum filtration, dried overnight in a dessicator, and prepared for mass spectrometric analysis by dissolving in methanol to a concentration of 0.0250 M. The synthesis was confirmed by the mass spectrum presented in Figure 4.1. The percent yield for this reaction was 97.0%.

3.3.2 $Cd(tftm)_2$ Synthesis

The addition of 0.2825 g of metal chloride ($CdCl_2$) and 0.658 mL of 1,1,1-trifluoro-5,5-dimethylhexanedione to 100 mL of deionized water caused the solution to remain clear. Upon the addition of 20 mL of 1:1 (*v/v*) NH_4OH:H_2O, the solution remained clear, but emitted a puff of white smoke. After about 10 more minutes of stirring, a cloudy white precipitate formed. The mixture was stirred for two hours with gentle heating. The precipitate was isolated using vacuum filtration, dried overnight in a dessicator, and prepared for mass spectrometric analysis by dissolving in methanol to a concentration of 0.0250 M. The synthesis was confirmed by the mass spectrum presented in Figure 6.6. The percent yield of this synthesis reaction was 15.6%.

3.3.3 $Co(tftm)_2$ Synthesis

The addition of 0.3953 g of metal chloride ($CoCl_2 \cdot 6H_2O$) and 0.578 mL of 1,1,1-trifluoro-5,5-dimethylhexanedione to 100 mL of deionized water caused the solution to become deep blue in color. Upon the addition of 20 mL of 1:1 (*v/v*) NH_4OH:H_2O, the solution turned brown with a khaki colored precipitate. The mixture was stirred for two hours with gentle heating. The precipitate was isolated using vacuum filtration, dried overnight in a dessicator, and prepared for mass spectrometric analysis by dissolving in methanol to a concentration of 0.0250 M. The synthesis was confirmed by the mass spectrum presented in Figure 6.3. The percent yield of this synthesis reaction was 55.6%.

3.3.4 $Cu(tftm)_2$ Synthesis

The addition of 0.2212 g of metal chloride ($CuCl_2$) and 0.572 mL of 1,1,1-trifluoro-5,5-dimethylhexanedione to 100 mL of deionized water caused the solution to become a pale bluish-green color. Upon the addition of 20 mL of 1:1 (*v/v*) NH_4OH:H_2O, the solution turned to a dark royal blue color. The mixture was stirred for two hours with gentle heating. The precipitate was isolated using vacuum filtration, dried overnight in a dessicator, and prepared for mass spectrometric analysis by dissolving in methanol to a concentration of 0.0250 M. The synthesis was confirmed by the mass spectrum presented in Figure 6.5. The percent yield for this synthesis reaction was 43.1%.

3.3.5 $Ca(tftm)_2$ Synthesis

The addition of 0.1925 g of metal chloride ($CaCl_2$) and 0.603 mL of 1,1,1-trifluoro-5,5-dimethylhexanedione to 100 mL of deionized water caused the solution to remain clear. Upon the addition of 20 mL of 1:1 (*v/v*) NH_4OH:H_2O, the solution emitted a white smoke followed by an immediate formation of a white precipitate. The mixture was stirred for two hours with gentle heating. The precipitate was isolated using vacuum filtration, dried overnight in a dessicator, and prepared for mass spectrometric analysis by dissolving in methanol to a concentration of 0.0250 M. The success of this synthesis was not confirmed by mass spectrometric analysis.

3.3.6 $Fe(tftm)_2$ Synthesis

The addition of 0.3484 g of metal chloride ($FeCl_2$) and 0.582 mL of 1,1,1-trifluoro-5,5-dimethylhexanedione to 100 mL of deionized water caused the solution to turn a light orange color. Upon the addition of 20 mL of 1:1 (*v/v*) NH_4OH:H_2O, the

solution emitted a white smoke and turned to a cloudy dark orange color. The mixture was stirred for two hours with gentle heating. The precipitate was isolated using vacuum filtration, dried overnight in a dessicator, and prepared for mass spectrometric analysis by dissolving in methanol to a concentration of 0.0250M. The success of this synthesis was not confirmed by mass spectrometric analysis.

3.3.7 $Fe(tftm)_3$ Synthesis

The addition of 0.3161 g of metal chloride ($FeCl_3 \cdot 6H_2O$) and 0.607 mL of 1,1,1-trifluoro-5,5-dimethylhexanedione to 100 mL of toluene caused the solution to become a light red color. Upon the addition of 20 mL of 1:1 (*v/v*) NH_4OH:H_2O, the solution formed an aqueous layer and an organic layer, with a dark red precipitate formation in the aqueous layer. The mixture was stirred for two hours with gentle heating. The precipitate was isolated using a Rotovap, dried overnight in a dessicator, and prepared for mass spectrometric analysis by dissolving in methanol to a concentration of 0.0250 M. The success of this synthesis was not confirmed by mass spectrometric analysis.

3.3.8 $Al(tftm)_3$ Synthesis

The addition of 0.2956 g of metal chloride ($AlCl_3 \cdot 6H_2O$) and 0.591 mL of 1,1,1-trifluoro-5,5-dimethylhexanedione to 100 mL of toluene caused the solution to remain clear. Upon the addition of 20 mL of 1:1 (*v/v*) NH_4OH:H_2O, the solution remained clear, but formed an aqueous and an organic layer, with a white precipitate formation in the aqueous layer. The mixture was stirred for two hours with gentle heating. The precipitate was isolated using a Rotovap, dried overnight in a dessicator, and prepared for

mass spectrometric analysis by dissolving in methanol to a concentration of 0.0250 M. The success of this synthesis was not confirmed by mass spectrometric analysis.

3.3.9 $Mg(tftm)_2$ Synthesis

The addition of 0.3660 g of metal chloride ($MgCl_2 \cdot 6H_2O$) and 0.626 mL of 1,1,1-trifluoro-5,5-dimethylhexanedione to 100 mL of deionized water caused the solution to remain clear. Upon the addition of 20 mL of 1:1 (*v/v*) NH_4OH:H_2O, the solution emitted a white smoke followed by an immediate formation of a white precipitate. The mixture was stirred for two hours with gentle heating. The precipitate was isolated using vacuum filtration, dried overnight in a dessicator, and prepared for mass spectrometric analysis by dissolving in methanol to a concentration of 0.0250 M. The synthesis was confirmed by the mass spectrum presented in Figure 6.1. The percent yield for this synthesis reaction was 92.4%.

3.4 Metal 1,1,1-trifluoro-2,4-pentanedione ($M(tfac)_2$) Synthesis

3.4.1 $Ni(tfac)_2$ Synthesis

The addition of 0.2621 g of metal chloride ($NiCl_2 \cdot 6H_2O$) and 0.496 mL of 1,1,1-trifluoro-2,4-pentanedione to 100 mL of deionized water caused the solution to turn light green in color. Upon the addition of 20 mL of 1:1 (*v/v*) NH_4OH:H_2O, the solution stayed green, however, a fine white precipitate formed. The mixture was stirred for two hours with gentle heating. The precipitate was isolated using vacuum filtration, dried overnight in a dessicator, and prepared for mass spectrometric analysis by dissolving in methanol to a concentration of 0.0250 M. The synthesis was confirmed by the mass spectrum presented in Figure 4.25 (a). The percent yield for this synthesis reaction was 88.5%.

3.5 Metal 3,5-heptanedione ($M(eeac)_2$) Synthesis

3.5.1 $Ni(eeac)_2$ Synthesis

The addition of 0.5660 g of metal chloride ($NiCl_2 \cdot 6H_2O$) and 0.645 mL of 3,5-heptanedione to 100 mL of deionized water caused the solution to turn light green in color. Upon the addition of 20 mL of 1:1 (*v/v*) NH_4OH:H_2O, the solution turned dark blue with a sky blue precipitate. The mixture was stirred for two hours with gentle heating. The precipitate was isolated using vacuum filtration, dried overnight in a dessicator, and prepared for mass spectrometric analysis by dissolving in methanol to a concentration of 0.0250 M. The synthesis was confirmed by the mass spectrum presented in Figure 4.6. The percent yield of this synthesis reaction was 67.3%.

3.5.2 $Cu(eeac)_2$ Synthesis

The addition of 0.3126 g of metal chloride ($CuCl_2$) and 0.635 mL of 3,5-heptanedione to 100 mL of deionized water caused the solution to turn dark blue. Upon the addition of 20 mL of 1:1 (*v/v*) NH_4OH:H_2O, the solution stayed the same color but formed a light blue precipitate. The mixture was stirred for two hours with gentle heating. The precipitate was isolated using vacuum filtration, dried overnight in a dessicator, and prepared for mass spectrometric analysis by dissolving in methanol to a concentration of 0.0250 M. The synthesis was confirmed by the mass spectrum presented in Figure 6.4. The percent yield of this synthesis reaction was 67.3%.

3.5.3 $Mg(eeac)_2$ Synthesis

The addition of 0.5457 g of metal chloride ($MgCl_2 \cdot 6H_2O$) and 0.724 mL of 3,5-heptanedione to 100 mL of deionized water caused the solution to remain clear. Upon the addition of 20 mL of 1:1 (*v/v*) NH_4OH:H_2O, the solution remained clear for about 10 minutes. After 10 minutes of stirring, the solution produced a cloudy white precipitate. The mixture continued to stir for two hours with gentle heating. The precipitate was isolated using vacuum filtration, dried overnight in a dessicator, and prepared for mass spectrometric analysis by dissolving in methanol to a concentration of 0.0250 M. The synthesis was confirmed by the mass spectrum presented in Figure 6.2. The percent yield of this synthesis was 32.1%.

3.5.4 $Co(eeac)_2$ Synthesis

The addition of 0.5636 g of metal chloride ($CoCl_2 \cdot 6H_2O$) and 0.645 mL of 3,5-heptanedione to 100 mL of deionized water caused the solution to turn a deep blue color. Upon the addition of 20 mL of 1:1 (*v/v*) NH_4OH:H_2O, the solution turned almost black with a peach colored precipitate. The mixture was stirred for two hours with gentile heating. The precipitate was isolated using vacuum filtration, dried overnight in a dessicator, and prepared for mass spectrometric analysis by dissolving in methanol to a concentration of 0.0250 M. The synthesis was confirmed by the mass spectrum presented in Figure 6.4. The percent yield of this synthesis was 28.0%.

3.5.5 $Al(eeac)_3$ Synthesis

The addition of 0.4408 g of metal chloride ($AlCl_3 \cdot 6H_2O$) and 0.741 mL of 3,5-heptanedione to 100 mL of toluene caused the solution to remain clear. Upon the

addition of 20 mL of 1:1 (*v/v*) $NH_4OH:H_2O$, the solution formed an aqueous layer and an organic layer, with a white precipitate formed in the aqueous layer. The mixture was stirred for two hours with gentile heating. The precipitate was isolated using a Rotovap, dried overnight in a dessicator, and prepared for mass spectrometric analysis by dissolving in methanol to a concentration of 0.0250 M. The success of this synthesis was not confirmed by mass spectrometric analysis.

3.5.6 $Fe(eeac)_2$ Synthesis

The addition of 0.3039 g of metal chloride ($FeCl_2$) and 0.651 mL of 3,5-heptanedione to 100 mL of water caused the solution to turn a rusty color. Upon the addition of 20 mL of 1:1 (*v/v*) $NH_4OH:H_2O$, the solution formed an aqueous layer and an organic layer, with a white precipitate formed in the aqueous layer. The mixture was stirred for two hours with gentile heating. The precipitate was isolated using a Rotovap, dried overnight in a dessicator, and prepared for mass spectrometric analysis by dissolving in methanol to a concentration of 0.0250 M. The success of this synthesis was not confirmed by mass spectrometric analysis.

3.6 Metal 3-methyl-2,4-pentanedione ($M(3mac)_2$) Synthesis

3.6.1 $Ni(3mac)_2$ Synthesis

The addition of 0.6227 g of metal chloride ($NiCl_2 \cdot 6H_2O$) and 0.608 mL of 3-methyl-2,4-pentanedione to 100 mL of deionized water caused the solution to turn a pale green color. Upon the addition of 20 mL of 1:1 (*v/v*) $NH_4OH:H_2O$, the solution turned to a cerulean color. The mixture stirred for two hours with gentle heating. The precipitate was isolated using vacuum filtration, dried overnight in a dessicator, and prepared for

mass spectrometric analysis by dissolving in methanol to a concentration of 0.0250 M. The success of this synthesis was not confirmed by mass spectrometric analysis.

3.6.2 $Co(3mac)_2$ Synthesis

The addition of 0.6212 g of metal chloride ($CoCl_2 \cdot 6H_2O$) and 0.608 mL of 3-methyl-2,4-pentanedione to 100 mL of deionized water caused the solution to turn a faint pink color. Upon the addition of 20 mL of 1:1 (*v/v*) NH_4OH:H_2O, the solution turned a brownish black color with a peach colored precipitate. The mixture was stirred for two hours with gentle heating. The precipitate was isolated using vacuum filtration, dried overnight in a dessicator, and prepared for mass spectrometric analysis by dissolving in methanol to a concentration of 0.0250 M. The success of this synthesis was not confirmed by the mass spectrometric analysis.

3.6.3 $Al(3mac)_3$ Synthesis

The addition of 0.4898 g of metal chloride ($AlCl_3 \cdot 6H_2O$) and 0.709 mL of 3-methyl-2,4-pentanedione to 100 mL of toluene caused the solution to remain clear. Upon the addition of 20 mL of 1:1 (*v/v*) NH_4OH:H_2O, the solution separated into an aqueous layer and an organic layer with the formation of a white precipitate in the aqueous layer. The mixture was stirred for two hours with gentle heating. The precipitate was isolated using a Rotovap, dried overnight in a dessicator, and prepared for mass spectrometric analysis by dissolving in methanol to a concentration of 0.0250 M. The success of this synthesis was not confirmed by mass spectrometric analysis.

3.7 Mass Spectrometric Parameters

All mass spectrometric data of individual metal β-diketonate complexes, as well as the co-sublimations, were obtained using a Finnigan TSQ 7000 triple quadrupole electron impact mass spectrometer. Each sample was introduced into the mass spectrometer via direct insertion using a probe with a Re filament. Each spectrum was generated using an electron energy of 70 eV with a *m/z* range of 50 – 650. The system was calibrated regularly using a perfluorotributylamine (PFTBA) calibration gas. The pressure of the source was maintained at 10^{-6} Torr with a source temperature and manifold temperature held at 160 ^{o}C and 80 ^{o}C, respectively. The probe temperature was set to ramp from ambient temperature to about 1000 ^{o}C over a 10 minute period, though most samples completely sublimed within the first 5 minutes. The recorded isotopic intensities observed from these spectra match the natural abundances expected for the individual atoms.

Approximately 1.0 – 1.5 μL aliquots of the 0.0250 M solutions were added to a custom-made, double-looped filament. The loops were evaporated to dryness within the vacuum chamber of the mass spectrometer. For single spectrum analysis, a single sample was added to either the double-looped filament or just a single-looped filament and analyzed with the first quadrupole of the mass spectrometer. For all co-sublimation reactions, one metal β-diketonate complex was added to one loop while the other was added to the adjacent loop. The 2 mm separation between the loops ensured no physical contact allowing for only gas-phase interaction.

Specific gas-phase reactions were analyzed within the CID (Collision Induced Dissociation) chamber. This step of the research was necessary in order to shed light on which specific ions were involved during the gas-phase ligand exchange. During these experiments, 1.0 μL of one sample was placed on the filament and ionized while the neutral species was evaporated directly into the collision cell. Collision cell pressures were held at 10^{-3} Torr while the source pressure was maintained at 10^{-6} Torr. During collision cell experiments, the ionization energy was lowered based upon the fragmentation behavior of the individual fragment selected. Mass-selected fragments ranged from intact metal β-diketonate species to small fragments of the original species. Species of interest were mass-selected in the first quadrupole and then reacted in the collision cell with the third quadrupole scanning for reaction exchange products. This unique application of the collision cell provides an opportunity to examine the role of possible reaction mechanisms that would otherwise be non-accessible given the presence of various ions during the initial ionization step.

3.8 Scanning Electron Microscope (SEM) / Energy Dispersive X-Ray Spectrometry (EDS) Parameters

All SEM images were obtained using a JEOL Focused Ion Beam Scanning Electron Microscope (JEOL JIB-4500 MultiBeam FIB-SEM), equipped with micromanipulator, gas injection systems and a silicon drift energy dispersive X-ray spectrometer detector (EDS). It provided high resolution 3-D imaging and analysis for the structure of $Pd(tftm)_2$. $Pd(tftm)_2$ powder was prepared as previously mentioned in Section 3.3.1 and was adhered to a clean steel SEM sample plate using carbon tape. The images were taken in secondary electron imaging mode (SEI) at 15 kV at 500x, 2,000x,

and 3,000x magnification. Another image was collected in the backscatter electron imaging mode (BEI) at 15 kV and 3,000x magnification. These images can be found in Appendix B.

Energy Dispersive Spectrometer (EDS) micro-analysis was also performed by measuring the energy and intensity distribution of X-ray signals generated by a focused electron beam on the specimen. With the attachment of the energy dispersive spectrometer, the elemental composition of $Pd(tftm)_2$ was verified. This data can also be found in Appendix B.

Chapter 4

The Co-Sublimation and Gas-Phase Ligand Exchange Reactions of Palladium Trifluorotrimethylacetylacetonate ($Pd(tftm)_2$) with Nickel Acetylacetonate ($Ni(acac)_2$), Nickel Diethylacetylacetonate ($Ni(eeac)_2$), Nickel Hexafluoroacetylacetonate ($Ni(hfac)_2$), and Nickel Trifluoroacetylacetonate ($Ni(tfac)_2$).

4.1 Introduction

The data presented in this Chapter shows the most evidence of gas-phase ligand exchange reactions to date and it examines the co-sublimation of $Pd(tftm)_2$ with $Ni(acac)_2$, $Ni(eeac)_2$, $Ni(hfac)_2$, and $Ni(tfac)_2$. The co-sublimation spectra presented in this Chapter focuses on palladium as the metal center and shows similar results to those previously reported using different metal centers.[16,17,18,19,20] Even with a heavy metal center, these palladium containing β-diketonate complexes were observed to behave similarly in the gas phase compared to complexes containing the lighter metal complexes previously studied. Palladium is much more isotopically rich than these lighter metals which makes the spectra produced from the co-sublimation reactions more difficult to interpret. The results presented herein indicate partial, mixed ligand, and even some complete ligand exchange.

While the presence of the mixed ligand species in the mass spectrum is clear evidence that a gas-phase reaction occurred, more evidence is necessary to propose how these reactions occur mechanistically. To obtain this data, selective reactions involving mass-selected ions and neutral species were explored using the collision cell. As

mentioned in Chapter 3, Section 3.7, the collision cell of the triple quadrupole mass spectrometer is employed differently than how it is conventionally used. For these reactions to occur, neutral $Ni(acac)_2$ (or other nickel compounds) is introduced into the collision cell by evaporation. These compounds easily vaporize due to their high volatility and the reduced pressure of the instrument. Once the residual air is removed from the collision chamber, gaseous nickel β-diketonate compounds are introduced and maintained at a pressure of 10^{-6} Torr. Mass-selected $Pd(tftm)_2$ cations then enter the collision cell consisting of known neutral species and are allowed to react. For example, if m/z = 498 is selected, which corresponds to $[Pd(tftm)_2]^+$, only species with m/z = 498 can enter the collision cell where it may or may not react with the gaseous nickel β-diketonate compound. The third quadrupole then detects all species that may have been produced.

The resulting masses and intensities following the selective reaction experiments may indicate that only partial ligand exchange, the formation of the mixed ligand, complete ligand exchange, and in some cases, no reaction has occured. By selecting only a single mass in the first quadrupole and comparing the resulting intensities of mixed ligand masses in the third quadrupole, gas-phase reaction mechanisms can be proposed like those presented in Equations 4.1 – 4.32. It is important to keep in mind in the following three Chapters that, while the co-sublimation reactions offer convincing evidence that gas-phase ligand exchange reactions can and do occur, it is the selective reactions performed in the collision cell (where only a single mass from the first quadrupole is selected) that offers further evidence for mechanism propositions.

4.2 Results and Discussion

4.2.1 Palladium trifluorotrimethylacetylacetonate ($Pd(tftm)_2$)

As stated previously, many of the metal β-diketonate compounds featured in this study are novel compounds. The main focus in both Chapters 4 & 5 revolves more specifically around $Pd(tftm)_2$. This complex was synthesized according to the guidelines expressed in Chapter 3, Section 3.3.1. For structural confirmation, $Pd(tftm)_2$ was examined individually via triple quadrupole mass spectrometry prior to the co-sublimation gas-phase exchange reactions outlined in Chapters 4 & 5. Figure 4.1 below represents a typical cationic mass spectrum of $Pd(tftm)_2$ with the corresponding relative abundances featured in Table 4.1. Identifying the fragmentation patterns observed in the single species mass spectrum is essential in order to appreciate the results from the co-sublimation and selected reactions featured later in this Chapter. The fragments listed in Table 4.1 were mass-selected and subsequently used in the selective reactions within the collision cell of the mass spectrometer. The results from these reactions can be found in Figures 4.2 – 4.4.

Figure 4.1 is a representative positive mass spectrum of $Pd(tftm)_2$ and is presented for the first time with a mass range of m/z = 100 - 500. This spectrum is also presented in all of the following stacked co-sublimation figures, for example, see Figure 4.2 (b), with a mass range of m/z = 50 – 650 for comparative purposes. Figure 4.1 is presented with a shortened mass range in order to better illustrate the isotopic characteristics of this complex and to minimize the abundance of the m/z = 57 ion signal that overwhelms the data given its high intensity. The loss of a *t*Bu group (m/z = 57) is a common loss channel

for these complexes and can minimize the importance of the other species that are present, but at a lower ion intensity. In Figure 4.1, *m/z* = 300, corresponding to $[Pd(tftm)]^+$, was selected as the most abundant peak, and thereafter was used as the reference peak when calculating the relative abundances of the fragmentation pattern observed for $Pd(tftm)_2$. This representation of the spectra also allows for a better view of the signature six-peak isotopic pattern exhibited by all palladium-containing compounds.

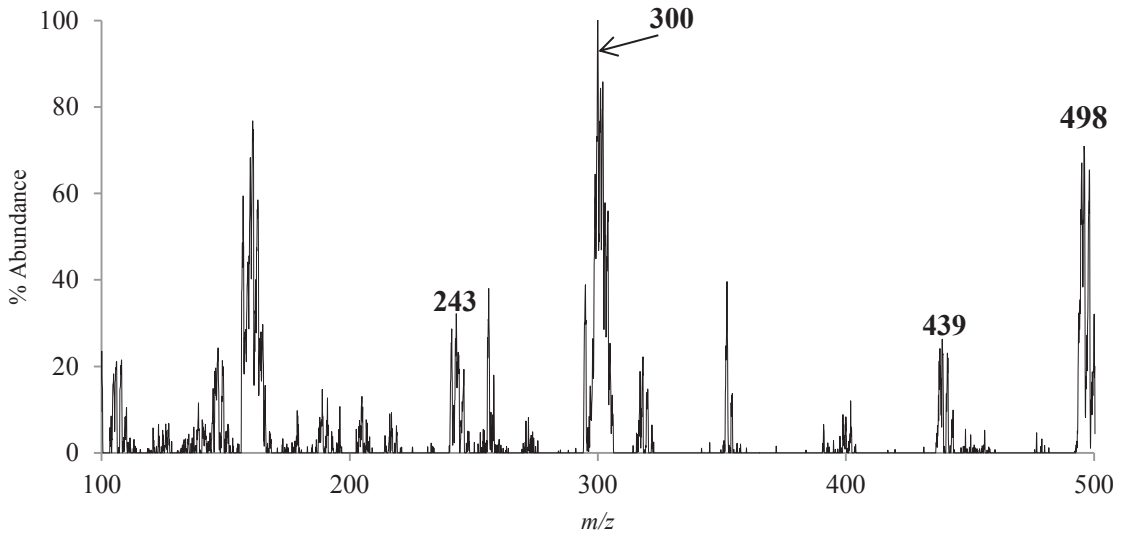

Figure 4.1: The 70 eV positive EI mass spectrum of $Pd(tftm)_2$, showing only the range between *m/z* = 100 and *m/z* = 500 to exhibit more isotopic abundance without the interference of the background *m/z* = 57 peak corresponding to the loss of a *t*Bu group.

Species	*m/z*	Relative Abundance
$[Pd(tftm)_2]^+$	496	65
$[Pd(tftm)(tftm - tBu)]^+$	439	21
$[Pd(tftm)(tftm - CF_3)]^+$	429	<1
$[Pd(tftm)]^+$	300	100
$[Pd(tftm - tBu)]^+$	243	31
$[Pd(tftm - CF_3)]^+$	231	<1

Table 4.1: The fragmentation species and corresponding relative abundances of the mass spectral analysis of $Pd(tftm)_2$ as presented in Figure 4.1.

4.2.2 Nickel Acetylacetonate ($Ni(acac)_2$)

For more details regarding nickel acetylacetonate ($Ni(acac)_2$) and its corresponding fragmentation behavior, please refer to Hunter et.al.[17] A representative cationic mass spectrum of $Ni(acac)_2$ is featured in Section 4.2.3 in Figure 4.2 (a).

4.2.3 The Co-Sublimation of $Pd(tftm)_2$ & $Ni(acac)_2$

The mass spectra presented in Figure 4.2 are vertically stacked in order to better visualize the extent of gas-phase ligand exchange. The top portion, Figure 4.2 (a), features the positive EI mass spectrum of $Ni(acac)_2$ and shows typical fragmentation patterns such as the parent peak at *m/z* = 256 and the loss of a methyl group at *m/z* = 241. The middle portion, Figure 4.2 (b) shows the spectrum of $Pd(tftm)_2$, which resembles Figure 4.1 but over a different mass range. The bottom portion, Figure 4.2 (c) corresponds to the mass spectrum from the co-sublimation of both $Pd(tftm)_2$ and $Ni(acac)_2$ using a two-loop filament.

As indicated in Chapter 3, Section 3.7, a two-looped filament is used to ensure that only a gas-phase reaction can occur. It is important to note that there are peaks present in the co-sublimation spectrum that are not featured in the previous single species spectra which is a clear indication of gas-phase ligand exchange. Those species that underwent any amount of gas-phase ligand exchange, which includes both partial and complete exchange, are labeled within the spectra and are highlighted in bold. The *m/z* values and relative abundances for the fragmentation of the single species, the co-sublimation species, as well as the exchange products are featured below in Table 4.2. The relative abundances were calculated in relation to the most intense peak of

importance, that is, the peak with the most intensity that is either a partial exchange, mixed ligand, or full exchange product. For example, in Figure 4.2 (c), the most intense peak is *m/z* = 57. However, *m/z* = 391 was selected as the base peak for the relative abundance calculations since it was the next highest intense peak and corresponds to $[Ni(tftm)(tftm - tBu)]^+$, which is a ligand exchange product. Results from this co-sublimation experiment show partial, mixed, and full ligand exchange for both the nickel and the palladium species, however the nickel appears to have a greater success in performing the complete exchange of ligands.

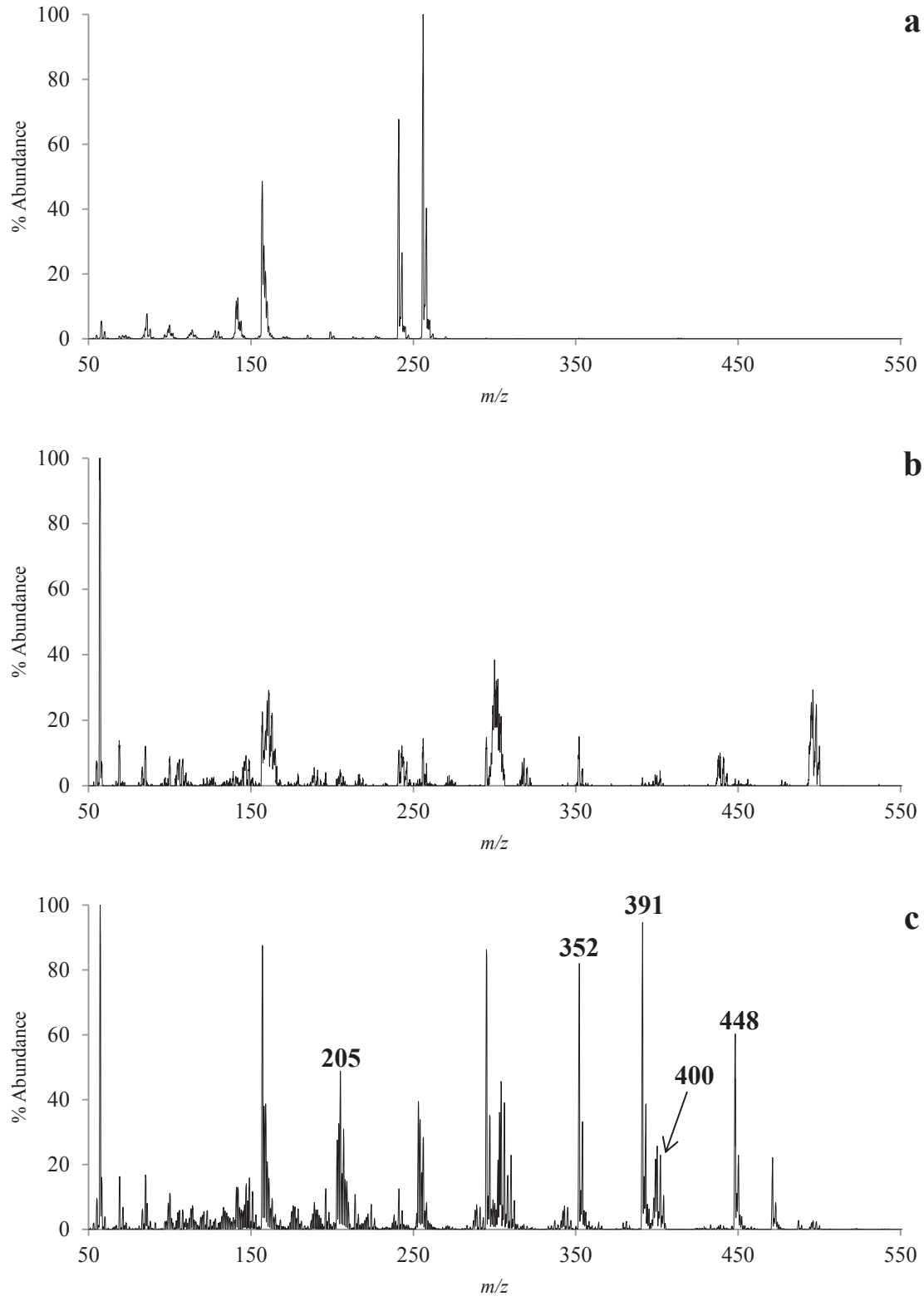

Figure 4.2: The 70 eV positive EI mass spectra of (a) $Ni(acac)_2$, (b) $Pd(tftm)_2$, and (c) the co-sublimation spectrum of $Pd(tftm)_2$ and $Ni(acac)_2$. Mixed ligand and ligand exchange peaks are highlighted in bold.

	Mass	Mass	NiL_2	PdL'_2	NiL_2 & PdL'_2	NiL_2 & PdL'_2
Species	Ni	Pd	Ni	Pd	Ni	Pd
ML_2	256	304	100		32	51
ML_2-CH_3	241	289	66		13	8
ML_2-$2CH_3$	226	275	1		3	0
ML	157	205	57		100	52
ML'_2	448	496		65	68	3
ML'_2-*t*Bu	391	439		20	100	1
ML'_2-CF_3	379	429		<1	2	<1
ML'	253	300		100	42	10
ML'-*t*Bu	196	243		31	13	6
ML'-CF_3	184	231		<1	<1	<1
MLL'	352	400			92	28
ML(L'- tBu)	295	343			98	7
ML(L' - CF_3)	283	331			1	<1
M(L-CH_3)L'	337	385			3	<1

L = (acac); L' = (tftm)

Table 4.2: The mass spectrometric relative abundances of nickel and palladium β-diketonate complexes as well as the co-sublimation experiment as presented in Figure 4.2.

4.2.4 Selective Reaction of $Pd(tftm)_2$ & $Ni(acac)_2$

As stated in Chapter 3, Section 3.7, the selective reactions performed in this study utilize the collision cell of the triple quadrupole mass spectrometer in an unconventional way. The first quadrupole mass selects specific cations, and in this study include the intact $[Pd(tftm)_2]^+$ species as well as the following framents: $[Pd(tftm)(tftm–tBu)]^+$, $[Pd(tftm)(tftm\text{-}CF_3)]^+$, $[Pd(tftm)]^+$, $[Pd(tftm - tBu)]^+$, and $[Pd(tftm - CF_3)]^+$. Only those species can enter the collision cell where a selective reaction may or may not ensue. The third quadrupole scans the entire mass ramp for all products of the selective reactions. The spectra displayed in Figures 4.3, 4.4, and 4.5 show the results of these specific reactions. All selective reactions were run under conditions similar to the co-sublimation

reactions at a temperature ramp of ambient temperature to 1000°C over a span of ten minutes with pressures constant at 10^{-6} Torr, and ionization energy of 400 μA, and the electron multiplier held at 950 V. The collision chamber was purged with the gaseous $Ni(acac)_2$ prior to each run. Equation 4.1 below shows the proposed mechanism from the results of the first selective reaction.

$$[Pd(tftm)(tftm)]^+ + Ni(acac)_2 \rightarrow [Pd(tftm)(acac)]^+ + Ni(tftm)(acac) \qquad \text{(Eqn 4.1)}$$

Figure 4.3 is a mass spectrum that illustrates the results of the reaction after selecting *m/z* = 498 ($[Pd(tftm)_2]^+$). By selecting this peak and allowing it to react with the gaseous $Ni(acac)_2$, a product of *m/z* = 400 is observed. A *m/z* = 400 ion corresponds to the mixed ligand formation of $[Pd(tftm)(acac)]^+$. The remaining peak at *m/z* = 300 is representative of the fragmentation of $Pd(tftm)_2$ producing $[Pd(tftm)]^+$.

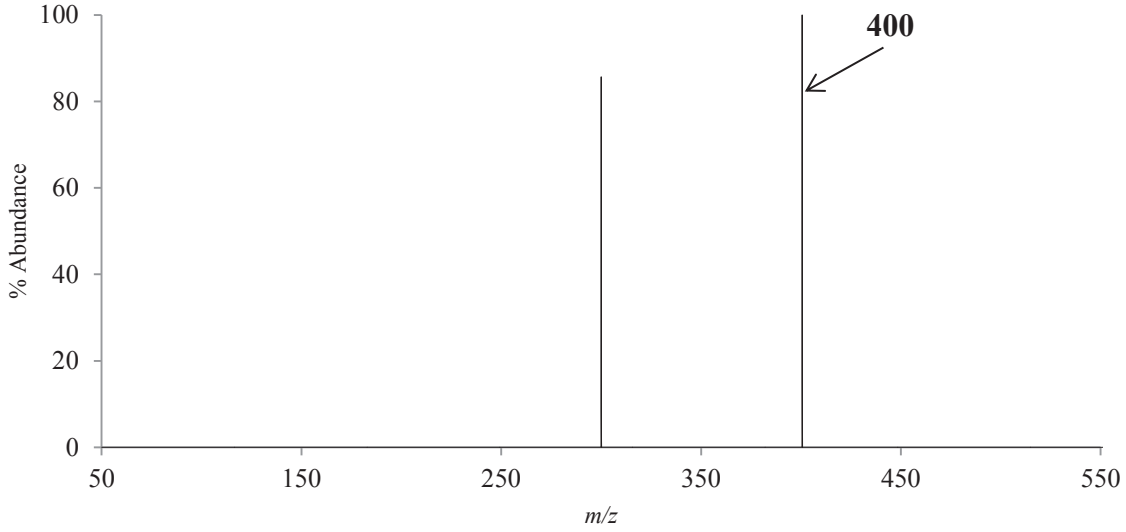

Figure 4.3: The positive mass spectrum obtained by scanning the third quadrupole after the selective reaction of *m/z* = 498 ($[Pd(tftm)_2]^+$) with neutral $Ni(acac)_2$ to produce the mixed ligand *m/z* = 400 ($[Pd(tftm)(acac)]^+$).

The next specific ion to be reacted with $Ni(acac)_2$ within the collision cell was $[Pd(tftm)(tftm - tBu)]^+$, *m/z* = 439. The proposed mechanism for this reaction is featured below in Equation 4.2.

$$[Pd(tftm - tBu)(tftm)]^+ + Ni(acac)_2 \rightarrow$$
$$[Ni(tftm)(acac)]^+ + Pd(acac)(tftm - tBu) \quad \text{(Eqn 4.2)}$$

The reaction result is shown below in Figure 4.4 where *m/z* = 352 is observed to form and corresponds to the mixed ligand formation of $[Ni(tftm)(acac)]^+$.

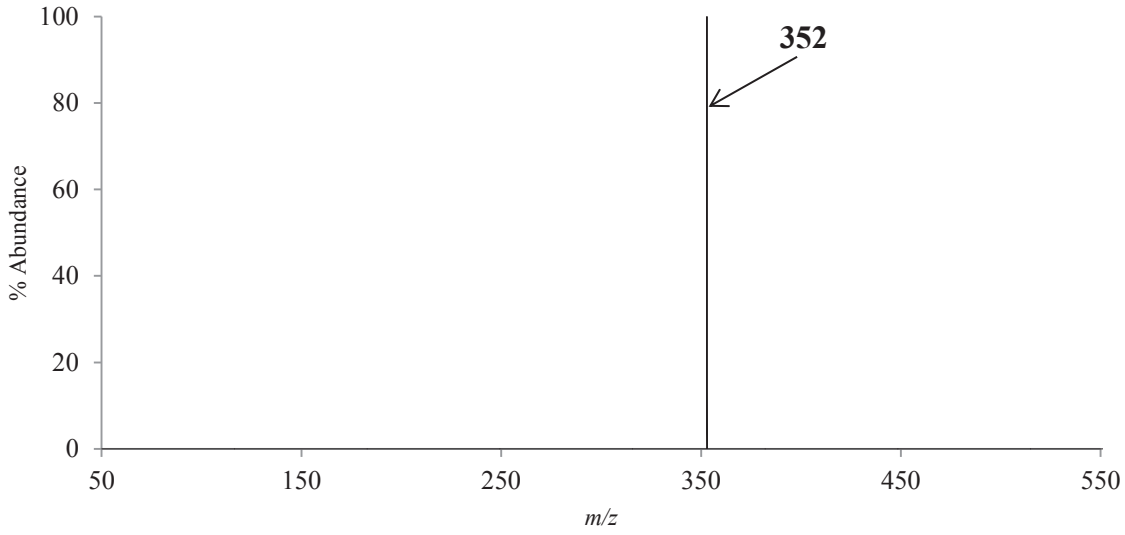

Figure 4.4: The positive mass spectrum obtained by scanning the third quadrupole after the selective reaction of *m/z* = 439 ($[Pd(tftm - tBu)(tftm)]^+$) with neutral $Ni(acac)_2$ to produce the mixed ligand *m/z* = 352 ($[Ni(tftm)(acac)]^+$).

The selective reaction between $[Pd(tftm)^+]$ with *m/z* = 300 and $Ni(acac)_2$ was performed next with the proposed mechanisms for this reaction featured in Equations 4.3 and 4.4.

$$[Pd(tftm)]^+ + Ni(acac)_2 \rightarrow [Ni(tftm)(acac)]^+ + Pd(acac) \quad \text{(Eqn 4.3)}$$

$$[Pd(tftm)]^+ + Ni(acac)_2 \rightarrow [Pd(tftm)(acac - CH_3)]^+ + Ni(acac) + CH_3 \quad \text{(Eqn 4.4)}$$

The mass spectrum of this reaction is found in Figure 4.5 where the mixed ligand formation at *m/z* = 352, which corresponds to $[Ni(tftm)(acac)]^+$, as well as the mixed ligand formation at *m/z* = 385, $[Pd(tftm)(acac - CH_3)]^+$, were observed. Similar to Figure 4.3, this reaction also shows the fragmentation product of *m/z* = 300 which corresponds to $[Pd(tftm)]^+$.

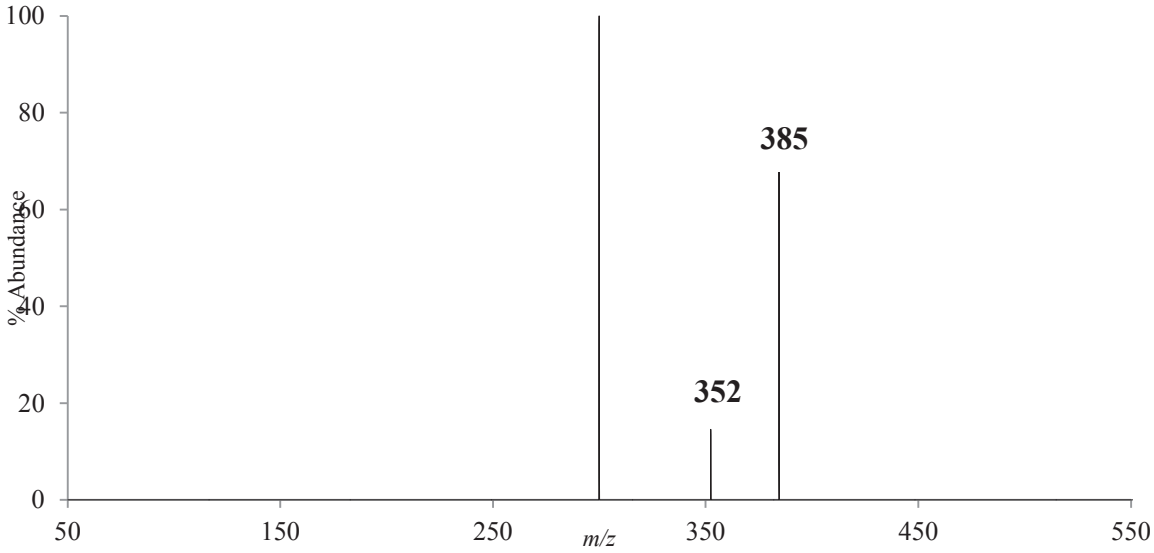

Figure 4.5: The positive mass spectrum obtained by scanning the third quadrupole following the selective reaction of *m/z* = 300 ($[Pd(tftm)]^+$) with neutral $Ni(acac)_2$ to produce *m/z* = 352 ($[Ni(tftm)(acac)]^+$) and *m/z* = 385 ($[Pd(tftm)(acac - CH_3)]^+$).

The mass selections of *m/z* = 429 ($[Pd(tftm)(tftm - CF_3)]^+$), *m/z* = 243 [$(Pd(tftm - tBu)]^+$, and *m/z* = 231 ($[Pd(tftm - CF_3)]^+$) did not produce any noteworthy results when using the collision cell and thus are not included.

The results of these selective reactions have provided insight into which palladium-containing β-diketonates fragments may play a role in the gas-phase ligand exchange reactions occurring with neutral $Ni(acac)_2$. The selective reaction of $[Pd(tftm)_2]^+$, *m/z* = 498, produced a mass spectrum showing the mixed ligand formation of $[Pd(tftm)(acac)]^+$, making it a possible key player in the co-sublimation reaction exchange as seen in Figure 4.3. The mass-selection of the fragment [Pd(tftm)(tftm – *t*Bu)]$^+$, m/z = 439, also appears to play a key role in gas-phase exchange as it is shown to produce the mixed ligand $[Ni(tftm)(acac)]^+$, *m/z* = 352 as seen in Figure 4.4 when reacted with neutral $Ni(acac)_2$. Figure 4.5 shows that the fragment $[Pd(tftm)]^+$ may be the most important in the role of gas-phase exchange as it produces two mixed ligand products, $[Ni(tftm)(acac)]^+$, *m/z* = 352, as well as $[Pd(tftm)(acac - CH_3)]^+$, *m/z* = 385.

4.2.5 Nickel Diethylacetylacetonate ($Ni(eeac)_2$)

Nickel diethylacetylacetonate ($Ni(eeac)_2$) is a novel metal β-diketonate complex that is reported herein for the first time. $Ni(eeac)_2$ was investigated using co-sublimation reactions as well as selective reactions within the collision cell in order to gain more insight into the properties and characteristics of this particular complex.

Figure 4.6 is a representative positive mass spectrum of $Ni(eeac)_2$ and is presented for the first time with a mass range of *m/z* = 100-500, the same shortened range used earlier in Figure 4.1. This spectrum is also presented in the vertically stacked co-sublimation spectra found in Figure 4.7 (a) with a mass range of *m/z* = 50 – 550 for comparative purposes. This shortened mass range again illustrates the characteristics of this complex by minimizing the abundance of the *m/z* = 57 ion signal peak that

overwhelms the data given its relatively high intensity. The loss of a *t*Bu group (*m/z* = 57) is a common loss channel for these complexes and can minimize the importance of other species that are present, but at a lower ion intensity. In Figure 4.6, the peak at *m/z* = 312 is the parent peak and corresponds to $[Ni(eeac)_2]^+$. The dominant peak at *m/z* = 283 comes from the loss of an ethyl group from one of the ligands attached to the nickel center. This ion signal was selected as the most abundant peak and thereafter was used as the reference peak when calculating the relative abundances featured below in Table 4.3. The only other fragment of importance is the peak at *m/z* = 185, which corresponds to $[Ni(eeac)]^+$.

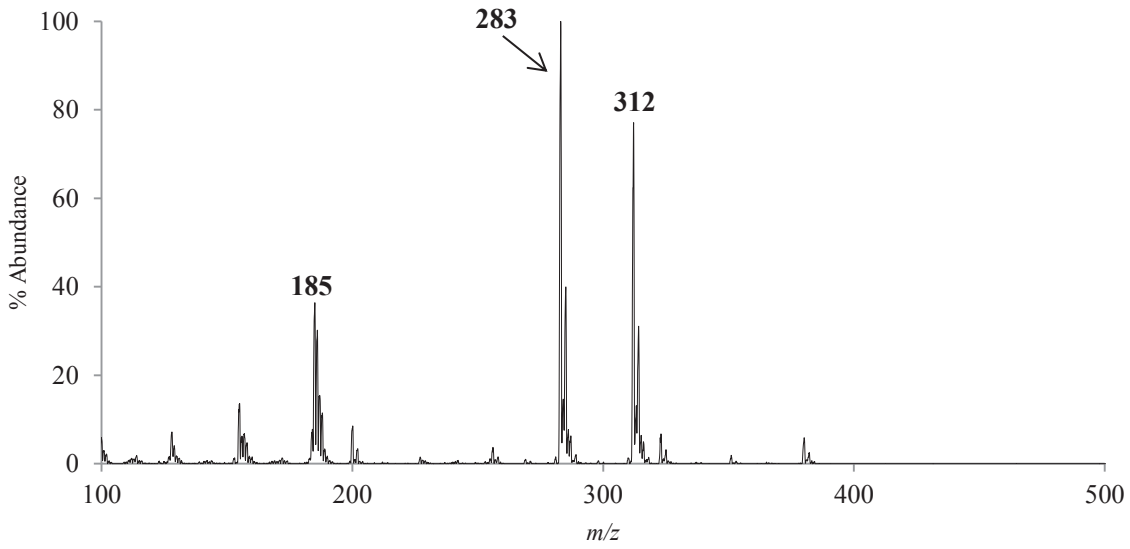

Figure 4.6: The 70 eV positive EI mass spectrum of $Ni(eeac)_2$, showing only the range between *m/z* = 100 and *m/z* = 500 to exhibit more isotopic abundance without the interference of the background *m/z* = 57 peak corresponding to the loss of a *t*Bu group.

Species	*m/z*	Relative Abundance
$[Ni(eeac)_2]^+$	312	77
$[Ni(eeac)(eeac - Et)]^+$	283	100
$[Ni(eeac)]^+$	185	39

Table 4.3: The fragmentation species and corresponding relative abundances of the mass spectral analysis of $Ni(eeac)_2$ as presented in Figure 4.6.

4.2.6 The Co-Sublimation of $Pd(tftm)_2$ & $Ni(eeac)_2$

The mass spectra presented in Figure 4.7 are vertically stacked in order to better visualize the extent of ligand exchange. The top portion, Figure 4.7 (a), features the positive EI mass spectrum of $Ni(eeac)_2$ showing typical fragmentation patterns such as the parent peak at *m/z* = 312 , the loss of an ethyl group at *m/z* = 283, and the loss of a diethylacetylacetonate ligand at *m/z* = 185. The middle portion, Figure 4.7 (b) shows the spectrum of $Pd(tftm)_2$ which resembles Figure 4.1, but over a different mass range. The bottom portion, Figure 4.7 (c), corresponds to the spectrum from the co-sublimation of both $Pd(tftm)_2$ and $Ni(eeac)_2$ using a two-looped filament.

It is important to note that there are peaks present in the co-sublimation spectrum that are not featured in the previous single species spectra which is a clear indication of gas-phase ligand exchange. Those species that underwent any amount of ligand exchange, which includes partial exchanges, mixed ligand formations, and complete exchanges are labeled within the spectra and are highlighted in bold. The *m/z* values and relative abundances for the fragmentation of the single species, the co-sublimation species, as well as the exchange products are featured in Table 4.4. The relative abundances were calculated in relation to the most intense peak of importance, that is, the

peak with the most intensity that is either a partial exchange, mixed ligand, or full exchange product. For example, in Figure 4.7 (c), the most intense peak is *m/z* = 57. However, *m/z* = 391 was selected as the base peak for the relative abundance calculations since it was the next highest intense peak and corresponds to $[Ni(tftm)(tftm - tBu)]^+$ which is a ligand exchange product. Results from this co-sublimation experiment show partial, mixed, and full ligand exchange for both the nickel and the palladium species, however the nickel complexes appear to more readily undergo the complete ligand exchange which is similar to the results in Section 4.2.3. The relative abundances of the single reactions as well as the co-sublimation reactions can be found in Table 4.4.

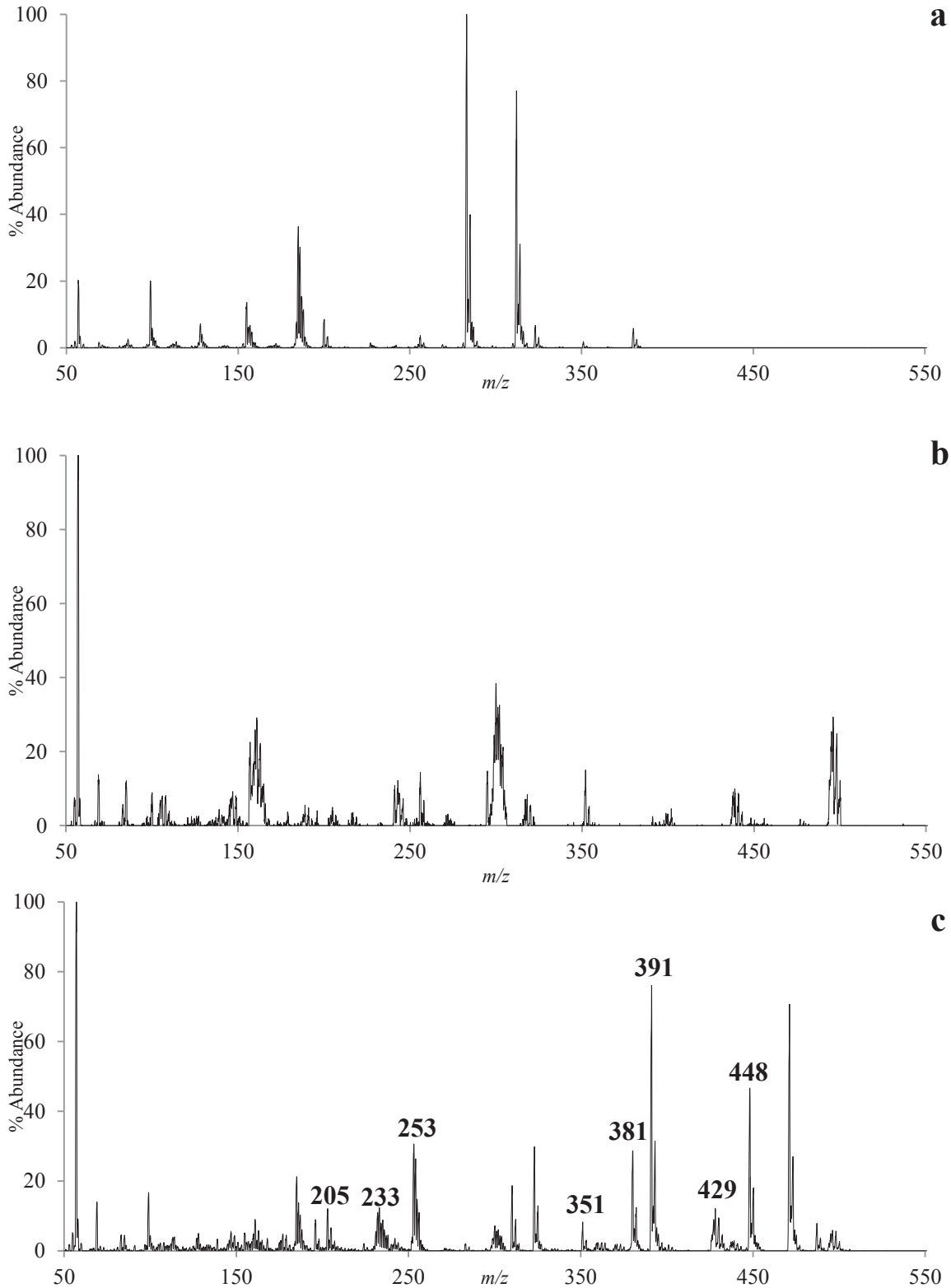

Figure 4.7: The 70 eV positive EI mass spectra of (a) $Ni(eeac)_2$, (b) $Pd(tftm)_2$, and (c) the co-sublimation of $Pd(tftm)_2$ and $Ni(eeac)_2$. Mixed ligand formations or ligand exchange peaks are highlighted in bold.

	Mass	Mass	NiL''$_2$	PdL'$_2$	NiL''$_2$ & PdL'$_2$	NiL''$_2$ & PdL'$_2$
Species	Ni	Pd	Ni	Pd	Ni	Pd
ML''$_2$	312	360	77		12	4
ML''$_2$-Et	283	331	100		3	<1
ML''	185	233	39		31	17
ML'' - Et	156	205	7		4	10
ML'$_2$	448	496		65	67	9
ML'$_2$-*t*Bu	391	439		20	100	4
ML'$_2$-CF$_3$	379	429		<1	3	4
ML'	253	300		100	44	9
ML'-*t*Bu	196	243		31	13	2
ML'-CF$_3$	184	231		<1	4	8
ML'L''	381	429			10	16
M(L'-tBu)L''	323	371			40	2
M(L'-CF$_3$)L''	311	359			4	3
ML'(L''-Et)	351	399			10	1

L' = (tftm); L'' = (eeac)

Table 4.4: The relative mass spectrometric abundances of nickel and palladium β-diketonate complexes as well as the co-sublimation experiment as presented in Figure 4.7.

4.2.7 Selective Reaction of Pd(tftm)$_2$ & Ni(eeac)$_2$

The selective reactions performed in this study utilized the collision cell of the mass spectrometer where specific cations, including the intact $[Pd(tftm)_2]^+$ species, and fragments including $[Pd(tftm)(tftm - tBu)]^+$, $[Pd(tftm)(tftm - CF_3)]^+$, $[Pd(tftm)]^+$, $[Pd(tftm - tBu)]^+$, and $[Pd(tftm - CF_3)]^+$ were all individually mass-selected and allowed to enter the collision cell and react with neutral Ni(eeac)$_2$. The third quadrupole scans the entire region for all products of the selective reaction and the spectra included below in Figures 4.8 – 4.16 show the results of these reactions. The collision chamber was purged with the gaseous Ni(eeac)$_2$ prior to each run. Figures 4.8 and 4.9 show the results of the reaction selecting $[Pd(tftm)_2]^+$ at *m/z* = 498. By selecting this peak and allowing it to react with the gaseous Ni(eeac)$_2$, Figure 4.8 shows that a product of *m/z* = 381 is

observed. This corresponds to the mixed ligand formation of $[Ni(tftm)(eeac)]^+$. The proposed mechanism for this reaction is found below in Equation 4.5. Figure 4.8 and 4.9 are showing the same reaction result, but at different detection times along the chromatograph from the scan of the third quadrupole. Capturing data at various times along the temperature ramp of the insertion probe allows for a variation of the ion concentration that is reacting.

$$[Pd(tftm)(tftm)]^+ + Ni(eeac)_2 \rightarrow [Ni(tftm)(eeac)]^+ + Pd(eeac)(tftm) \qquad \text{(Eqn 4.5)}$$

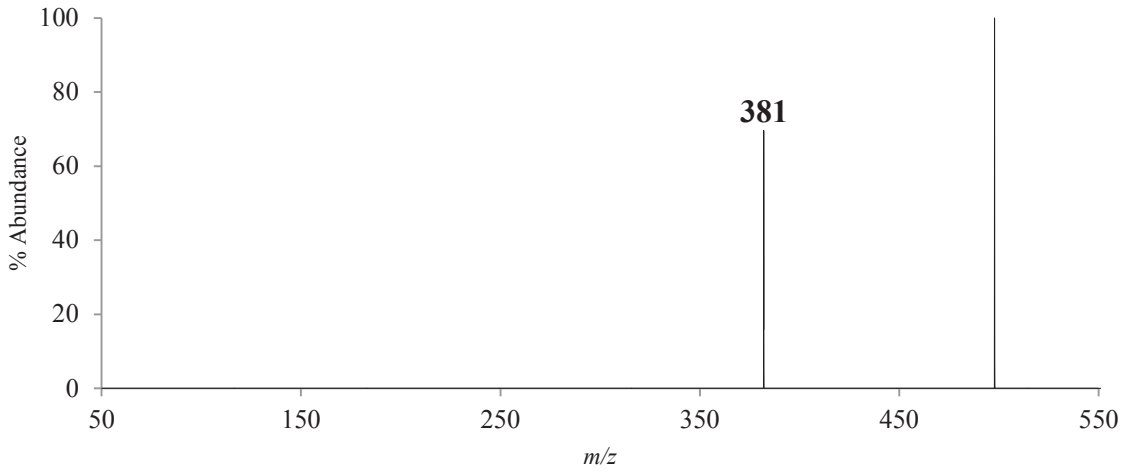

Figure 4.8: The positive mass spectrum obtained by scanning the third quadrupole following the selective reaction of *m/z* = 498 ($[Pd(tftm)_2]^+$) with neutral $Ni(eeac)_2$ to produce the mixed ligand *m/z* = 381 ($[Ni(tftm)(eeac)]^+$). The ion signal at *m/z* = 498 is the mass-selected species.

The mass selection of *m/z* = 498 for the selective reaction also revealed that *m/z* = 351 was produced, corresponding to the $[Ni(tftm)(eeac - Et)]^+$ fragment. The proposed mechanism for this reaction is shown below in Equation 4.6, and the spectrum is presented in Figure 4.9.

$$[Pd(tftm)(tftm)]^+ + Ni(eeac)_2 \rightarrow [Ni(tftm)(eeac - Et)]^+ + Pd(tftm)(eeac) + Et \qquad \text{(Eqn 4.6)}$$

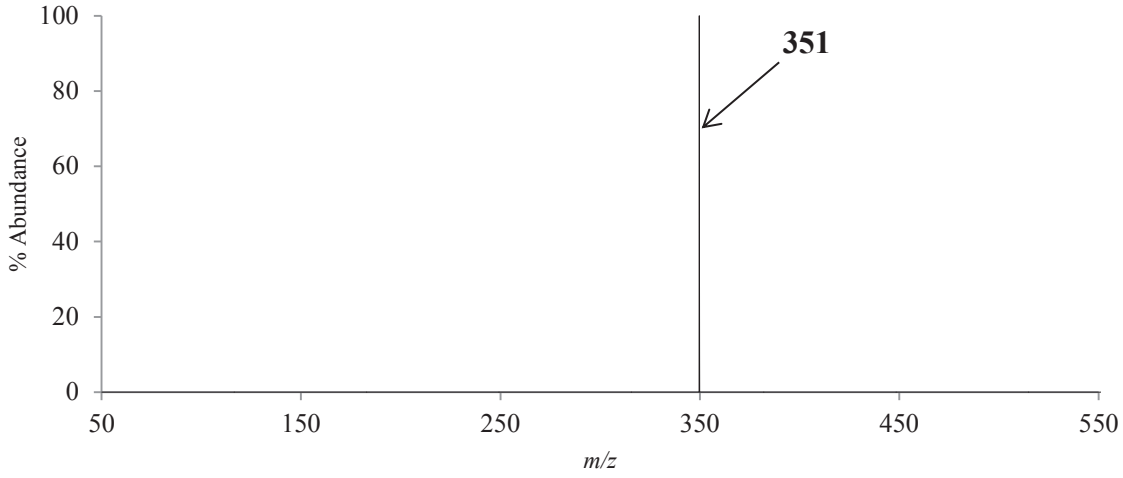

Figure 4.9:The positive mass spectrum obtained by scanning the third quadrupole after the selective reaction of *m/z* = 498 ($[Pd(tftm)_2]^+$) with neutral $Ni(eeac)_2$ to produce the mixed ligand fragment *m/z* = 351 ($[Ni(tftm)(eeac - Et)]^+$).

The mass selection of $[Pd(tftm)(tftm - t\text{Bu})]^+$, at m/z = 439, also produced two different gas-phase ligand exchange products that can be seen below in Figure 4.10 and Figure 4.11. The first product is the partial exchange product of $[Ni(tftm)]^+$ at m/z = 253 with a proposed reaction mechanism presented in Equation 4.7

$$[Pd(tftm - t\text{Bu})(tftm)]^+ + Ni(eeac)_2 \rightarrow$$

$$[Ni(tftm)]^+ + Pd(tftm - t\text{Bu})(eeac) + (eeac) \qquad \text{(Eqn 4.7)}$$

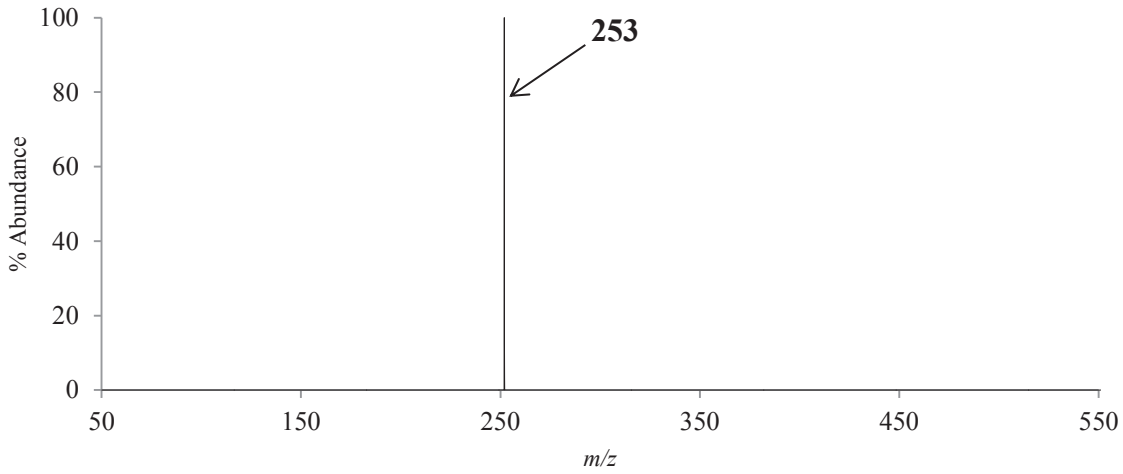

Figure 4.10: The positive mass spectrum obtained by scanning the third quadrupole after the selective reaction of m/z = 439 ($[Pd(tftm)(tftm - tBu)]^+$) with neutral $Ni(eeac)_2$ to produce the mixed ligand fragment m/z = 253 ($[Ni(tftm)]^+$).

The mass selection of $[Pd(tftm)(tftm - tBu)]^+$ at *m/z* = 439 also produced an ion signal at *m/z* = 381 which corresponds to $[Ni(tftm)(eeac)]^+$. The proposed mechanism for this reaction can be found in Equation 4.8 and the spectrum appears in Figure 4.11.

$$[Pd(tftm - tBu)(tftm)]^+ + Ni(eeac)_2 \rightarrow$$

$$[Ni(tftm)(eeac)]^+ + Pd(eeac)(tftm - tBu) \qquad \text{(Eqn 4.8)}$$

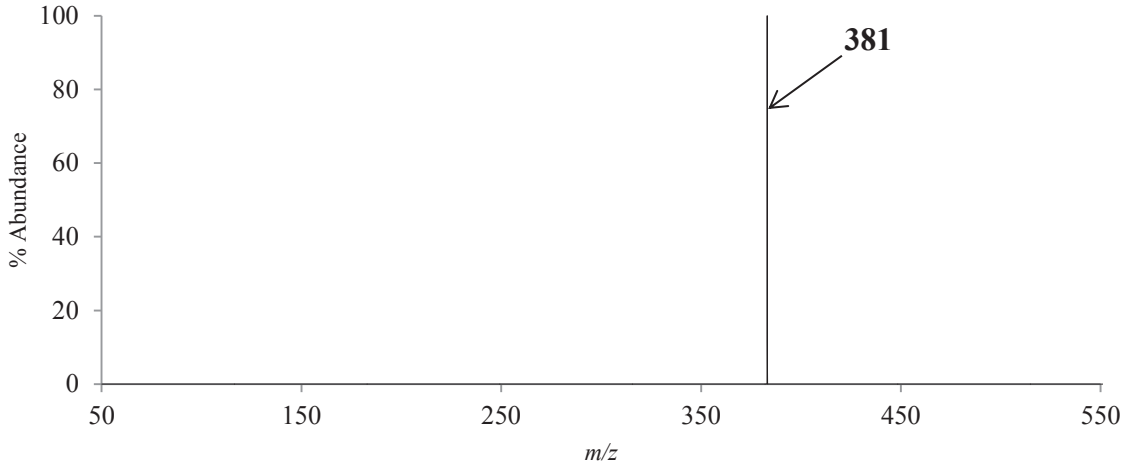

Figure 4.11: The positive mass spectrum obtained by scanning the third quadrupole after the selective reaction of *m/z* = 439 ($[Pd(tftm)(tftm - tBu)]^+$) with neutral $Ni(eeac)_2$ to produce the mixed ligand *m/z* = 381 ($[Ni(tftm)(eeac)]^+$).

The mass selection of $[Pd(tftm)(tftm - CF_3)]^+$ at *m/z* = 429 also showed two different gas-phase ligand exchange products. The proposed reaction mechanisms for these reactions can be found in Equations 4.9 and 4.10. Figure 4.12 below shows a complete exchange of the trifluorotrimethylacetylacetonate ligand from $[Pd(tftm)_2]^+$ to $[Ni(tftm)_2]^+$. This exchange is observed by the peak located at *m/z* = 448. It is apparent from Equation 4.9 that there must be another explanation for this reaction occurring since there are not two intact *tftm* ligands to begin with to form a complete ligand exchange product of $Ni(tftm)_2$. The involvement of free radicals, residual ligands, and/or fragment species remaining in the collision cell, or simple molar ratios, could help explain the proposed reaction. It is still worth noting the reaction in Figure 4.12 since it does show evidence of the ligand exchange occurring with the ion signal at *m/z* = 448.

$$[Pd(tftm - CF_3)(tftm)]^+ + Ni(eeac)_2 + CF_3 \rightarrow$$
$$[Ni(tftm)(tftm)]^+ + Pd(eeac)_2 \qquad \text{(Eqn 4.9)}$$

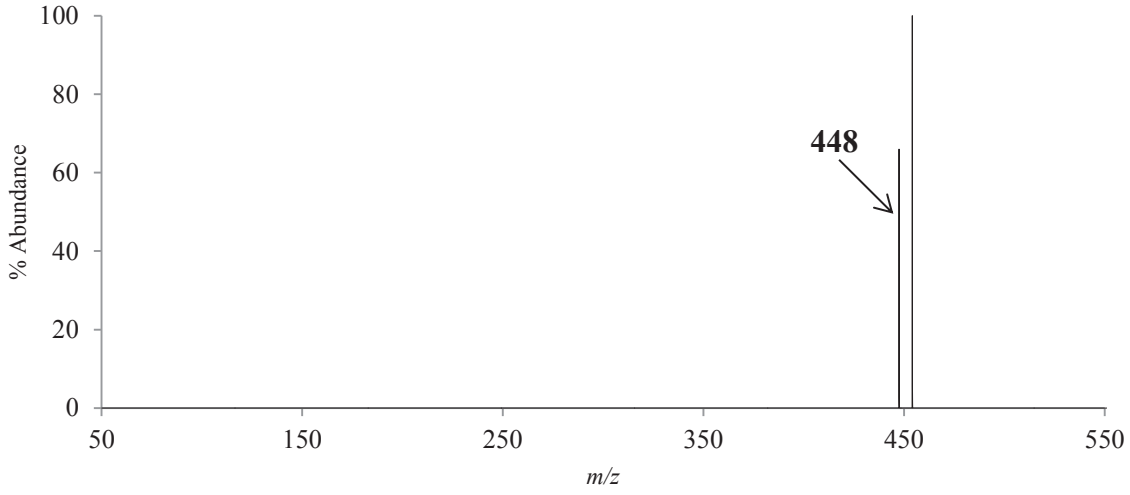

Figure 4.12:The positive mass spectrum obtained by scanning the third quadrupole after the selective reaction of *m/z* = 429 ($[Pd(tftm)(tftm - CF_3)]^+$) with neutral $Ni(eeac)_2$ to produce the complete ligand exchange product of *m/z* = 448 ($[Ni(tftm)_2]^+$).

The mass selection of *m/z* = 429 also produced the partial ligand exchange product of $[Ni(tftm)]^+$ at *m/z* = 253. The spectrum expressing these results can be found in Figure 4.13.

$$[Pd(tftm - CF_3)(tftm)]^+ + Ni(eeac)_2 \rightarrow$$
$$[Ni(tftm)]^+ + Pd(tftm - CF_3)(eeac) + (eeac) \qquad \text{(Eqn 4.10)}$$

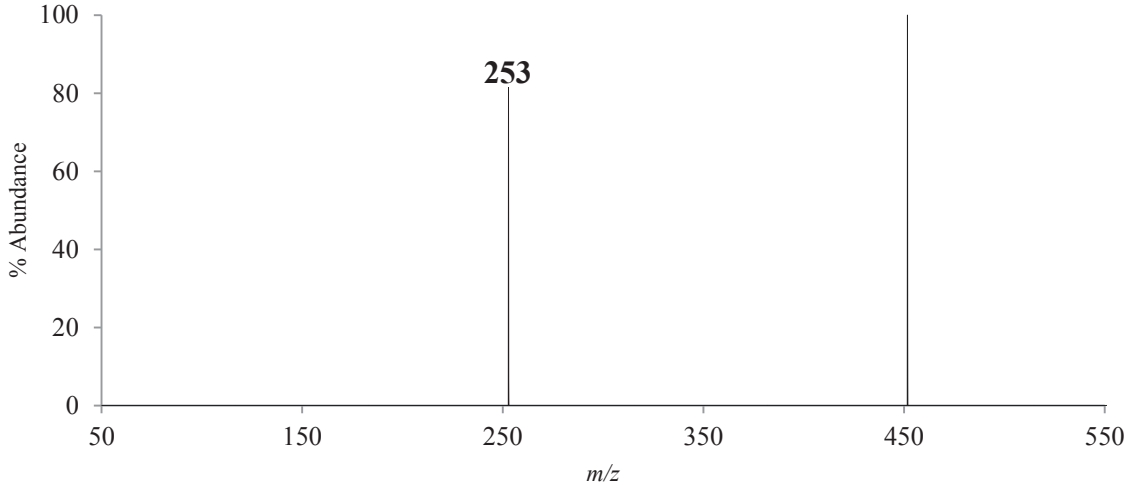

Figure 4.13: The positive mass spectrum obtained by scanning the third quadrupole after the selective reaction of *m/z* = 429 ($[Pd(tftm)(tftm - CF_3)]^+$) with neutral $Ni(eeac)_2$ to produce the partial gas-phase exchange product of *m/z* = 253 ($[Ni(tftm)]^+$).

The mass selection of $[Pd(tftm)]^+$ at *m/z* = 300 only produced a single gas-phase exchange product with neutral $Ni(eeac)_2$. The proposed mechanism for this reaction can be found in Equation 4.11 and the spectrum is shown in Figure 4.14. The partial exchange product of $[Ni(tftm)]^+$ at *m/z* = 253 is present in many other selective reaction spectra presented in this Chapter.

$$[Pd(tftm)]^+ + Ni(eeac)_2 \rightarrow [Ni(tftm)]^+ + Pd(eeac)_2 \qquad \text{(Eqn 4.11)}$$

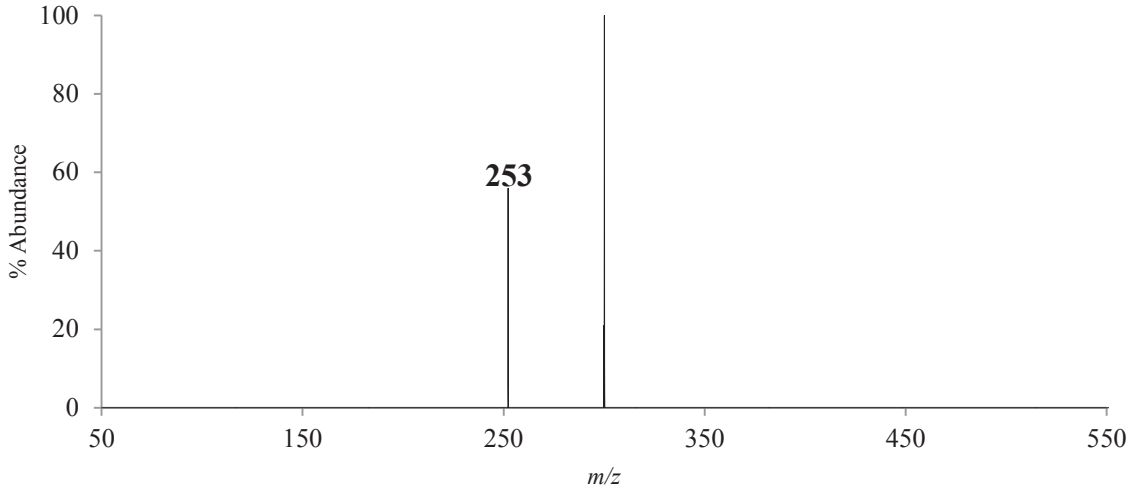

Figure 4.14: The positive mass spectrum obtained by scanning the third quadrupole after the selective reaction of *m/z* = 300 ($[Pd(tftm)]^+$) with neutral $Ni(eeac)_2$ to produce the partial gas-phase ligand exchange product of *m/z* = 253 ($[Ni(tftm)]^+$).

The mass selection of $[Pd(tftm - CF_3)]^+$ at *m/z* = 231 showed two resulting gas-phase ligand exchange products. The proposed mechanisms for these reactions can be found in Equations 4.12 and 4.13 and the spectra are shown in Figures 4.15 and 4.16. It is interesting that this selective reaction was just as successful at producing exchange products as the previous selective reaction simply because the relative initial abundance of this fragment in both the single $Pd(tftm)_2$ spectrum as well as the co-sublimation of $Pd(tftm)_2$ and $Ni(eeac)_2$ showed such a low relative abundance as seen in Table 4.4. Even more interesting is the fact that previously, more exchanges involving the nickel metal were observed. The results presented below in Figures 4.15 and 4.16 are the contrary. Figure 4.15 shows an ion signal at *m/z* = 429, which corresponds to the mixed ligand formation of $[Pd(tftm)(eeac)]^+$. Similar to Equation 4.9, however, the formation of the mixed ligand expressed in Equation 4.12 is shown to be occurring without starting with an intact (tftm) ligand. For this reason, it is most likely that the ion signal at *m/z* = 429 in Figure 4.15 is actually representative of the isobaric peak for $[Pd(tftm)(tftm - CF_3)]^+$ and not the selective reaction product. Since there is still a possibility that it is representative of mixed ligand exchange, it has still been included in this study.

$$[Pd(tftm - CF_3)]^+ + Ni(eeac)_2 + CF_3 \rightarrow [Pd(tftm)(eeac)]^+ + Ni(eeac) \qquad \text{(Eqn 4.12)}$$

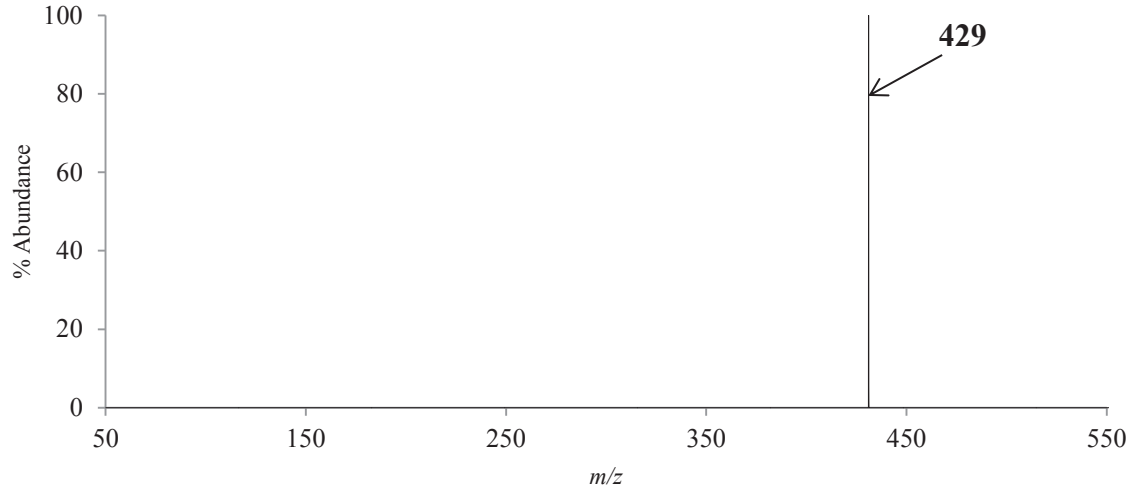

Figure 4.15: The positive mass spectrum obtained by scanning the third quadrupole after the selective reaction of *m/z* = 231 ($[Pd(tftm - CF_3)]^+$) with neutral $Ni(eeac)_2$ to produce the mixed ligand *m/z* = 429 ($[Pd(tftm)(eeac)]^+$).

The mass selection of $[Pd(tftm - CF_3)]^+$ at *m/z* = 231 also produced a partial gas-phase ligand exchange product as seen below in Figure 4.16 showing $[Pd(eeac)]^+$ at *m/z* = 233.

$$[Pd(tftm - CF_3)]^+ + Ni(eeac)_2 \rightarrow [Pd(eeac)]^+ + Ni(tftm - CF_3)(eeac) \qquad \text{(Eqn 4.13)}$$

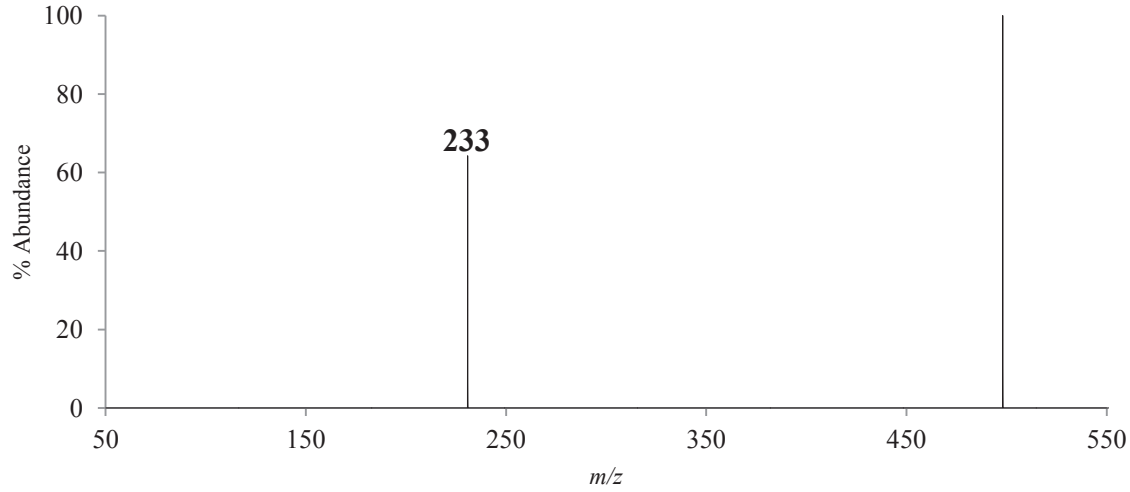

Figure 4.16: The positive mass spectrum obtained by scanning the third quadrupole after the selective reaction of *m/z* = 231 ($[Pd(tftm - CF_3)]^+$) with neutral $Ni(eeac)_2$ to produce the partial gas-phase ligand exchange product of *m/z* = 233 ($[Pd(eeac)]^+$).

The results of these selective reactions have provided insight into which palladium-containing β-diketonates fragments may play a role in the gas-phase ligand exchange reactions occurring with neutral $Ni(eeac)_2$. The selective reaction of $[Pd(tftm)_2]^+$, *m/z* = 498, produced two mass spectra showing the mixed ligand fragment formation of $[Ni(tftm)(eeac)]^+$ and $[Ni(tftm)(eeac - Et)]^+$ as seen in Figures 4.8 and 4.9 respectively. Given the prevalence of these two mixed ligand species, $[Pd(tftm)_2]^+$ may play a predominant role during the co-sublimation reaction exchange of $Pd(tftm)_2$ and $Ni(eeac)_2$. The mass-selection of the fragment $[Pd(tftm)(tftm - t\text{Bu})]^+$, *m/z* = 439, also appears to play a key role in gas-phase exchange as it is shown to produce both the partial ligand exchange product of $[Ni(tftm)]^+$ at *m/z* = 253 in Figure 4.10 as well as the mixed ligand $[Ni(tftm)(eeac)]^+$ at *m/z* = 352 as seen in Figure 4.11.

The selective reaction with the mass selection of $[Pd(tftm)(tftm\text{-}CF_3)]^+$ at *m/z* = 429 may play an important role in the gas-phase exchange reactions with the possible production of $[Ni(tftm)_2]^+$ at *m/z* = 448 seen in Figure 4.12. However, more evidence is necessary since the fragment peak alone is not sufficient to produce $[Ni(tftm)_2]^+$ meaning that other participants in the reaction are necessary. The partial ligand formation of $[Ni(tftm)]^+$ at *m/z* = 253 is shown in Figure 4.13 from the selective reaction with *m/z* = 429. The fragment $[Pd(tftm)]^+$ at *m/z* = 300 may also play a more minor role in ligand exchange during co-sublimation. While the formation of $[Ni(tftm)]^+$ is observed to occur in the collision cell, the ion intensity is quite low given the amount of fragmentation that is necessary to form this species in the first place. The fragment of $[Pd(tftm - CF_3)]^+$ at *m/z* = 231 also plays a minor role in gas-phase ligand exchange as it only provides the possibility of the formation of $[Pd(tftm)(eeac)]^+$ at *m/z* = 429 as seen in Figure 4.15. The

fragment of $[Pd(tftm - tBu)]^+$ did not produce appreciable data and is thus not thought to play a major role in the gas-phase ligand exchange during the co-sublimation of $Pd(tftm)_2$ and $Ni(eeac)_2$.

4.2.8 Nickel hexafluoroacetylacetonate ($Ni(hfac)_2$)

For more details regarding nickel hexafluoroacetylacetonate ($Ni(hfac)_2$) and its corresponding fragmentation behavior, please refer to Hunter et.al.[17] A representative cationic mass spectrum of $Ni(hfac)_2$ is featured in Section 4.2.7 in Figure 4.17 (a).

4.2.9 The Co-Sublimation of $Pd(tftm)_2$ & $Ni(hfac)_2$

The mass spectra presented in Figure 4.17 is vertically stacked to better visualize the extent of ligand exchange occurring. The top portion, Figure 4.17 (a), features the positive EI mass spectrum of $Ni(hfac)_2$ showing typical fragmentation patterns such as the parent peak at m/z = 472, the dominant peak representing the loss of a CF_3 group at m/z = 403, the loss of an hfac ligand at m/z = 265. Fluorine migration giving rise to an ion at m/z = 215 ($[Ni(hfac - CF_2)]^+$, which will be discussed in more detail later in this Chapter, and the loss of another CF_3 group at m/z = 196 are also both observed. The middle portion, Figure 4.17 (b), shows the positive mass spectrum of $Pd(tftm)_2$ which resembles Figure 4.1, but over a different mass range. The bottom portion, Figure 4.17 (c), corresponds to the mass spectrum from the co-sublimation of both $Pd(tftm)_2$ and $Ni(hfac)_2$ using a two-looped filament.

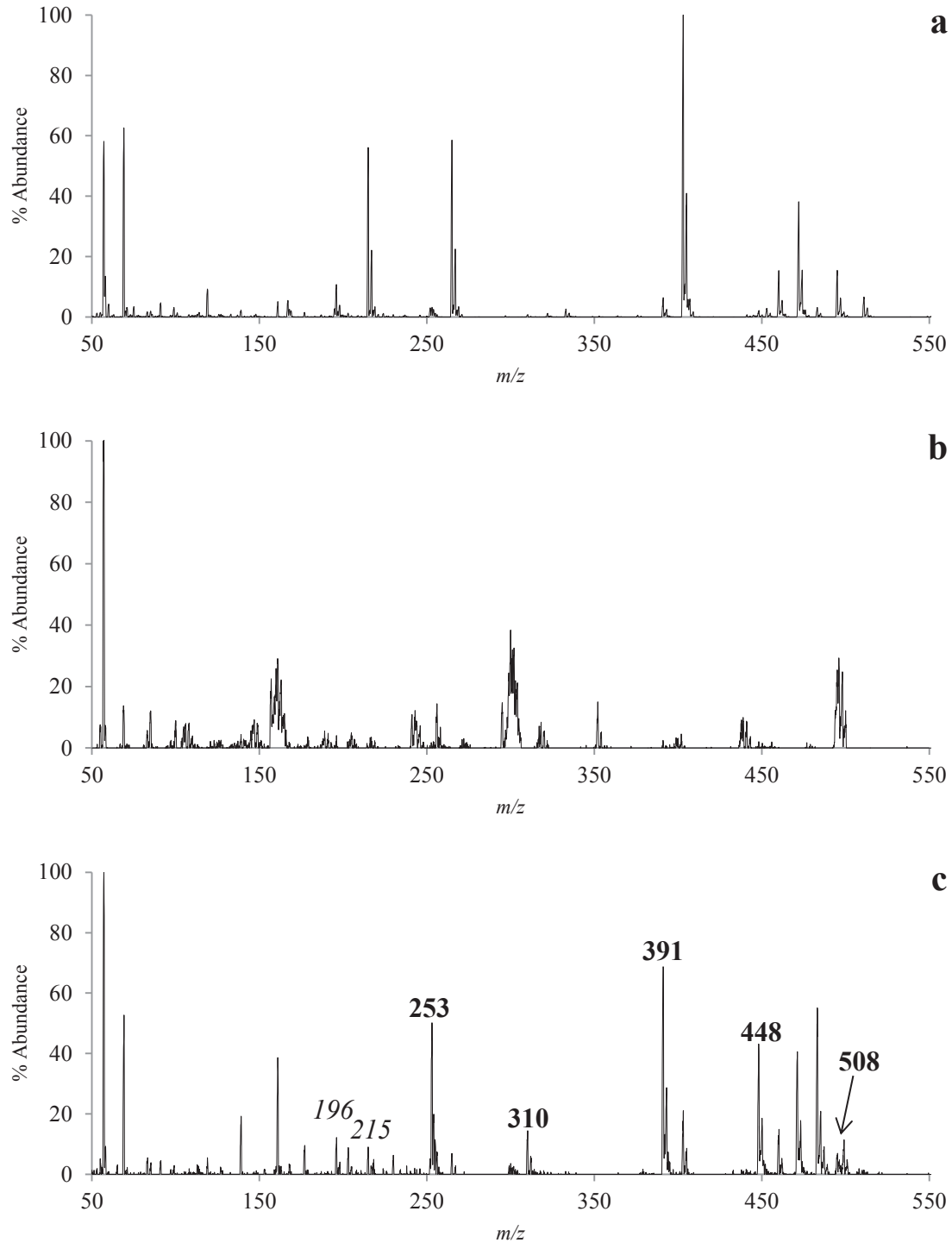

Figure 4.17: The 70 eV positive EI mass spectra of (a) $Ni(hfac)_2$, (b) $Pd(tftm)_2$, and (c) the co-sublimation of $Pd(tftm)_2$ and $Ni(hfac)_2$. Mixed ligand or ligand exchange peaks are highlighted in bold, with other peaks of interest italicized.

It is important to note that there are peaks present in the co-sublimation spectrum that are not featured in the previous single spectra which is a clear indication of gas-phase ligand exchange. Those species that underwent any amount of ligand exchange, which includes partial exchanges, mixed ligand formations, and complete exchanges are labeled within the spectra and highlighted in bold. The *m/z* values for the fragmentation of the single species as well as the co-sublimation species are featured below in Table 4.5. The relative abundances were calculated in relation to the most intense peak of importance, that is, the peak with the most intensity that is either a partial exchange, mixed ligand, or full exchange product.

For Figure 4.17 (c), the most intense peak is *m/z* = 57. However, *m/z* = 391 was selected as the base peak for the relative abundance calculations since it was the next highest intense peak and corresponds to both $[Ni(tftm)(tftm - tBu)]^+$ and $[Ni(tftm)(hfac - CF_3)]^+$ which both indicate isobaric ligand exchange products. Results from this co-sublimation experiment show partial, mixed, and full ligand exchange for both the nickel and the palladium species. However, the ligand exchanges involving nickel species is more dominant and is similar to the results presented in Sections 4.2.3 and 4.2.5. The relative abundances of the single reactions as well as the co-sublimation reactions can be found below in Table 4.5. The italicized rows correspond to isobaric peaks in the co-sublimation spectrum.

An interesting peak is the one located at *m/z* = 310 as observed in Figure 4.17 (c) and described in Table 4.5. This mass corresponds to $[Ni(tftm) + tBu]^+$ and was previously observed by Hunter et.al.[17] Further analysis of this co-sublimation reaction in the collision cell may provide information on the mechanism of the mixed ligand

formation as well as which fragmentation event may lead to the production of what corresponds to $[Ni(tftm) + tBu]^+$.

	Mass	Mass	NiL'''$_2$	PdL'$_2$	NiL'''$_2$ & PdL'$_2$	NiL'''$_2$ & PdL'$_2$
Species	Ni	Pd	Ni	Pd	Ni	Pd
ML'''$_2$	472	520	40		13	<1
ML'''$_2$-CF$_2$	422	470	0		0	3
ML'''$_2$-CF$_3$	403	451	100		25	6
ML'''$_2$ - 2CF$_3$	334	382	<1		0	0
ML'''	265	313	53		8	<1
ML''' - CF$_2$	215	263	51		<1	0
ML''' - CF$_3$	196	244	11		15	<1
ML''' - 2CF$_3$	127	175	<1		3	<1
ML'$_2$	448	496		65	63	6
ML'$_2$-tBu	*391*	*439*		*20*	*100*	*<1*
ML'$_2$-CF$_3$	379	429		<1	1	0
ML'	253	300		100	67	4
ML'-*t*Bu	196	243		31	15	1
ML'-CF$_3$	184	231		<1	<1	0
ML' + *t*Bu	310	358		0	19	0
ML'L'''	460	508			21	1
M(L'- *t*Bu)L'''	403	451			25	6
ML'(L'''-CF$_2$)	410	458			0	<1
ML'(L''' - CF$_3$)	*391*	*439*			*100*	*<1*
ML'(L''' - 2CF$_3$)	322	370			<1	0

L' = (tftm); L''' = (hfac)

Table 4.5: The mass spectrometric relative abundances of nickel and palladium β-diketonate complexes as well as the co-sublimation products of $Pd(tftm)_2$ and $Ni(hfac)_2$ as presented in Figure 4.17.

Though not involved in the co-sublimation ligand exchange, the peak of *m/z* = 215 is of interest because it shows evidence of fluorine migration. That is, there is the loss of a CF_2 group as opposed to the more common loss of CF_3. For a full description of fluorine migration, see Hunter[17] and references therein. Hunter had also observed

fluorine migration in co-sublimation reactions involving hexafluoroacetylacetonate complexes. Fluorine migration has been observed in these types of compounds for many years, however, an adequate mechanism for fluorine loss has yet to be determined.

Perhaps one of the most interesting peaks in this co-sublimation reaction is the peak located at *m/z* = 196 in Figure 4.17 (c). This peak is isobaric, meaning it represents a mass overlap of the ligand exchange product of $[Ni(tftm - tBu)]^+$ with the fragment $[Ni(hfac - CF_3)]^+$. Without a collision cell analysis, it is nearly impossible to determine a ratio of these products in relation to one another. Additional analysis is necessary to adequately describe the co-sublimation reaction.

4.2.10 Selective Reactions of $Pd(tftm)_2$ & $Ni(hfac)_2$

The selective reactions of $Pd(tftm)_2$ and $Ni(hfac)_2$ were enacted using the same parameters and experimental design as observed in Sections 4.2.3 and 4.2.7. The collision chamber was purged with the gaseous $Ni(hfac)_2$ prior to each run. The results of these selective reactions can be seen below in Figures 4.18 – 4.23.

The mass selections of the parent peak of *m/z* = 498, or the loss of a *t*Bu group at *m/z* = 439 did not reveal any appreciable ion intensity. The mass selection of $[Pd(tftm)(tftm - CF_3]^+$ at *m/z* = 429 did, however, show the production of two different complete gas-phase ligand exchanges as presented in Figures 4.18 and 4.19. The proposed mechanisms for these reactions are found in Equations 4.14 and 4.15 while Figure 4.18 shows the complete ligand exchange and formation of $[Ni(tftm)_2]^+$ at *m/z* = 448 from the selection of *m/z* = 429. This reaction, like those presented in Equations 4.9

and 4.12, need still need further analysis to definitively show that the evidence of the ligand exchange product is in fact just that, and not formed through a different process.

$$[Pd(tftm - CF_3)(tftm)]^+ + Ni(hfac)_2 + CF_3 \rightarrow$$
$$[Ni(tftm)(tftm)]^+ + Pd(hfac)_2 \qquad \text{(Eqn 4.14)}$$

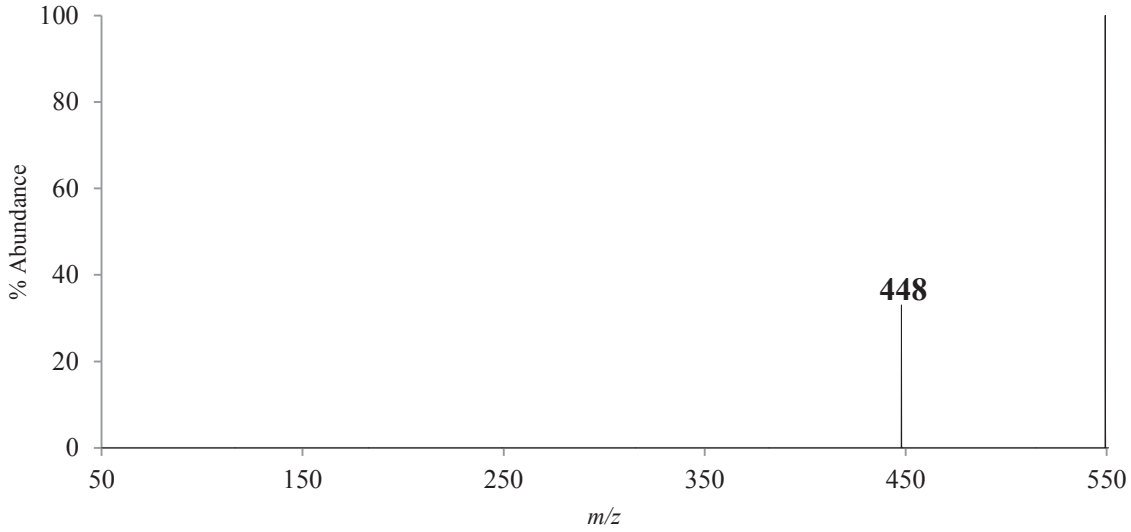

Figure 4.18: The positive mass spectrum obtained by scanning the third quadrupole after the selective reaction of *m/z* = 429 ($[Pd(tftm)(tftm - CF_3)]^+$) with neutral $Ni(hfac)_2$ to produce the complete gas-phase ligand exchange product of *m/z* = 448 ($[Ni(tftm)_2]^+$).

The selective reaction mass-selecting *m/z* = 429 also revealed the complete gas-phase ligand exchange and formation of $[Pd(hfac)_2]^+$ at *m/z* = 520. This is the first complete ligand exchange involving the Pd metal observed in this study and is presented below in Figure 4.19.

$$[Pd(tftm - CF_3)(tftm)]^+ + Ni(hfac)_2 \rightarrow$$

$$[Pd(hfac)(hfac)]^+ + Ni(tftm - CF_3)(tftm) \qquad \text{(Eqn 4.15)}$$

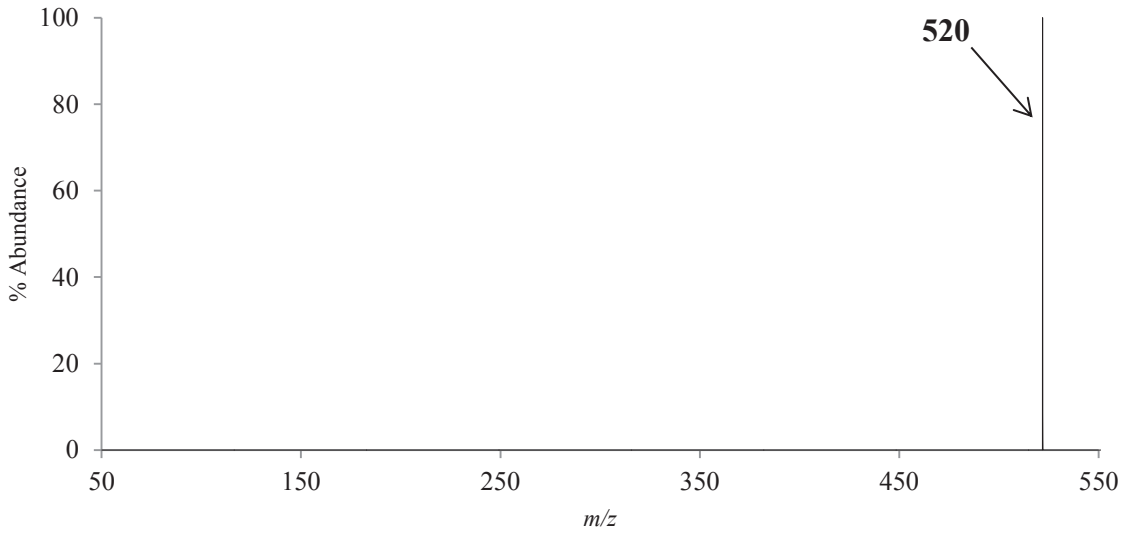

Figure 4.19: The positive mass spectrum obtained by scanning the third quadrupole after the selective reaction of *m/z* = 429 ($[Pd(tftm)(tftm - CF_3)]^+$) with neutral $Ni(hfac)_2$ to produce the complete gas-phase ligand exchange product of *m/z* = 520 ($[Pd(hfac)_2]^+$).

The mass selection of $[Pd(tftm)]^+$ at *m/z* = 300 showed a single gas-phase exchange product. The proposed mechanism for this reaction is found in Equation 4.16 with the spectrum featured in Figure 4.20 showing the mixed ligand formation of $[Pd(tftm)(hfac)]^+$ at *m/z* = 508.

$$[Pd(tftm)]^+ + Ni(hfac)_2 \rightarrow [Pd(tftm)(hfac)]^+ + Ni(hfac) \qquad \text{(Eqn 4.16)}$$

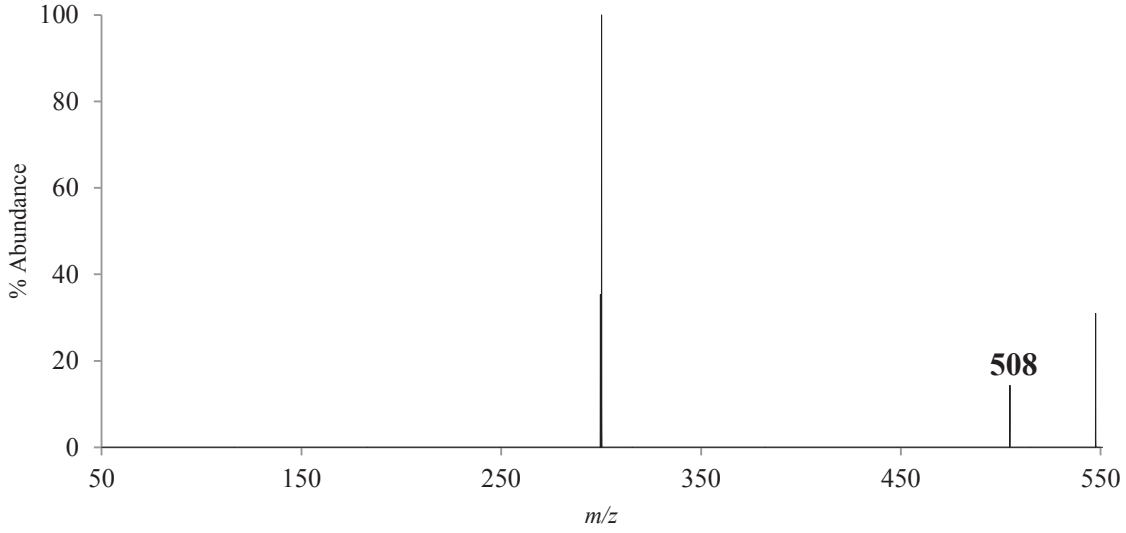

Figure 4.20: The positive mass spectrum obtained by scanning the third quardupole after the selective reaction of *m/z* = 300 ($[Pd(tftm)]^+$) with neutral $Ni(hfac)_2$ to produce the mixed ligand product of *m/z* = 508 ($[Pd(tftm)(hfac)]^+$).

The mass selection of $[Pd(tftm - tBu)]^+$ at *m/z* = 243 produced two different gas-phase ligand exchange products. The proposed mechanisms for these products can be found in Equations 4.17 and 4.18. The first selective reaction featured in Figure 4.21 is unique as it that actually exhibits an addition instead of a loss. This addition corresponds to $[Ni(tftm) + t\text{Bu}]^+$ located at *m/z* = 310. More extensive selective reaction research should be done in this area to understand how the addition of a functional group is happening in the gas-phase. This was also observed by Hunter et.al. with studies involving $Ni(hfac)_2$ gas-phase ligand exchanges.[17]

$$[Pd(tftm - t\text{Bu})]^+ + Ni(hfac)_2 + 2\ t\text{Bu} \rightarrow [Ni(tftm) + t\text{Bu})]^+ + Pd(hfac)_2 \qquad \text{(Eqn 4.17)}$$

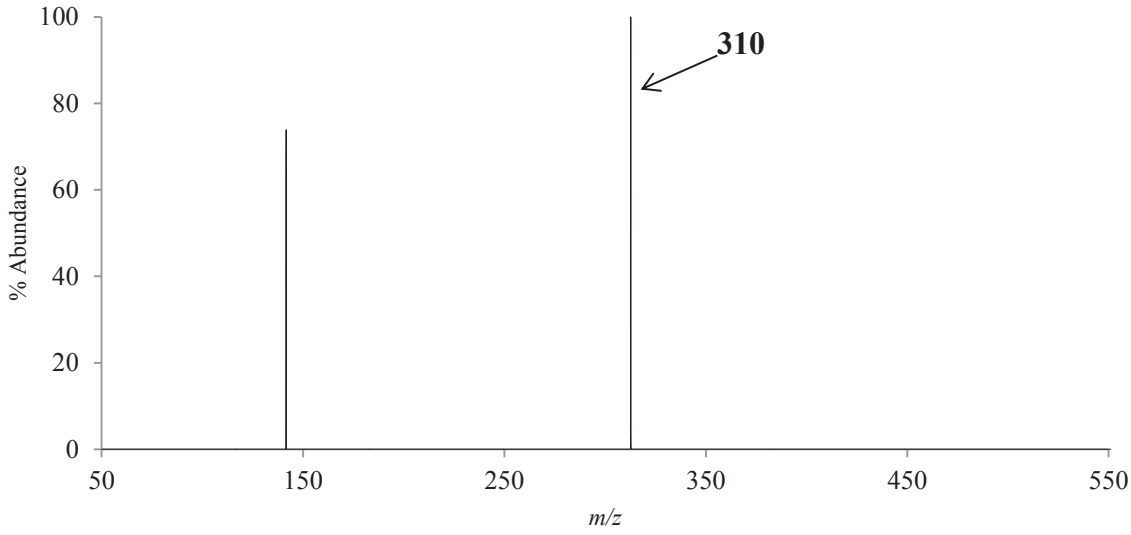

Figure 4.21: The positive mass spectrum obtained by scanning the third quadrupole after the selective reaction of *m/z* = 243 ($[Pd(tftm - t\text{Bu})]^+$) with neutral $Ni(hfac)_2$ to produce *m/z* = 310 ($[Ni(tftm + t\text{Bu})]^+$).

The selective reaction mass-selecting for *m/z* = 243 also produced an ion signal representative of the partial ligand exchange production of $[Ni(tftm)]^+$ at *m/z* = 253 observed in Figure 4.22.

$$[Pd(tftm - tBu)]^+ + Ni(hfac)_2 + tBu \rightarrow [Ni(tftm)]^+ + Pd(hfac)_2 \quad \text{(Eqn 4.18)}$$

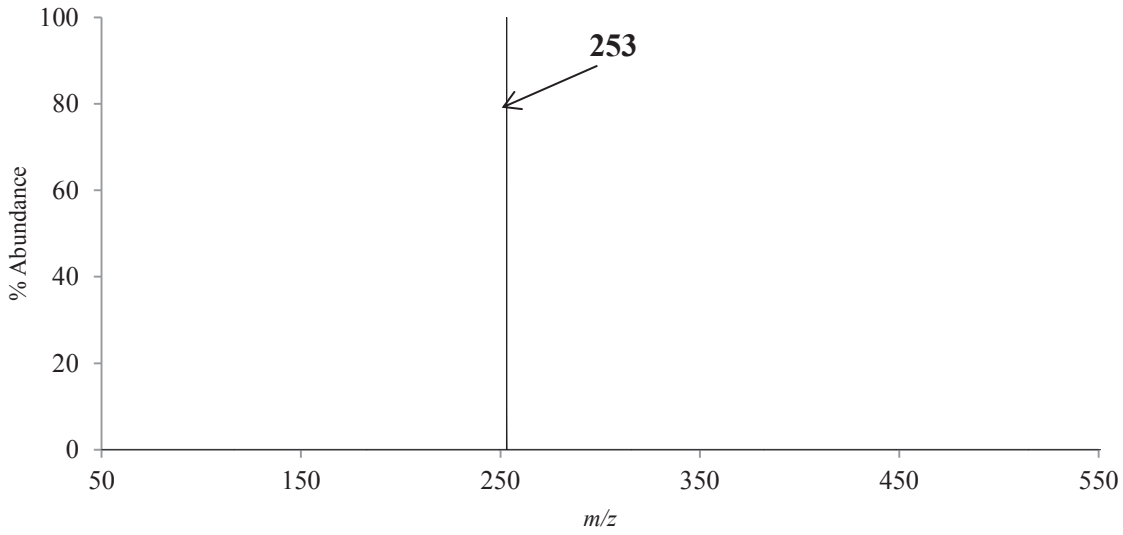

Figure 4.22: The positive mass spectrum obtained by scanning the third quadrupole after the selective reaction of *m/z* = 243 ($[Pd(tftm - tBu)]^+$) with neutral $Ni(hfac)_2$ to produce the partial gas-phase ligand exchange product of *m/z* = 253 ($[Ni(tftm)]^+$).

The mass selection of $[Pd(tftm - CF_3)]^+$ at *m/z* = 231 revealed one appreciable mass spectrum. The proposed mechanism for the reaction is found in Equation 4.19 with the corresponding mass spectrum featured in Figure 4.23. The complete ligand exchange product of $[Ni(tftm)_2]^+$ is observed at *m/z* = 448. Again, similar to Equations 4.9, 4.12, and 4.14, this mechanism needs to be investigated further.

$$[Pd(tftm - CF_3)]^+ + Ni(hfac)_2 + CF_3 \rightarrow [Ni(tftm)(tftm)]^+ + Pd(hfac) \qquad \text{(Eqn 4.19)}$$

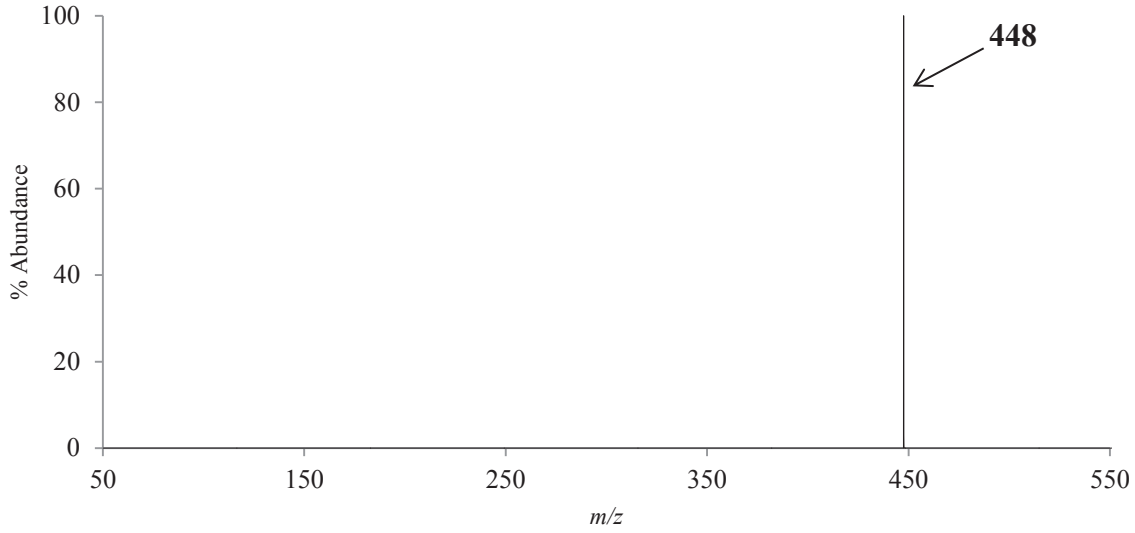

Figure 4.23: The positive mass spectrum obtained by scanning the third quadrupole after the selective reaction of *m/z* = 231 ($[Pd(tftm - CF_3)]^+$) with neutral $Ni(hfac)_2$ to produce the complete gas-phase ligand exchange product of *m/z* = 448 ($[Ni(tftm)_2]^+$).

The results of these selective reactions have provided insight into which palladium-containing β-diketonates fragments may play a role in the gas-phase ligand exchange reactions occurring with neutral $Ni(hfac)_2$. The selective reaction of $[Pd(tftm)(tftm - CF_3)]^+$ at *m/z* = 429, produced two appreciable mass spectra. The first spectrum in Figure 4.18 exhibits complete gas-phase ligand exchange evident from the ion signal corresponding to $[Ni(tftm)_2]^+$ at *m/z* = 448 while the second spectrum in Figure 4.19 shows opposite complete ligand exchange formation of $[Pd(hfac)_2]^+$ at m/z = 520. The ability of *m/z* = 429 to produce evidence for two different complete gas-phase ligand exchange products makes it a key player in the exchange process.

The fragment $[Pd(tftm)]^+$ at *m/z* = 300 may also play a role in ligand exchange as it shows the mixed ligand formation of $[Pd(tftm)(hfac)]^+$ in Figure 4.20. The fragment of $[Pd(tftm - tBu)]^+$ at *m/z* = 243 also plays a role in gas-phase ligand exchange as it shows both the unique formation of $[Ni(tftm) + tBu]^+$ in the gas-phase observed in Figure 4.21 as well as the partial ligand exchange product of $[Ni(tftm)]^+$ at *m/z* = 253 observed in Figure 4.22. The mass selection of $[Pd(tftm - CF_3)]^+$ at *m/z* = 231 could also play a role in the gas-phase ligand exchange between $Pd(tftm)_2$ and $Ni(hfac)_2$ as it produces the complete ligand exchange product of $[Ni(tftm)_2]^+$ at *m/z* = 448 presented in Figure 4.23. The mass selection of *m/z* = 498 and *m/z* = 439 did not produce appreciable data and is thus not thought to play a major role in the gas-phase ligand exchange of $Pd(tftm)_2$ and $Ni(hfac)_2$.

4.2.11 Nickel Trifluoroacetylacetonate ($Ni(tfac)_2$)

Nickel trifluoroacetylacetonate ($Ni(tfac)_2$) is a novel metal β-diketonate complex that is reported herein for the first time. $Ni(tfac)_2$ was investigated using co-sublimation reactions as well as selective reactions within the collision cell in order to gain more insight into the properties and characteristics of this particular complex.

Figure 4.24 is a representative positive mass spectrum of $Ni(tfac)_2$ and is presented for the first time with as mass range of *m/z* = 100 - 500, the same shortened range used earlier for other species. This mass spectrum is also presented in the vertically stacked co-sublimation spectra found in Figure 4.25 (a) with a mass range of *m/z* = 50 – 550 for comparative purposes. The shortened mass range again illustrates the characteristics of this complex by minimizing the abundance of the *m/z* = 57 ion signal peak that overwhelms the data given its relatively high intensity. The peak at *m/z* = 364 in Figure 4.24 is the dominant parent peak $[Ni(tfac)_2]^+$, while the peak at *m/z* = 349 comes from the loss of a methyl group from one of the ligands attached to the nickel center. At *m/z* = 295, the loss of a CF_3 group is observed and the peak at *m/z* = 211 corresponds to the loss of an entire ligand ($[Ni(tfac)]^+$), and *m/z* = 142 is the subsequent loss of the remaining CF_3 group. Also as with $Pd(tftm)_2$, the relative abundance of the fragmentation of $Ni(tfac)_2$ shown in Table 4.6 was based upon *m/z* = 364 as the base peak since it is the most abundant peak of importance.

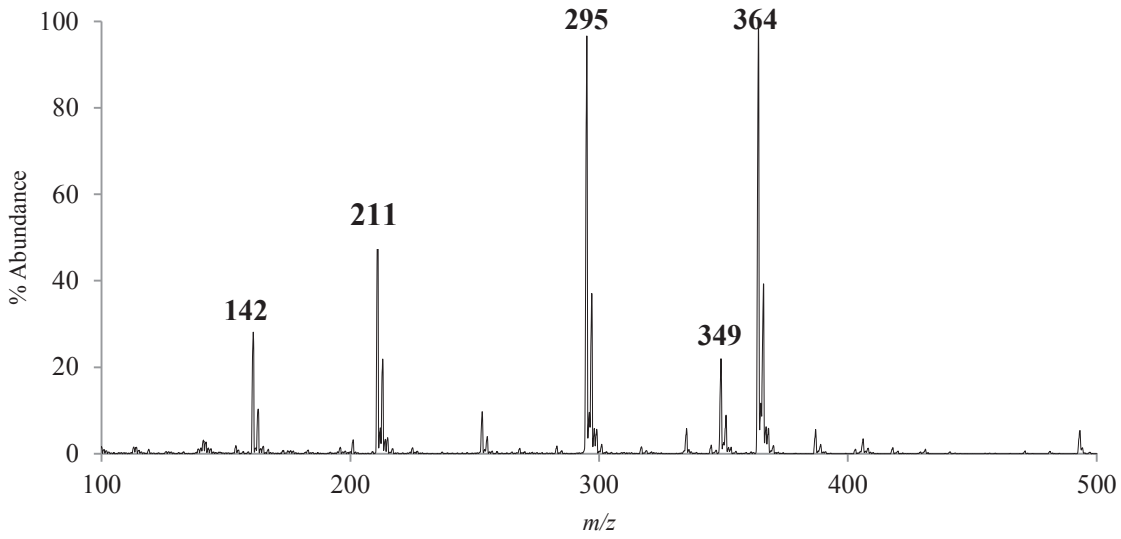

Figure 4.24: The 70 eV positive EI mass spectrum of $Ni(tfac)_2$, showing only the range between m/z = 100 and m/z = 500 to exhibit more isotopic abundance without the interference of the background m/z = 57 peak corresponding to the loss of a *t*Bu group.

Species	*m/z*	Relative Abundance
$[Ni(tfac)_2]^+$	364	100
$[Ni(tfac)(tfac - CH_3)]^+$	349	22
$[Ni(tfac)(tfac - CF_3)]^+$	295	97
$[Ni(tfac)]^+$	211	54
$[Ni(tfac - CF_3)]^+$	142	4

Table 4.6: The fragmentation species and corresponding relative abundances of the mass spectral analysis of $Ni(tfac)_2$ as presented in Figure 4.24.

4.2.12 Co-Sublimation of $Pd(tftm)_2$ & $Ni(tfac)_2$

The mass spectrum presented in Figure 4.25 is vertically stacked to better visualize the extent of ligand exchange occurring. The top portion, Figure 4.25 (a), features the single $Ni(tfac)_2$ spectrum showing typical fragmentation patterns such as the dominant parent peak at *m/z* = 364 and the peak representing the loss of a CH_3 group at *m/z* = 349. The loss of a CF_3 group at *m/z* = 295, the peak at *m/z* = 211 representing the loss of an entire trifluoroacetylacetonate ligand ($[Ni(tfac)]^+$, and finally the subsequent loss of a CF_3 group at *m/z* = 142 are also observed as mentioned earlier. The middle portion, Figure 4.25 (b), shows the spectrum of $Pd(tftm)_2$ which resembles Figure 4.1,

but over a different mass range. The bottom portion, Figure 4.25 (c), corresponds to the spectrum of the co-sublimation of both $Pd(tftm)_2$ and $Ni(tfac)_2$.

It is important to note that there are peaks present in the co-sublimation spectrum that are not featured in the previous single spectra. Those species that underwent any amount of ligand exchange, which includes partial exchanges, mixed ligand formations, and complete exchanges are labeled within the spectra and highlighted in bold. The *m/z* values and the relative abundances of the single species, exchange products, as well as the co-sublimation species are featured below in Table 4.7. The relative abundances were calculated in relation to the most intense peak of importance, that is, the peak with the most intensity that is either a partial exchange, mixed ligand, or full exchange product. In Figure 4.25 (c), *m/z* = 211 was selected as the base peak for the relative abundance calculations since it was the most intense peak of importance and corresponds to $[Ni(tfac)]^+$. Results from this co-sublimation show partial, mixed, and full ligand exchange for both the nickel and the palladium species, however the nickel appears to have a greater success in performing the complete exchange of ligands, similar to the results in Section 4.2.3, 4.2.5, and 4.2.7. The relative abundances of the single reactions as well as the co-sublimation reactions can be found below in Table 4.7. The italicized rows correspond to isobaric peaks in the co-sublimation spectrum.

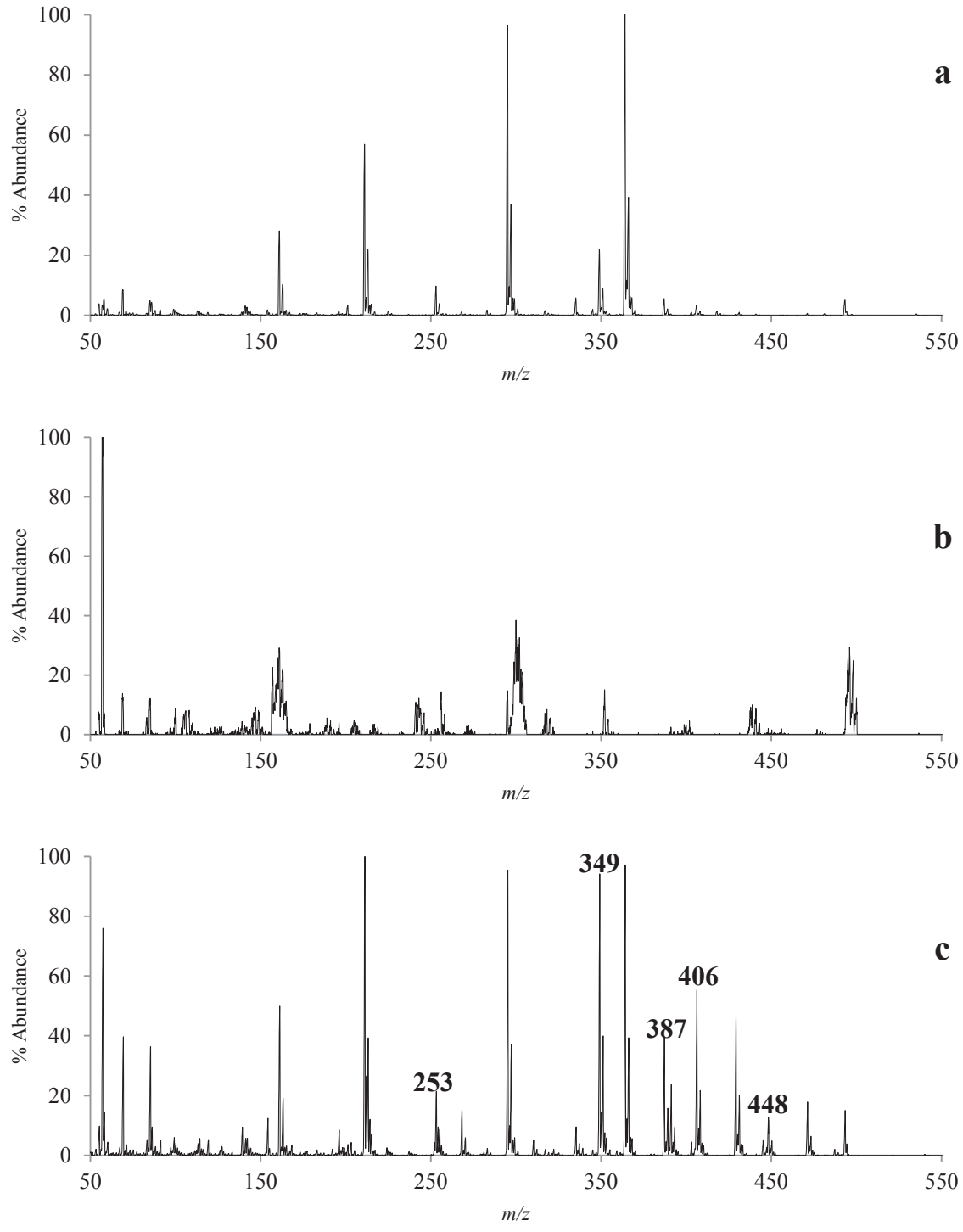

Figure 4.25: The 70 eV positive EI mass spectra of (a) $Ni(tfac)_2$, (b) $Pd(tftm)_2$, and (c) the co-sublimation of $Pd(tftm)_2$ and $Ni(tfac)_2$. Mixed ligand or ligand exchange peaks are highlighted in bold.

An important thing to note is that this co-sublimation reaction shows appreciable isobaric abundance. For example, *m/z* = 349 corresponds to both $[Ni(tfac)(tfac - CH_3)]^+$ as well as $Ni[(tftm - tBu)(tfac)]^+$. Similarly, *m/z* = 196 corresponds to both $[Ni(tfac - CH_3)]^+$ as well as $[Pd(tftm - tBu)]^+$. The isobaric species observed in this co-sublimation reaction are highlighted in red in Table 4.7. These interferences may make the proposition of mechanisms for these gas-phase ligand exchanges more difficult to produce.

	Mass	**Mass**	**NiL^*_2**	**PdL'_2**	**NiL^*_2 & PdL'_2**	**NiL^*_2 & PdL'_2**
Species	Ni	Pd	Ni	Pd	Ni	Pd
ML^*_2	364	414	100		92	<1
ML^*_2-CF_3	295	345	97		92	2
ML^*_2 - CH_3	*349*	*399*	*22*		*89*	*0*
ML*	211	260	54		100	<1
ML* - CF_3	142	191	3		6	<1
ML* - CH_3	*196*	*243*	*2*		*8*	*<1*
ML'_2	448	496		65	13	4
ML'_2-*t*Bu	391	439		20	23	<1
ML'_2-CF_3	379	429		<1	<1	45
ML'	253	300		100	21	6
ML'-tBu	*196*	*243*		*31*	*8*	*<1*
ML'-CF_3	184	231		<1	2	<1
ML'L*	406	455			52	<1
M(L'- tBu)L*	*349*	*399*			*89*	*0*
M(L'-CF_3)L*	335	387			10	37

Table 4.7: The mass spectrometric relative abundances of nickel and palladium β-diketonate complexes as well as the co-sublimation products as presented in Figure 4.25.

4.2.13 Selective Reactions of $Pd(tftm)_2$ & $Ni(tfac)_2$

The selective reactions featured in this section were conducted in the same way as stated in Sections 4.2.4, 4.2.7, and 4.2.10. The spectra included below in Figures 4.26 – 4.36 show the results of these reactions following the proposed mechanisms of these reactions The collision chamber was purged with the gaseous $Ni(tfac)_2$ prior to each run. The selective reaction for $Ni(tfac)_2$ showed many more products than the previous selective reactions. This reaction combination may prove to be the most promising for pursuit by future researchers.

The mass selection of $[Pd(tftm)_2]^+$ at *m/z* = 498 produced three gas-phase ligand exchange products as seen below in Figures 4.26, 4.27, and 4.28. First, in Figure 4.26, the mixed ligand formation of $[Ni(tftm)(tfac)]^+$ is observed at *m/z* = 406. This is presented following the proposed mechanism in Equation 4.20.

$$[Pd(tftm)(tftm)]^+ + Ni(tfac)_2 \rightarrow [Ni(tftm)(tfac)]^+ + Ni(tfac)(tftm) \qquad \text{(Eqn 4.20)}$$

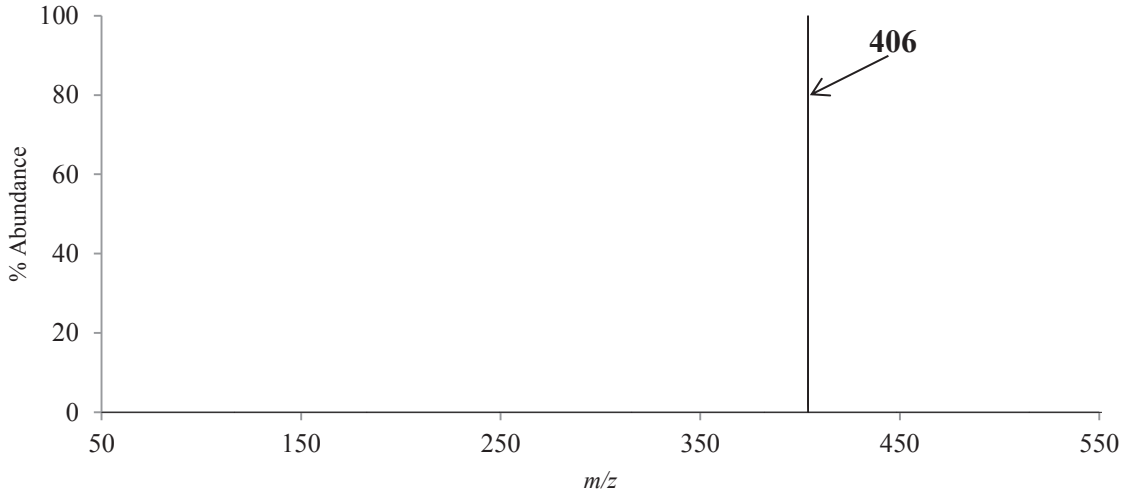

Figure 4.26: The positive mass spectrum obtained by scanning the third quadrupole after the selective reaction of *m/z* = 498 ($[Pd(tftm)_2]^+$) with neutral $Ni(tfac)_2$ to produce the mixed ligand *m/z* = 406 ($[Ni(tftm)(tfac)]^+$).

In addition to the mixed ligand formation from the mass-selection of m/z = 498, Figure 4.27 shows evidence for the partial exchange of $[Ni(tftm)]^+$ observed at *m/z* = 253. The proposed mechanism for this reaction is found in Equation 4.21.

$$[Pd(tftm)(tftm)]^+ + Ni(tfac)_2 \rightarrow [Ni(tftm)]^+ + Pd(tfac)_2 + (tftm) \qquad \text{(Eqn 4.21)}$$

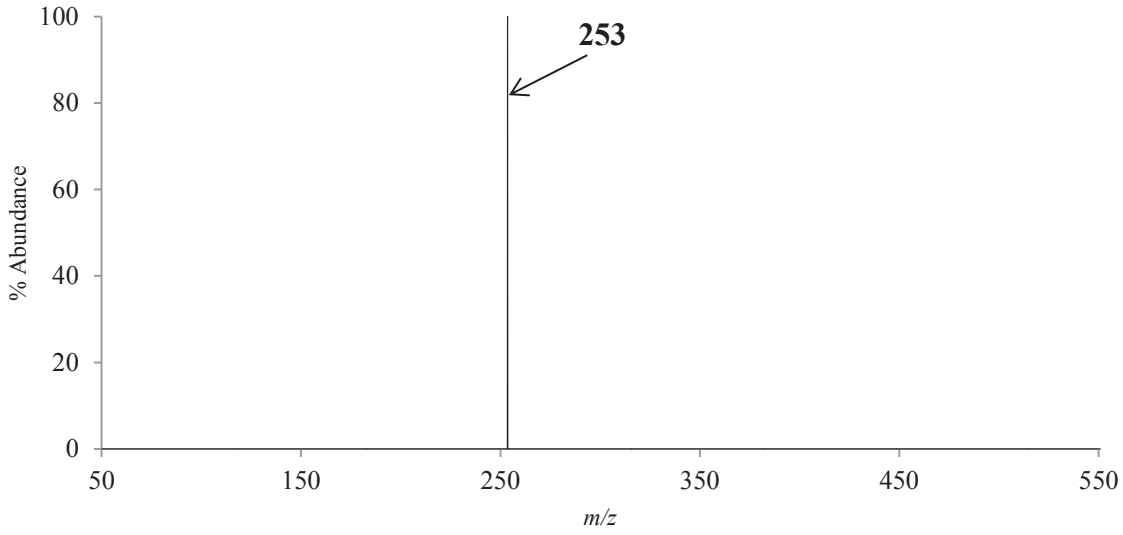

Figure 4.27: The mass spectrum obtained by scanning the third quardupole after the selective reaction of *m/z* = 498 ($[Pd(tftm)_2]^+$) with neutral $Ni(tfac)_2$ to produce the partial gas-phase ligand exchange product of *m/z* = 253 ($[Ni(tftm)]^+$).

As presented in Figure 4.28, the mass selection of $[Pd(tftm)_2]^+$ at *m/z* = 498 also produced another mixed ligand product corresponding to $[Ni(tftm - tBu)(tfac)]^+$ at *m/z* = 349. The proposed mechanism for this reaction is found below in Equation 4.22.

$$[Pd(tftm)(tftm)]^+ + Ni(tfac)_2 \rightarrow$$

$$[Ni(tftm - tBu)(tfac)]^+ + Pd(tftm)(tfac) + tBu \qquad \text{(Eqn 4.22)}$$

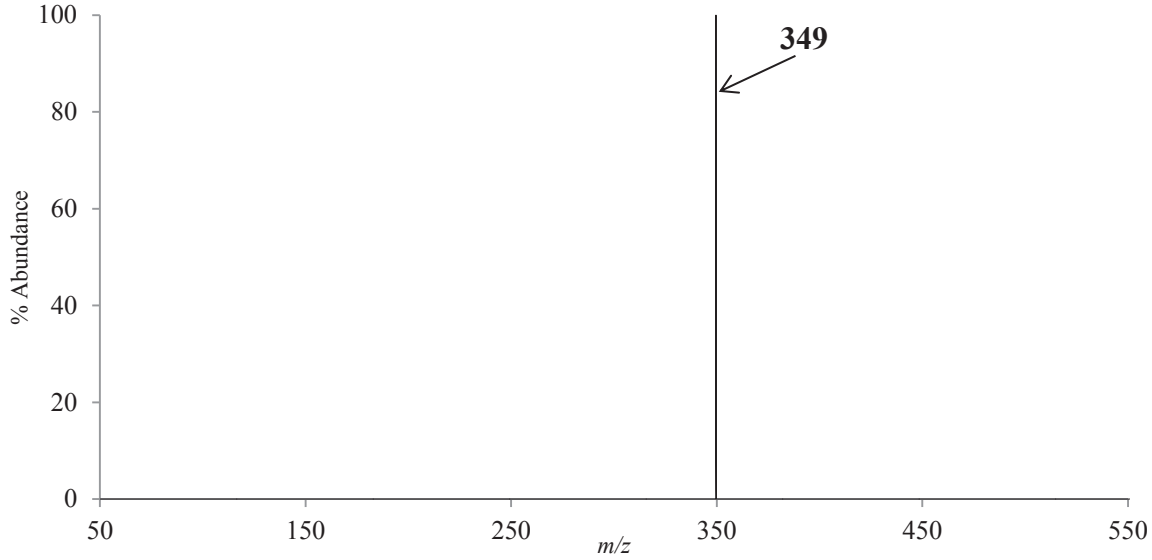

Figure 4.28: The positive mass spectrum obtained by scanning the third quadrupole after the selective reaction of *m/z* = 498 ($[Pd(tftm)_2]^+$) with neutral $Ni(tfac)_2$ to produce the mixed ligand *m/z* = 349 ($[Ni(tftm - tBu)(tfac)]^+$).

The mass selection of ([Pd(tftm)(tftm – *t*Bu)]$^+$ at *m/z* = 439 produced one gas-phase ligand exchange product at *m/z* = 349. This peak corresponds to the mixed ligand formation of [Ni(tftm – *t*Bu)(tfac)]$^+$. The proposed reaction mechanism is found in Equation 4.23 and the corresponding spectrum is presented in Figure 4.29.

$$[Pd(tftm - tBu)(tftm)]^+ + Ni(tfac)_2 \rightarrow$$

$$[Ni(tftm - tBu)(tfac)]^+ + Pd(tftm)(tfac) \qquad \text{(Eqn 4.23)}$$

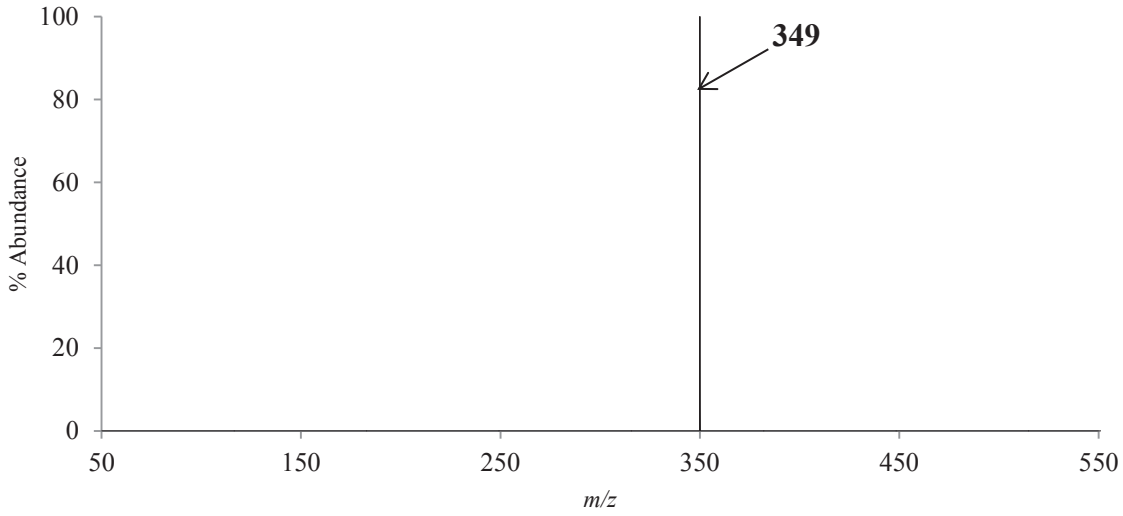

Figure 4.29: The positive mass spectrum obtained by scanning the third quadrupole after the selective reaction of *m/z* = 439 ([Pd(tftm)(tftm – *t*Bu)]$^+$) with neutral Ni(tfac)$_2$ to produce the mixed ligand *m/z* = 349 ([Ni(tftm – *t*Bu)(tfac)]$^+$).

The mass selection of $[Pd(tftm)(tftm - CF_3)]^+$ at *m/z* = 429 also produced only one ligand exchange product. The proposed mechanism of this reaction can be found in Equation 4.24 and the spectrum is presented in Figure 4.30. The peak at *m/z* = 253 corresponds to the partial exchange product of $[Ni(tftm)]^+$.

$$[Pd(tftm - CF_3)(tftm)]^+ + Ni(tfac)_2 \rightarrow$$
$$[Ni(tftm)]^+ + Pd(tfac)(tftm - CF_3) + (tfac) \qquad \text{(Eqn 4.24)}$$

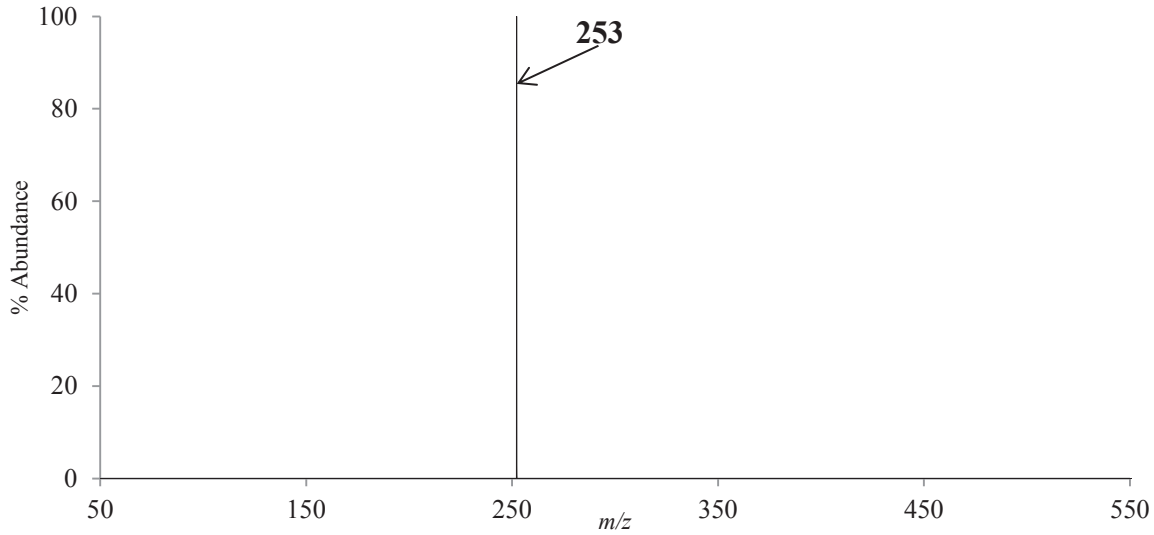

Figure 4.30: The positive mass spectrum obtained by scanning the third quadrupole after the selective reaction of *m/z* = 429 ($[Pd(tftm)(tftm - CF_3)]^+$) with neutral $Ni(tfac)_2$ to produce the partial ligand exchange product of *m/z* = 253 ($[Ni(tftm)]^+$).

The mass selection of $[Pd(tftm)]^+$ at *m/z* = 300 produced the three spectra observed below in Figures 4.31, 4.32, and 4.33. Each of these mass spectra show mixed ligand formations with proposed mechanisms for each presented in Equations 4.25, 4.26, and 4.27. Figure 4.31 below shows the mixed ligand formation of $[Ni(tftm)(tfac)]^+$ representing the peak at *m/z* = 406.

$$[Pd(tftm)]^+ + Ni(tfac)_2 \rightarrow [Ni(tftm)(tfac)]^+ + Ni(tfac) \qquad \text{(Eqn 4.25)}$$

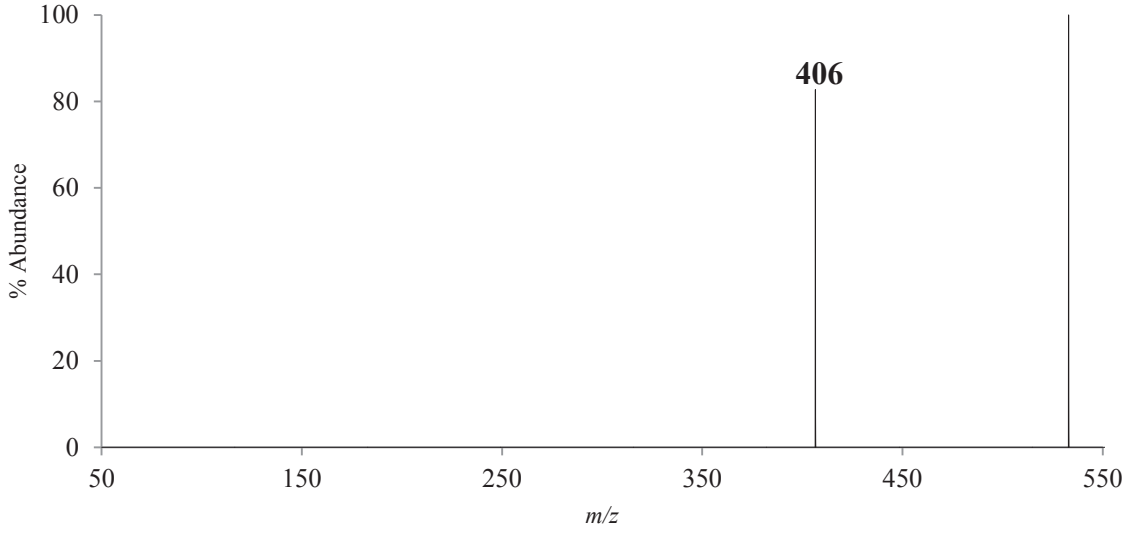

Figure 4.31:The positive mass spectrum obtained by scanning the third quadrupole after the selective reaction of *m/z* = 300 ($[Pd(tftm)]^+$) with neutral $Ni(tfac)_2$ to produce the mixed ligand *m/z* = 406 ($[Ni(tftm)(tfac)]^+$).

The mass selection of $[Pd(tftm)]^+$ at *m/z* = 300 also produced a mixed ligand fragment. The proposed mechanism for this reaction is found in Equation 4.26 and the spectra is presented below in Figure 4.32, where *m/z* = 349, representing [Ni(tftm – *t*Bu)(tfac)]$^+$ is detected.

$$[Pd(tftm)]^+ + Ni(tfac)_2 \rightarrow [Ni(tftm - tBu)(tfac)]^+ + Pd(tfac) \qquad \text{(Eqn 4.26)}$$

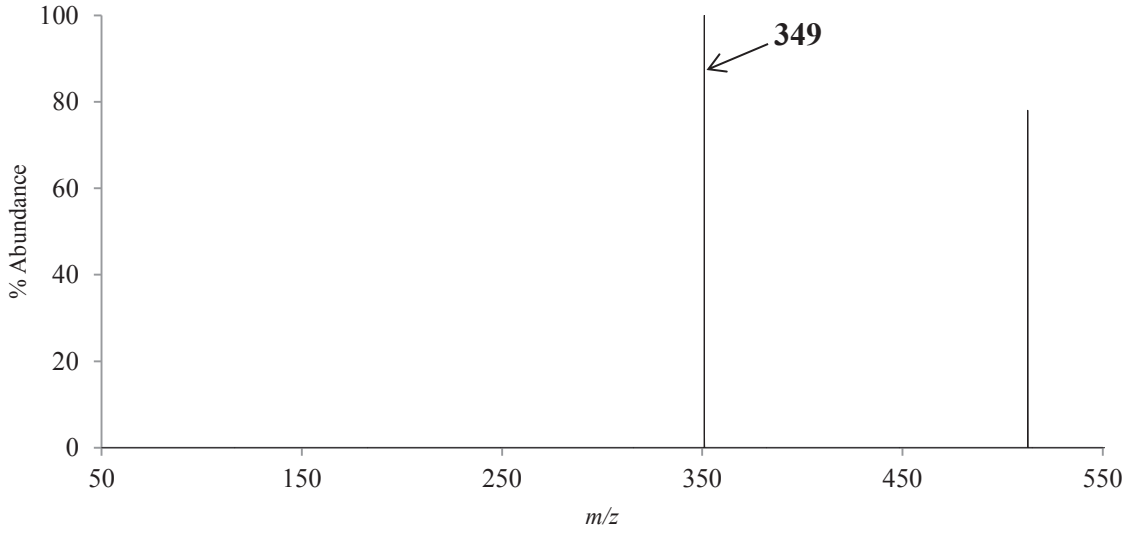

Figure 4.32:The positive mass spectrum obtained by scanning the third quadrupole after the selective reaction of *m/z* = 300 ($[Pd(tftm)]^+$) with neutral $Ni(tfac)_2$ to produce the mixed ligand fragment of *m/z* = 349 ([Ni(tftm – *t*Bu)(tfac)]$^+$).

The mass-selection of *m/z* = 300 also revealed the Pd-containing mixed ligand fragment $[Pd(tftm - tBu)(tfac)]^+$. The proposed mechanism for this reaction is found in Equation 4.27 and the spectrum featuring the corresponding ion signal at *m/z* = 387 is found below in Figure 4.33.

$$[Pd(tftm)]^+ + Ni(tfac)_2 \rightarrow [Pd(tftm - tBu)(tfac)]^+ + Ni(tfac) + tBu \qquad \text{(Eqn 4.27)}$$

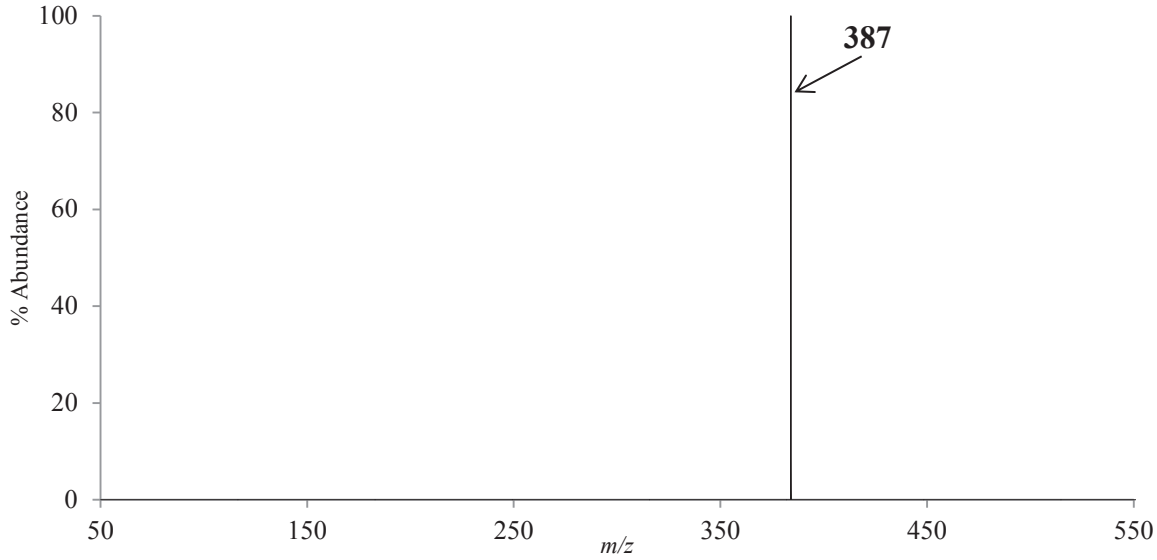

Figure 4.33:The positive mass spectrum obtained by scanning the third quadrupole after the selective reaction of *m/z* = 300 ($[Pd(tftm)]^+$) with neutral $Ni(tfac)_2$ to produce the mixed ligand fragment *m/z* = 387 ($[Pd(tftm - tBu)(tfac)]^+$).

The mass selection of $[Pd(tftm - tBu)]^+$ at *m/z* = 243 is probably one of the most interesting sets of selective reactions featured in this study. This mass selection produced the four different gas-phase exchange products presented in Figures 4.34 and 4.35, The proposed mechanisms are also featured in Equations 4.28, 4.29, 4.30, and 4.31. First, the complete gas-phase ligand exchange product of $[Ni(tftm)_2]^+$ is represented by the peak located at *m/z* = 448 in Figure 4.34 below. Similar to previous mechanisms, the one featured in Equation 4.28 will need to be further investigated for validity.

$$[Pd(tftm - tBu)]^+ + Ni(tfac)_2 + (tftm) + tBu \rightarrow$$
$$[Ni(tftm)(tftm)]^+ + Pd(tfac)_2 \qquad \text{(Eqn 4.28)}$$

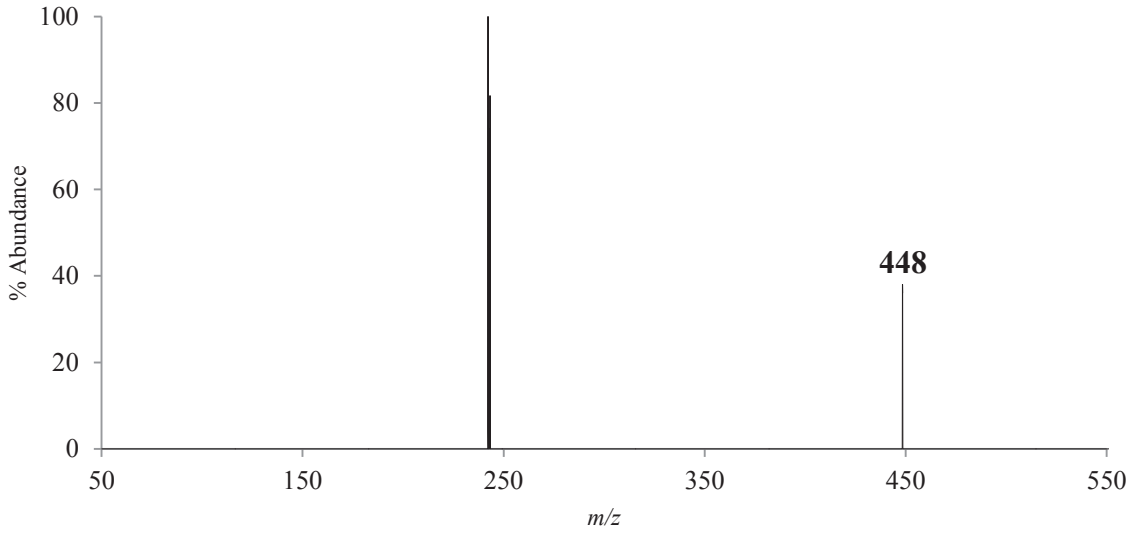

Figure 4.34: The positive mass spectrum obtained by scanning the third quadrupole after the selective reaction of *m/z* = 243 ($[Pd(tftm - tBu)]^+$) with neutral $Ni(tfac)_2$ to produce the complete gas-phase ligand exchange product of *m/z* = 448 ($[Ni(tftm)_2]^+$).

The next spectrum observed in Figure 4.35 is even more interesting because it shows the production of not one, but three gas-phase ligand exchange products in a single spectrum. The first product is $[Ni(tftm - tBu)(tfac)]^+$ observed at *m/z* = 349. Next, the mixed ligand formation of $[Pd(tftm - tBu)(tfac)]^+$ is represented at *m/z* = 387. Finally the mixed ligand formation of $[Ni(tftm)(tfac)]^+$ is represented at *m/z* = 406.

$$[Pd(tftm - tBu)]^+ + Ni(tfac)_2 \rightarrow [Ni(tftm - tBu)(tfac)]^+ + Pd(tfac) \quad \text{(Eqn 4.29)}$$

$$[Pd(tftm - tBu)]^+ + Ni(tfac)_2 \rightarrow [Pd(tftm - tBu)(tfac)]^+ + Ni(tfac) \quad \text{(Eqn 4.30)}$$

$$[Pd(tftm - tBu)]^+ + Ni(tfac)_2 + tBu \rightarrow [Ni(tftm)(tfac)]^+ + Ni(tfac) \quad \text{(Eqn 4.31)}$$

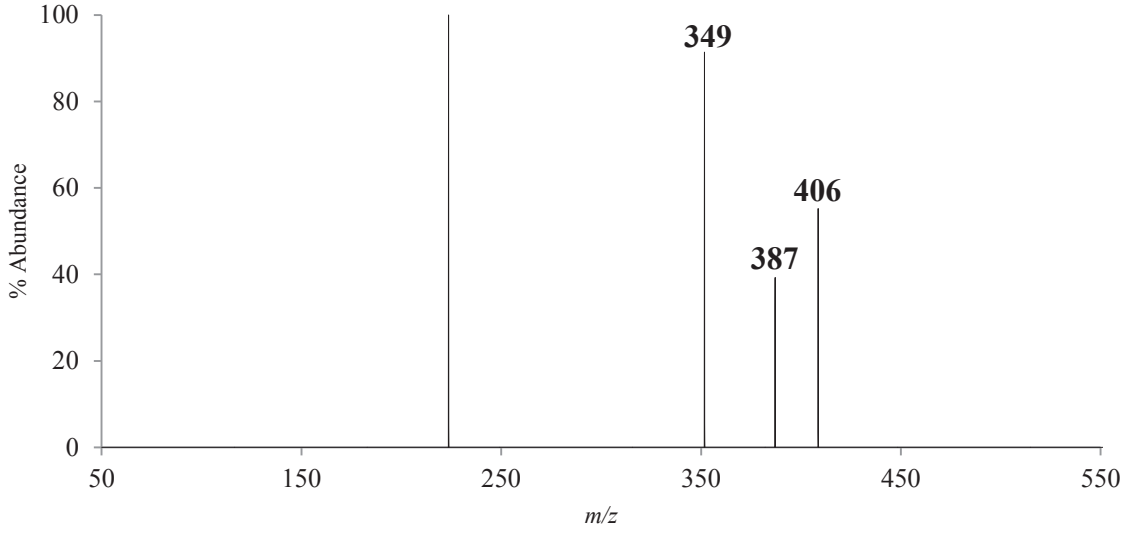

Figure 4.35: The positive mass spectrum obtained by scanning the third quadrupole after the selective reaction of *m/z* = 243 ($[Pd(tftm - tBu)]^+$) with neutral $Ni(tfac)_2$ to produce the mixed ligand products of *m/z* = 349 ($[Ni(tftm - tBu)(tfac)]^+$), *m/z* = 387 ($[Pd(tftm - tBu)(tfac)]^+$), and *m/z* = 406 ($[Ni(tftm)(tfac)]^+$).

The mass selection of $[Pd(tftm - CF_3)]^+$ at *m/z* = 231 also produced an appreciable spectrum found in Figure 4.36. A proposed mechanism for the partial exchange product of $[Ni(tftm)]^+$ at *m/z* = 253 is presented in Equation 4.32. This mechanism also needs further investigation due to the necessity of other species necessary to produce the intact *tftm*.

$$[Pd(tftm - CF_3)]^+ + Ni(tfac)_2 + CF_3 \rightarrow [Ni(tftm)]^+ + Pd(tfac)_2 \qquad \text{(Eqn 4.32)}$$

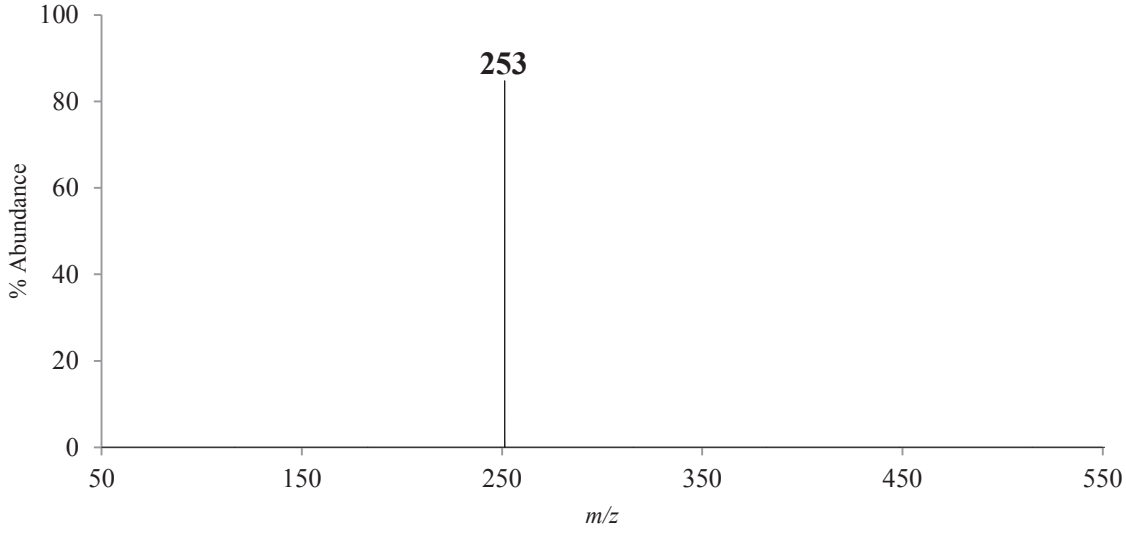

Figure 4.36: The positive mass spectrum obtained by scanning the third quadrupole after the selective reaction of *m/z* = 231 ($[Pd(tftm - CF_3)]^+$) with neutral $Ni(tfac)_2$ to produce *m/z* = 253 ($[Ni(tftm)]^+$).

The results of the selective reactions involving neutral $Ni(tfac)_2$ have shown the most evidence of gas-phase ligand exchange among all of the β-diketonate complexes studied. The selective reaction of $[Pd(tftm)_2]^+$ at *m/z* = 498 appears to be an active participant in the gas-phase ligand exchange of the selective reactions observed in Figures 4.26, 4.27, and 4.28. The ligand exchange products associated with these Figures show the production of $[Ni(tftm)(tfac)]^+$ at *m/z* = 406, $[Ni(tftm)]^+$ at *m/z* = 253, and $[Ni(tftm - tBu)(tfac)]^+$ at *m/z* = 349, respectively.

The selective reaction of $[Pd(tftm - tBu)(tftm)]^+$ at *m/z* = 439 with neutral $Ni(tfac)_2$ also provides evidence for the gas-phase ligand exchange of $Pd(tftm)_2$ with $Ni(tfac)_2$. The results of this selective reaction is found in Figure 4.29 and show the production of $[Ni(tftm - tBu)(tfac)]^+$ at *m/z* = 349. The selective reaction of $[Pd(tftm)(tftm - CF_3)]^+$ at *m/z* = 429 produced one appreciable mass spectrum observed in Figure 4.30 showing evidence for the partial ligand exchange production of $[Ni(tftm)]^+$ at *m/z* = 253.

The fragment $[Pd(tftm)]^+$ at *m/z* = 300 may also play a more major role in ligand exchange as it shows the production of three different ligand exchange products featured in Figures 4.31, 4.32, and 4.33. These Figures show evidence for the mixed ligand production of $[Ni(tftm)(tfac)]^+$ at *m/z* = 406, $[Ni(tftm - tBu)(tfac)]^+$ at *m/z* = 349, and $[Pd(tftm - tBu)(tfac)]^+$ at *m/z* = 387, respectively.

The selective reaction of $[Pd(tftm - tBu)]^+$ at *m/z* = 243 appear to the most influential fragment in the gas-phase ligand exchange with $Ni(tfac)_2$. Figure 4.34 shows the complete ligand exchange product of $[Ni(tftm)_2]^+$ at *m/z* = 448. Figure 4.35 is unique

in that it contains three ligand exchange products, including $[Ni(tftm - tBu)(tfac)]^+$ at *m/z* = 349, $[Pd(tftm - tBu)(tfac)]^+$ at *m/z* = 387, and $[Ni(tftm)(tfac)]^+$ at *m/z* = 406. The presence of so many different mixed ligands within these spectra provides clear indication that $[Pd(tftm - tBu)]^+$ plays an important role in these selective reactions and may be responsible for the production of the mixed ligand products during co-sublimation.

The mass selection of $[Pd(tftm - CF_3)]^+$ at *m/z* = 231 could also be an active participant in the gas-phase ligand exchange between $Pd(tftm)_2$ and $Ni(tfac)_2$ as it produces the partial ligand exchange product of $[Ni(tftm)]^+$ at *m/z* = 253 observed in Figure 4.36. This is the only set of selective reactions in this study that shows that all six mass-selected fragments provide evidence of playing a role in gas-phase ligand exchange.

Chapter 5: The Co-sublimation of Palladium trifluorotrimethylacetylacetonate with Copper and Zinc Metal β-Diketonate Complexes

5.1 Introduction

This chapter examines the gas-phase co-sublimation of $Pd(tftm)_2$ with several copper and zinc metal β-diketonate compounds ($Cu(acac)_2$, $Cu(eeac)_2$, $Cu(hfac)_2$, and $Zn(hfac)_2$). The reactions presented herein do not include the nickel compounds presented in Chapter 4. Though this data does not include proposed mechanisms and collision cell data, ligand exchange does occur and sheds light on the propensity of these complexes to react in the gas-phase.

The research presented in this Chapter is exciting as it shows partial exchanges, mixed ligand exchanges, and even a few complete exchanges in the gas phase. The spectra and tables of relative intensity presented in this Chapter show the propensity for certain compounds to undergo mixed ligand exchange. Perhaps one of the most important features of this Chapter is that all spectra presented here support Hunter's previous claims that the pathways for mixed ligand formation are not reactant dependent.[17] That is, it is predicted that no matter what metal β-diketonate sample is being co-sublimed with the $Pd(tftm)_2$ complex, a mixed ligand of some recognizable intensity is forming.

5.2 Results and Discussion

5.2.1 Co-sublimation of $Pd(tftm)_2$ & $Cu(acac)_2$

The mass spectra presented in Figure 5.1 are vertically stacked in order to better visualize the extent of ligand exchange occuring. This co-sublimation, as well as the ones following in Sections 5.2.2 – 5.2.4, was set up using the same experimental practice that was used in Chapter 4, Sections 4.2.3, 4.2.5, 4.2.7, and 4.2.9. The top portion, Figure 5.1 (a), features the single $Cu(acac)_2$ spectrum showing typical fragmentation patterns such as the parent peak at *m/z* = 261 , the loss of a methyl group at *m/z* = 246, the loss of another methyl group at *m/z* = 231, and finally the loss of an entire *acac* ligand at *m/z* = 161. The middle portion, Figure 5.1 (b), shows the spectrum of $Pd(tftm)_2$, which resembles Figure 4.1 but over a different mass range. The bottom portion, Figure 5.1 (c), corresponds to the mass spectrum of the co-sublimation of $Pd(tftm)_2$ and $Cu(acac)_2$ using a two-looped filament.

It is important to note that there are peaks present in the co-sublimation spectrum that are not featured in the previous single spectra which is a clear indication of gas-phase ligand exchange. Those species that underwent any amount of gas-phase ligand exchange, which includes both partial and complete exchange are labeled within the spectra and highlighted in bold. The *m/z* values for the fragmentation of the single species, the co-sublimation species, as well as the exchange products are featured below in Table 5.1. The relative abundances were calculated in relation to the most intense peak of importance, that is, the peak with the most intensity that is either a partial exchange, mixed ligand, or full exchange product. For example, in Figure 5.1 (c), the most intense peak is *m/z* = 57, however, *m/z* = 300 was selected as the base peak for the

relative abundance calculations since it was the most intense peak of importance corresponding to $[Pd(tftm)]^+$. Results from this co-sublimation experiment show partial, mixed, and full ligand exchange for both the copper and the palladium species, however the copper appears to have a greater success in performing the complete exchange of ligands.

The mixed ligand species tend to have a higher relative intensity than the products showing full ligand exchange. Additional research would need to be done to reveal a mechanism to which these mixed ligands form in the gas phase. It is also important to note some of the isobaric species in this spectrum, meaning two different species overlap in the same cluster of peaks. For example, the peak at *m/z* = 300 corresponds to both $[Pd(tftm)]^+$ and $[Cu(tftm\text{-}CF_3)(acac)]^+$. This conclusion comes from the comparison of the single sublimation spectra seen in Figure 5.1 (a) and 5.1 (b). The isotopic pattern for the *m/z* = 300 peak in the $Pd(tftm)_2$ spectrum is different than the *m/z* = 300 peak in the co-sublimation spectrum. The addition of the copper species in this peak causes the second isotopic peak to be more intense than the *m/z* = 300 peak in the palladium species. That difference of patterns among the co-sublimation and single spectra indicate the isobaric overlap.

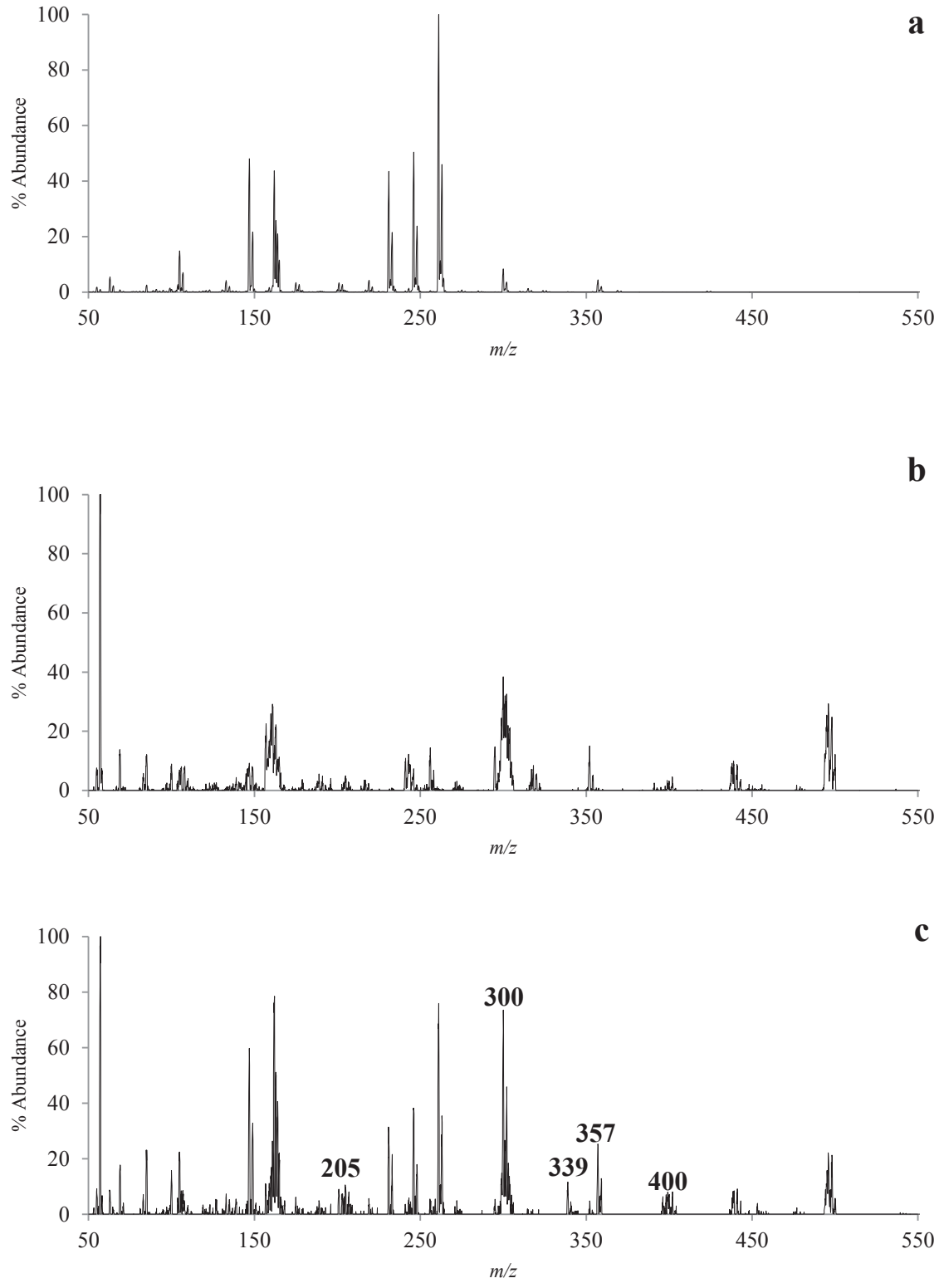

Figure 5.1: The 70 eV positive EI mass spectra of (a) $Cu(acac)_2$, (b) $Pd(tftm)_2$, and (c) the co-sublimation of $Pd(tftm)_2$ and $Cu(acac)_2$. Mixed ligand or ligand exchange peaks are highlighted in bold.

Species	m/z	Rel. Ab.	Species	m/z	Rel. Ab.
$[Pd(tftm)(acac)]^+$	400	8	$[Cu(tftm)_2]^+$	453	4
$[Pd(acac)]^+$	205	13	$[Cu(tftm)(acac)]^+$	357	34
			$[Cu(tftm)_2 - 2\ tBu]^+$	339	12
			$[Cu(tftm)(acac)-\ tBu]^+$	300	100

Table 5.1: The relative abundances of the partial, mixed ligand, and complete exchange products of the co-sublimation of $Pd(tftm)_2$ and $Cu(acac)_2$ as presented in Figure 5.1.

5.2.2 Co-sublimation of $Pd(tftm)_2$ & $Cu(eeac)_2$

The mass spectra presented in Figure 5.2 are vertically stacked in order to better visualize the extent of ligand exchange occurring. The top portion, Figure 5.2 (a), features the single $Cu(eeac)_2$ spectrum showing typical fragmentation patterns such as the parent peak at *m/z* = 317 , the loss of an ethyl group at *m/z* = 288, the loss of another ethyl group at *m/z* = 258, the loss of an entire *eeac* ligand at *m/z* = 191, and finally another subsequent loss of an ethyl group at *m/z* = 161. The middle portion, Figure 5.2 (b) shows the spectrum of $Pd(tftm)_2$, similar to Figure 4.1, but over a different mass range. The bottom portion, Figure 5.2 (c), corresponds to the spectrum of the co-sublimation of $Pd(tftm)_2$ and $Cu(eeac)_2$ using a two-looped filament.

It is important to note that there are peaks present in the co-sublimation spectrum that are not featured in the previous single spectra which is a clear indication of gas-phase ligand exchange. Those species that underwent any amount of ligand exchange, which includes partial exchanges, mixed ligand formations, and complete exchanges are labeled within the spectra and highlighted in bold. The *m/z* values and relative abundances for the fragmentation of the single species, the co-sublimation species, as well as the exchange products are featured in Table 5.2. The relative abundances were calculated in relation to the most intense peak of importance, that is, the peak with the most intensity that is either a partial exchange, mixed ligand, or full exchange product. For example, in Figure 5.2

(c), the most intense peak is *m/z* = 57, however, *m/z* = 317 was selected as the base peak for the relative abundance calculations since it was the most intense peak of importance that corresponds to the mixed ligand formation product of $[Cu(tftm– CF_3)(eeac)]^+$. Results from this co-sublimation experiment show partial, mixed, and full ligand exchange for both the copper and the palladium species, however the copper appears to have a greater success in performing the complete exchange of ligands.

The co-sublimation of $Pd(tftm)_2$ with $Cu(eeac)_2$ shows many mixed ligand species and fragments of these species. With the presence of so many fragmented mixed ligands, it may be that mixed ligand formation is favored by fragmented ligands as opposed to fully intact ligands. The prevalence of such high abundances of mixed ligand products is a promising indication of successful gas-phase ligand exchange.

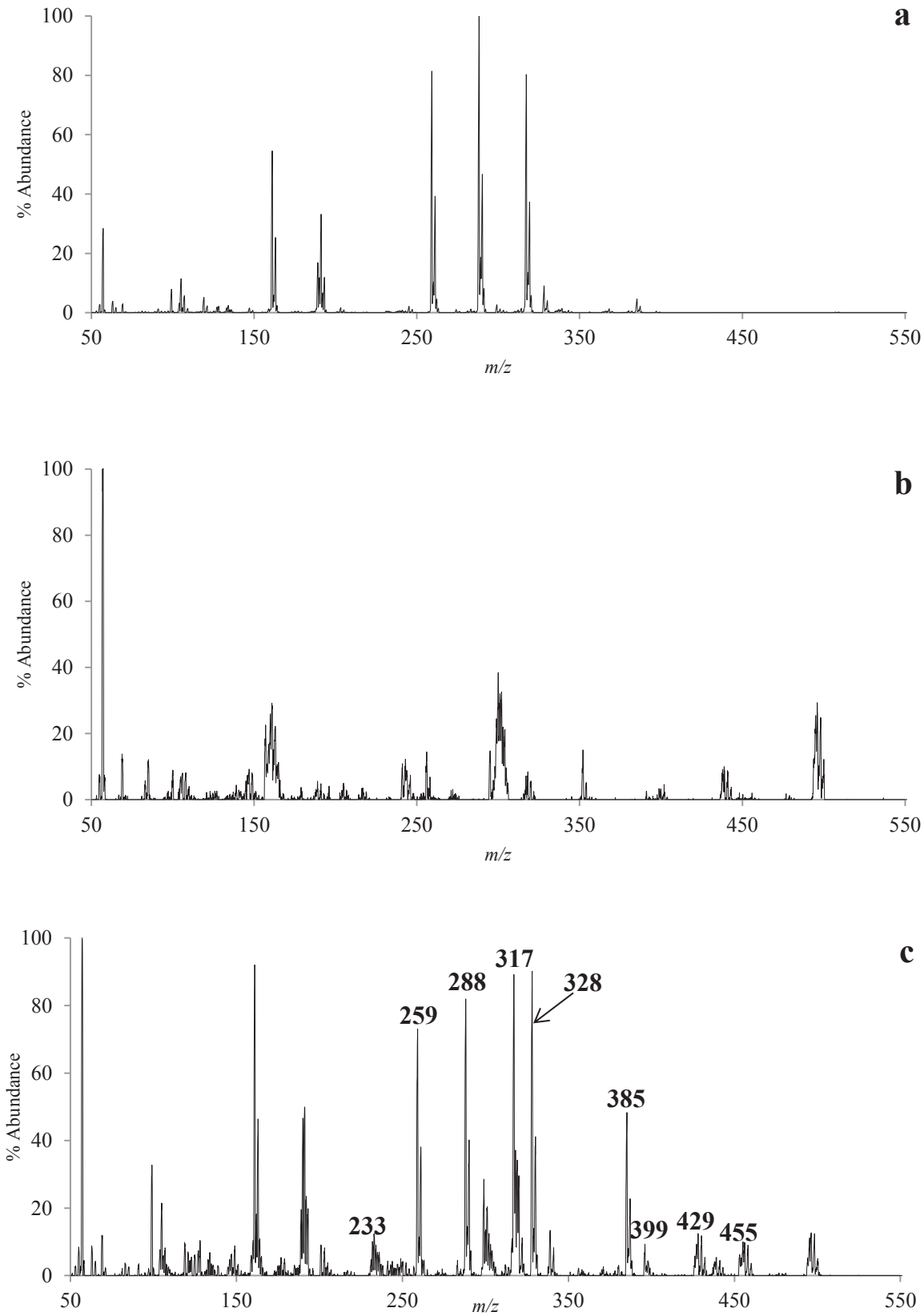

Figure 5.2: The 70 eV positive EI mass spectra of (a) $Cu(eeac)_2$, (b) $Pd(tftm)_2$, and (c) the co-sublimation of $Pd(tftm)_2$ and $Cu(eeac)_2$. Mixed ligand or ligand exchange peaks are highlighted in bold.

Species	m/z	Rel. Ab.	Species	m/z	Rel. Ab.
$[Pd(tftm)(eeac)]^+$	429	14	$[Cu(tftm)_2]^+$	455	11
$[Pd(tftm)(eeac) – Et]^+$	399	9	$[Cu(tftm)(eeac)]^+$	385	52
$[Pd(eeac)]^+$	233	13	$[Cu(tftm)(eeac) – t\text{Bu}]^+$	328	93
			$[Cu(tftm– CF_3)(eeac)]^+$	317	100
			$[Cu(tftm – CF_3)(eeac – Et)]^+$	288	88
			$[Cu(tftm – CF_3 \& t\text{Bu})(eeac)]^+$	259	75

Table 5.2: The relative abundances of the partial, mixed ligand, and complete exchange products of the co-sublimation of $Pd(tftm)_2$ and $Cu(eeac)_2$ as presented in Figure 5.2.

5.2.3 Co-sublimation of $Pd(tftm)_2$ & $Cu(hfac)_2$

The mass spectra presented in Figure 5.3 are vertically stacked in order to better visualize the extent of ligand exchange occurring. The top portion, Figure 5.3 (a), features the single $Cu(hfac)_2$ spectrum showing typical fragmentation patterns such as the parent peak at m/z = 476 , the loss of a CF_3 group at m/z = 408, the loss of another CF_3 group at m/z = 339, and finally the loss of an entire *hfac* ligand and one of its CF_3 groups at m/z = 200. The middle portion, Figure 5.3 (b) shows the spectrum of $Pd(tftm)_2$, similar to Figure 4.1 but over a different mass range. The bottom portion, Figure 5.3 (c), corresponds to the spectrum of the co-sublimation of both $Pd(tftm)_2$ and $Cu(hfac)_2$ using a two-looped filament.

It is important to note that there are peaks present in the co-sublimation spectrum that are not featured in the previous single spectra which is a clear indication of gas-phase ligand exchange. Those species that underwent any amount of ligand exchange, which includes partial exchanges, mixed ligand formations, and complete exchanges are labeled within the spectra and highlighted in bold. The m/z values and relative abundances for the fragmentation of the single species, the co-sublimation species, as well as the exchange products are featured in Table 5.3. The relative abundances were calculated in

relation to the most intense peak of importance, that is, the peak with the most intensity that is either a partial exchange, mixed ligand, or full exchange product. For example, in Figure 5.3 (c), the most intense peak is *m/z* = 57, however, *m/z* = 396 was selected as the base peak for the relative abundance calculations since it was the next highest intense peak corresponding to the ligand exchange product of $[Cu(tftm)(tftm - tBu)]^+$. Results from this co-sublimation experiment show partial, mixed, and full ligand exchange for both the copper and the palladium species, however the copper appears to have a greater success in performing the complete exchange of ligands.

The co-sublimation of $Pd(tftm)_2$ with $Cu(hfac)_2$ has successfully yielded some prominent and novel ligand exchange combinations. As there are the *tftm* exchanges from palladium similarly seen in Section 5.4, as well as the mixed ligand combination for both metals, it is exciting to see the exchange of hexfluoroacetylacetonate from copper to palladium. Though there is not a total exchange represented, the partial exchange of an *hfac* group exhibiting the loss of a CF_3 group (*m/z* = 243) is present with a decent relative abundance as seen in Table 5.3.

Even more exciting, however, may be the peak at *m/z* = 263, representing $[Pd(hfac - CF_2)]^+$. This peak, though having a slightly lower relative abundance in relation to $[Pd(hfac - CF_3)]^+$, is worth observation because it not only shows partial ligand exchange from a gas phase co-sublimation reaction, it also exhibits the fluorine migration common in hexafluoroacetylacetonate co-sublimation reactions. Further research should study the collision cell reactions with these compounds in an attempt to mechanistically describe this novel phenomenon.

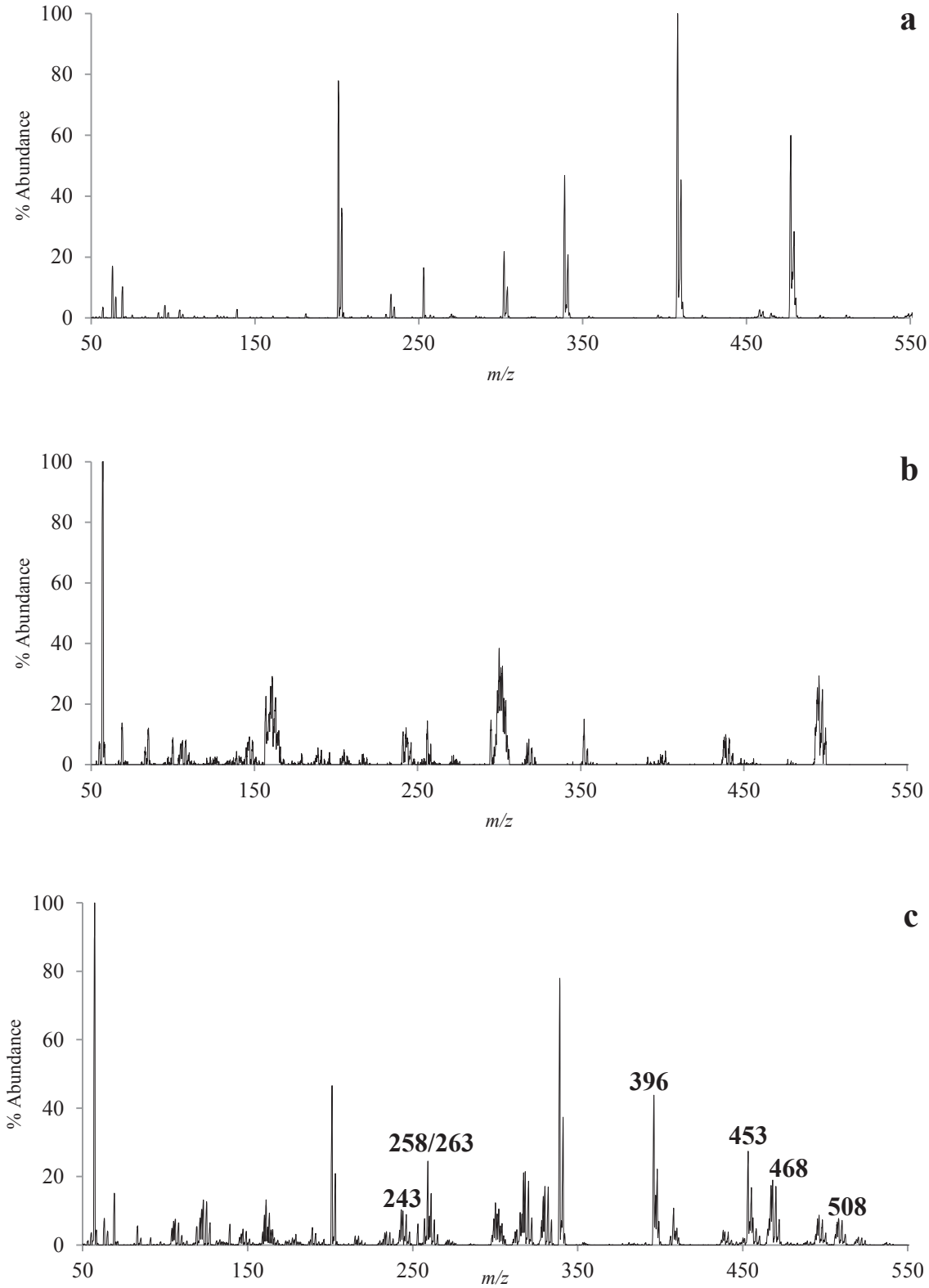

Figure 5.3: The 70 eV positive EI mass spectra of (a) $Cu(hfac)_2$, (b) $Pd(tftm)_2$, and (c) the co-sublimation of $Pd(tftm)_2$ and $Cu(hfac)_2$. Mixed ligand or ligand exchange peaks are highlighted in bold.

Species	m/z	Rel. Ab.	Species	m/z	Rel. Ab.
$[Pd(tftm)(hfac)]^+$	508	19	$[Cu(tftm)(hfac)]^+$	468	41
$[Pd(hfac - CF_2)]^+$	263	14	$[Cu(tftm)_2]^+$	453	62
$[Pd(hfac - CF_3)]^+$	243	23	$[Cu(tftm)(tftm - t\text{Bu})]^+$	396	100
			$[Cu(tftm)]^+$	258	52

Table 5.3: The relative abundances of the partial, mixed ligand, and complete exchange products of the co-sublimation of $Pd(tftm)_2$ and $Cu(hfac)_2$ as presented in Figure 5.3.

5.2.4 Co-sublimation of $Pd(tftm)_2$ & $Zn(hfac)_2$

The mass spectra presented in Figure 5.4 are vertically stacked in order to better visualize the extent of ligand exchange occurring. The top portion, Figure 5.4 (a), features the single $Zn(hfac)_2$ spectrum showing typical fragmentation patterns such as the parent peak at *m/z* = 477, the loss of a CF_3 group at *m/z* = 409, the loss of an *hfac* ligand at *m/z* = 270, and finally the fluorine migration at *m/z* = 221 which will be discussed shortly. The middle portion, Figure 5.4 (b) shows the spectrum of $Pd(tftm)_2$, similar to Figure 4.1 but over a different mass range. The bottom portion, Figure 5.4 (c), corresponds to the spectrum of the co-sublimation of $Pd(tftm)_2$ and $Zn(hfac)_2$ using a two-looped filament.

It is important to note that there are peaks present in the co-sublimation spectrum that are not featured in the previous single spectra which is a clear indication of gas-phase ligand exchange. Those species that underwent any amount of ligand exchange, which includes partial exchanges, mixed ligand formations, and complete exchanges are labeled within the spectra and highlighted in bold. The *m/z* values and relative abundances for the fragmentation of the single species as well as the co-sublimation species are featured below in Table 5.4. The relative abundances were calculated in relation to the most intense peak of importance, that is, the peak with the most intensity that is either a partial exchange, mixed ligand, or full exchange product. For example, in Figure 5.4 (c), the

most intense peak is *m/z* = 409, which is selected as the base peak for relative abundance calculations. Results from this co-sublimation experiment show partial, mixed, and full ligand exchange for both the copper and the palladium species, however the zinc appears to have a greater success in performing the complete exchange of ligands.

Similar to the co-sublimation of $Pd(tftm)_2$ with $Ni(hfac)_2$ as seen in Chapter 4, Section 4.2.7, there is once again evidence of fluorine migration at *m/z* = 221. Though this peak does not currently indicate mixed ligand formation, with future collision cell reaction analysis, this fluorine migration may play a role in the mechanism of mixed ligand formation or even ligand exchange. One of the most important features of this co-sublimation spectra is that it contains many isobaric peaks. Each of these isobaric peaks contains a ligand exchange product as well as a fragmentation product of one of the original molecules. For instance, *m/z* = 243 is indicative of both $[Pd(tftm - tBu)]^+$ and $[Pd(hfac - CF_3)]^+$. The peak at *m/z* = 397 is also isobaric, containing both $[Zn(tftm)(tftm - tBu)]^+$ and $[Zn(hfac\text{-}CF_3)]^+$. With a high frequency of isobaric peaks, the relative abundances of the mixed ligands within these peaks is difficult to accurately measure with the overlap of normal fragmentation. This issue can also be solved in the future with collision cell reactions. And finally, *m/z* = 409 is the most intense peak on the spectrum and is also isobaric as it contains $[Zn(hfac)(hfac - CF_3)]^+$ and $[Zn(hfac)(tftm - tBu)]^+$.

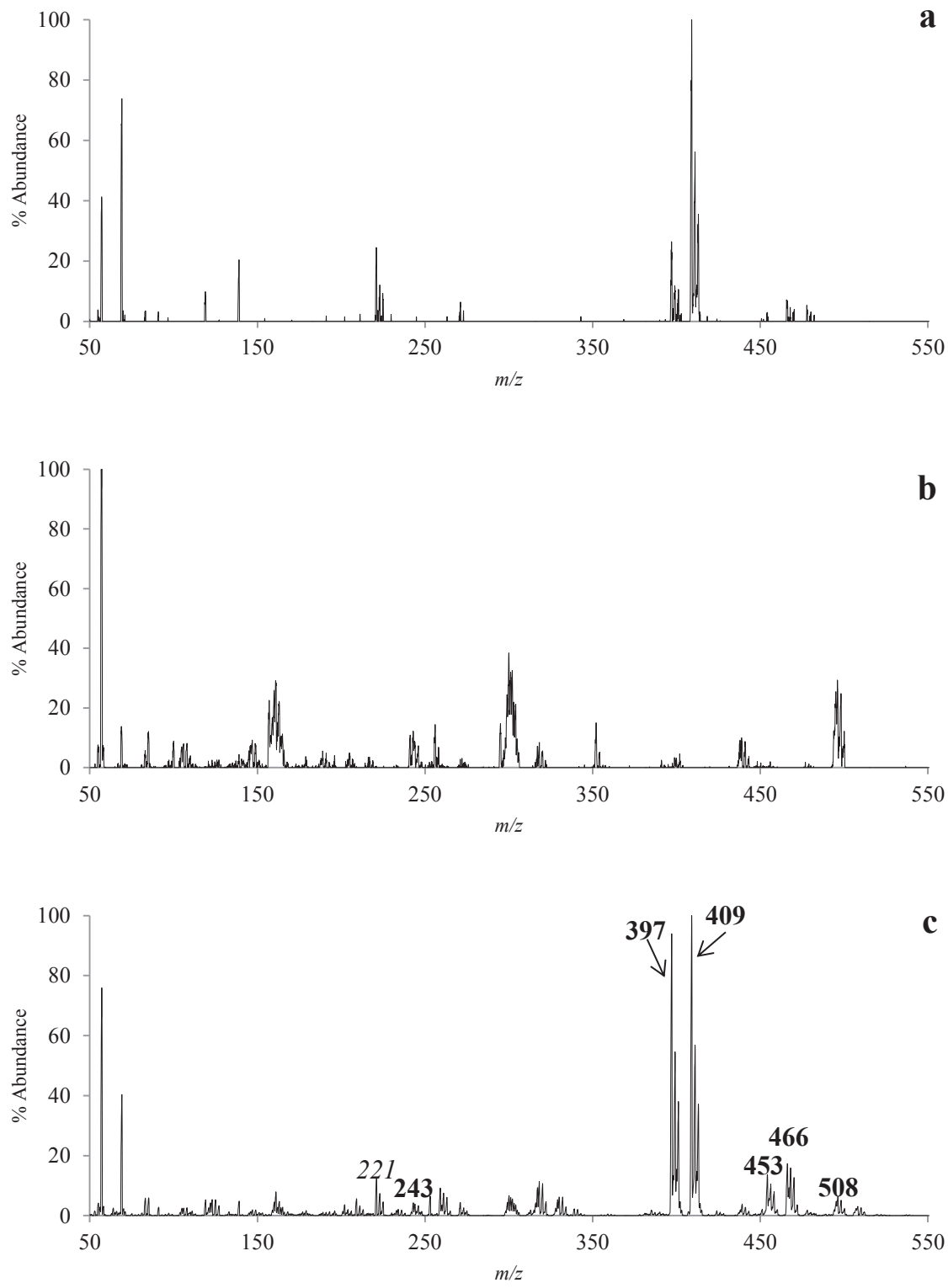

Figure 5.4: The 70 eV positive EI mass spectra of (a) $Zn(hfac)_2$, (b) $Pd(tftm)_2$, and (c) the co-sublimation of $Pd(tftm)_2$ and $Zn(hfac)_2$. Mixed ligand or ligand exchange peaks are highlighted in bold. Fluorine migration is indicated in italics.

Species	m/z	Rel. Ab.	Species	m/z	Rel. Ab.
[Pd(tftm)(hfac)]+	508	3	$[Zn(tftm)(hfac)]^+$	466	21
$[Pd(hfac - CF_3)]^+$	243	5	$[Zn(tftm)_2]^+$	455	16
			$[Zn(hfac)(tftm - tBu)]^+$	409	100
			$[Zn(tftm)(tftm - tBu)]^+$ / $[Zn(tftm)(hfac-CF_3)]^+$	397	99

Table 5.4: The relative abundances of the partial, mixed ligand, and complete exchange products of the co-sublimation of $Pd(tftm)_2$ and $Zn(hfac)_2$ as presented in Figure 5.4.

Chapter 6: Supplemental Spectra of Newly Synthesized β-diketonate Complexes

6.1 Introduction

The contents of this Chapter include several supplemental spectra of novel metal β-diketonate complexes that were proven successful via single species positive EI mass spectrometry but did not undergo any co-sublimation reactions nor selective reactions using the collision cell. The compounds featured herein contain different metals than what was presented in previous Chapters, including magnesium, cobalt, copper, and cadmium forming either trifluoroacetylacetonate (tftm) or diethylacetylacetonate (eeac) complexes. Both the synthesis and percent yield of these complexes is outlined in Chapter 3. As noted in Chapter 3, mass spectrometric results are not available for all of the synthesized compounds. Further investigation into the co-sublimation and collision cell reactions of these complexes along with $Pd(tftm)_2$ and other metal β-diketonate compounds would be beneficial in further understanding of the mechanism of these gas-phase ligand exchanges.

6.2 Results and Discussion

6.2.1 Magnesium trifluorotrimethylacetylacetonate ($Mg(tftm)_2$)

Magnesium trifluorotrimethylacetylacetonate ($Mg(tftm)_2$) was synthesized according to the methods outlined in Chapter 3, Section 3.3.9. Positive EI mass spectrometry was used to confirm the identity and thus overall success of the synthesis reaction. The resulting spectrum is featured in Figure 6.1 with fragmentation products presented in Table 6.1. In some mass spectra, sodium contamination is present and easily identified given the mass difference of 23. This sodium contamination is evident in Figure 6.1 at *m/z* = 437. The most dominant peak in the spectrum, *m/z* = 357, corresponds to the loss of a *t*Bu group where the intact $[Mg(tftm)_2]^+$ appears at *m/z* = 414. Since this fragment is the most dominant, it may be a candidate for co-sublimation reactions with $Pd(tftm)_2$ and/or other compounds of interest along with additional selective reactions to shed light on possible reaction mechanisms.

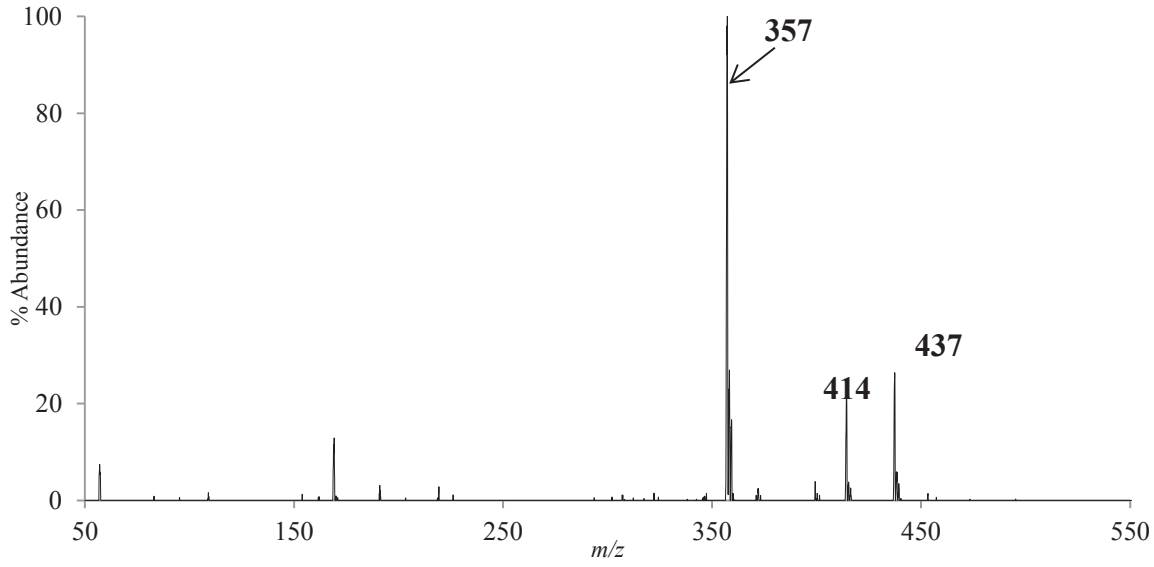

Figure 6.1: The 70 eV positive EI mass spectrum of $Mg(tftm)_2$.

Species	*m/z*	Relative Abundance
$[Mg(tftm)_2 + Na]^+$	437	24
$[Mg(tftm)_2]^+$	414	20
$[Mg(tftm)(tftm - tBu)]^+$	357	100

Table 6.1: The relative abundances of the fragmentation species of $Mg(tftm)_2$ as presented in Figure 6.1.

6.2.2 Magnesium diethylacetylacetonate ($Mg(eeac)_2$)

Magnesium diethylacetylacetonate ($Mg(eeac)_2$) was synthesized according to the methods outlined in Chapter 3, Section 3.5.3. Positive EI mass spectrometry was used to confirm the identity and thus overall success of the synthesis reaction. The resulting spectrum is featured in Figure 6.2 with the fragmentation products and relative abundances presented in Table 6.2. The parent peak at *m/z* = 278, corresponding to $[Mg(eeac)_2]^+$, is observed as is the loss of an ethyl group at *m/z* = 249. The loss of a second ethyl group at *m/z* = 221 is detected as is the loss of an intact ligand at *m/z* = 151 to produce $[Mg(eeac)]^+$.

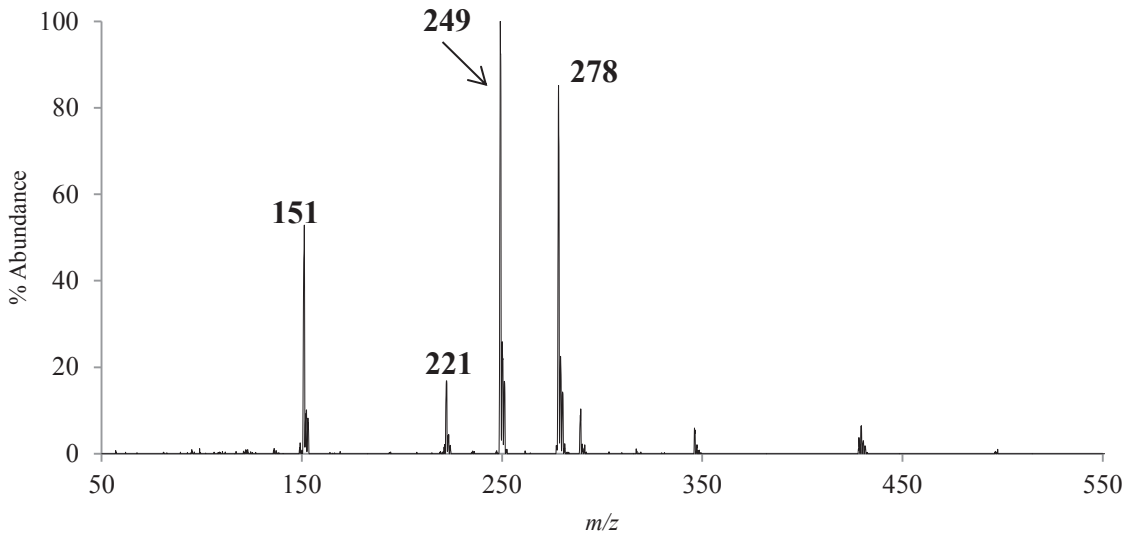

Figure 6.2: The 70 eV positive mass spectrum of $Mg(eeac)_2$.

Species	*m/z*	Relative Abundance
$[Mg(eeac)_2]^+$	278	79
$[Mg(eeac)(eeac - Et)]^+$	249	100
$[Mg(eeac - Et)(eeac - Et)]^+$	221	17
$[Mg(eeac - Et)]^+$	151	55

Table 6.2: The relative abundances of the fragmentation species of $Mg(eeac)_2$ as presented in Figure 6.2.

6.2.3 Cobalt trifluorotrimethylacetylacetonate ($Co(tftm)_2$)

Cobalt trifluorotrimethylacetylacetonate ($Co(tftm)_2$) was synthesized according to the methods outlined in Chapter 3, Section 3.3.3. Positive EI mass spectrometry was used to confirm the identity and thus overall success of the synthesis reaction. The resulting spectrum is featured below in Figure 6.3 and the relative abundances of the fragmentation products are found in Table 6.3. This compound has been studied previously by Hunter and was synthesized for confirmation purposes. More details can be found about this compound and its gas-phase reactivity by referencing Hunter et.al.[17]

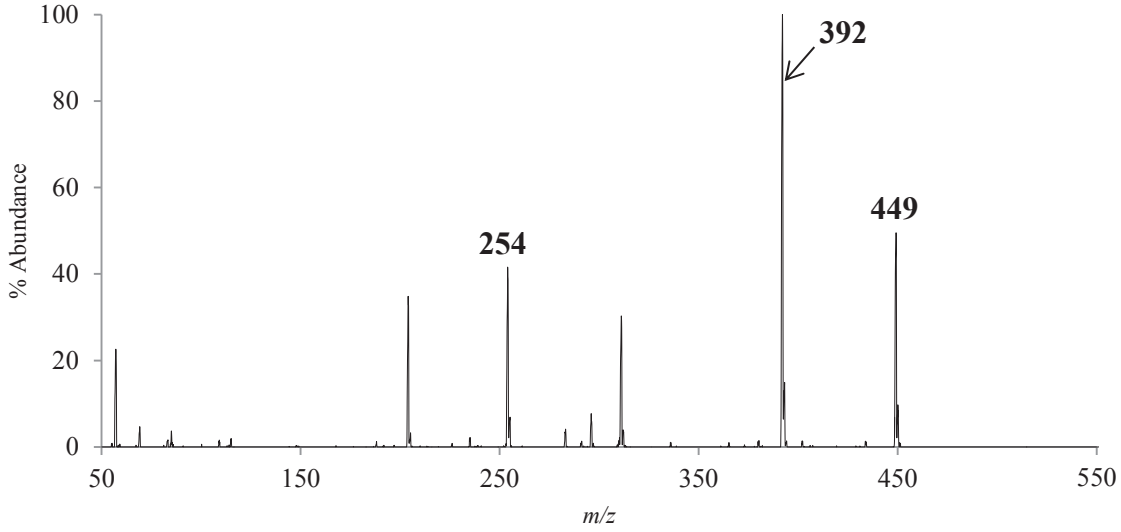

Figure 6.3: The 70 eV positive mass spectrum of $Co(tftm)_2$.

Species	*m/z*	Relative Abundance
$[Co(tftm)_2]^+$	449	52
$[Co(tftm)(tftm - tBu)]^+$	392	100
$[Co(tftm)]^+$	254	41

Table 6.3: The relative abundances of the fragmentation species of $Co(tftm)_2$ as presented in Figure 6.3.

6.2.4 Cobalt diethylacetylacetonate ($Co(eeac)_2$)

Cobalt diethylacetylacetonate ($Co(eeac)_2$) was synthesized according to the methods outlined in Chapter 3, Section 3.5.4. Positive EI mass spectrometry was used to confirm the identity and thus overall success of the synthesis reaction. The resulting spectrum is featured below in Figure 6.4 with its corresponding relative abundances of fragmentation presented in Table 6.4. The parent peak is located at *m/z* = 313 for $[Co(eeac)_2]^+$ followed by the loss of an ethyl group is confirmed at *m/z* = 284. $Co(eeac)_2$ also appears to lose an entire ligand to produce $[Co(eeac)]^+$ at *m/z* = 186.

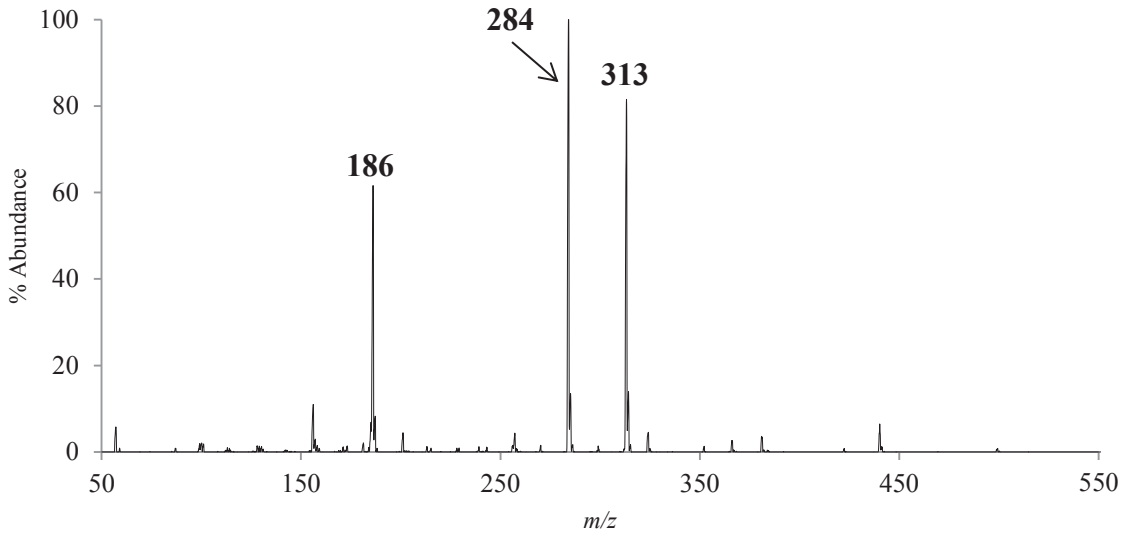

Figure 6.4: The 70 eV positive mass spectrum of $Co(eeac)_2$.

Species	*m/z*	Relative Abundance
$[Co(eeac)_2]^+$	313	80
$[Co(eeac)(eeac - Et)]^+$	284	100
$[Co(eeac)]^+$	186	57

Table 6.4: The relative abundances of the fragmentation species of Co(eeac)2 as presented in Figure 6.4.

6.2.5 Copper trifluorotrimethylacetylacetonate ($Cu(tftm)_2$)

Copper trifluorotrimethylacetylacetonate ($Cu(tftm)_2$) was synthesized according to the methods outlined in Chapter 3, Section 3.3.4. EI mass spectrometry was used to confirm the identity and thus overall success of the synthesis reaction. The resulting spectrum is featured below in Figure 6.5, along with the relative abundances of the fragmentation of $Cu(tftm)_2$ in Table 6.5. This compound has been studied previously by Hunter and was synthesized for confirmation purposes. More details can be found about this compound and its gas-phase reactivity by referencing Hunter et.al.[17]

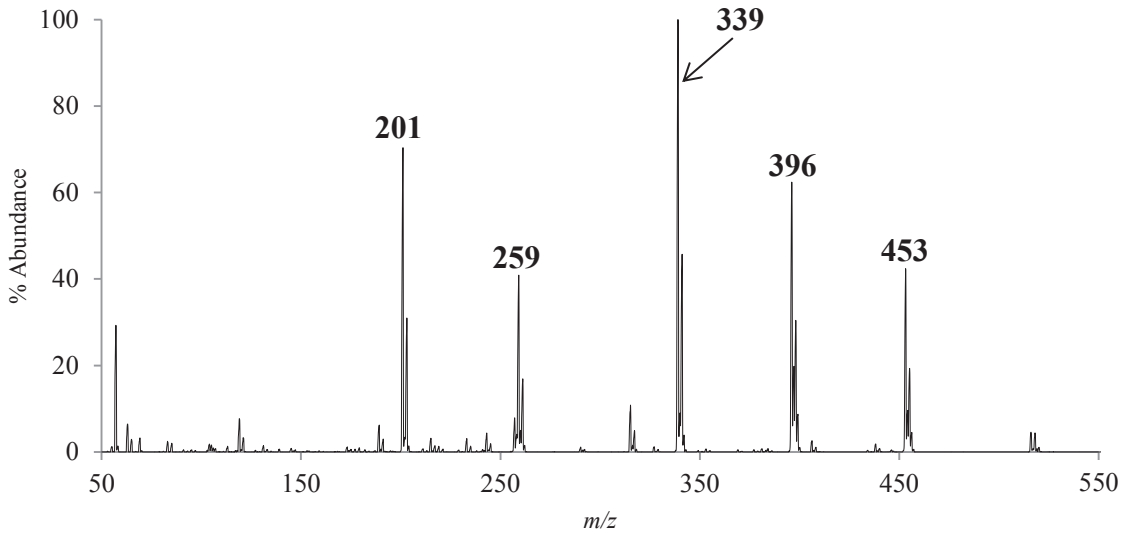

Figure 6.5: The 70 eV positive mass spectrum of $Cu(tftm)_2$.

Species	*m/z*	Relative Abundance
$[Cu(tftm)_2]^+$	453	43
$[Cu(tftm)(tftm - tBu)]^+$	396	63
$[Cu(tftm - tBu)(tftm - tBu)]^+$	339	100
$[Cu(tftm)]^+$	259	42
$[Cu(tftm - tBu)]^+$	201	66

Table 6.5: The relative abundances of the fragmentation species of $Cu(tftm)_2$ as presented in Figure 6.5.

6.2.6 Cadmium trifluorotrimethylacetylacetonate ($Cd(tftm)_2$)

Cadmium trifluorotrimethylacetylacetonate ($Cd(tftm)_2$) was synthesized according to the methods outlined in Chapter 3, Section 3.3.2. Positive EI mass spectrometry was used to confirm the identity and thus overall success of the synthesis reaction. The resulting spectrum is featured below in Figure 6.6. This compound, though very similar to the $Pd(tftm)_2$ that was so heavily emphasized in this study, was not investigated herein due to the fact that Silvestri was conducting a simultaneous study. Like $Mg(tftm)_2$, this complex also showed signs of sodium contamination given the peak located at *m/z* = 525, which 23 more than the parent peak located at *m/z* = 502. The loss of a *t*Bu group is also observed at *m/z* = 445, and the single ligand species is observed at *m/z* = 307.

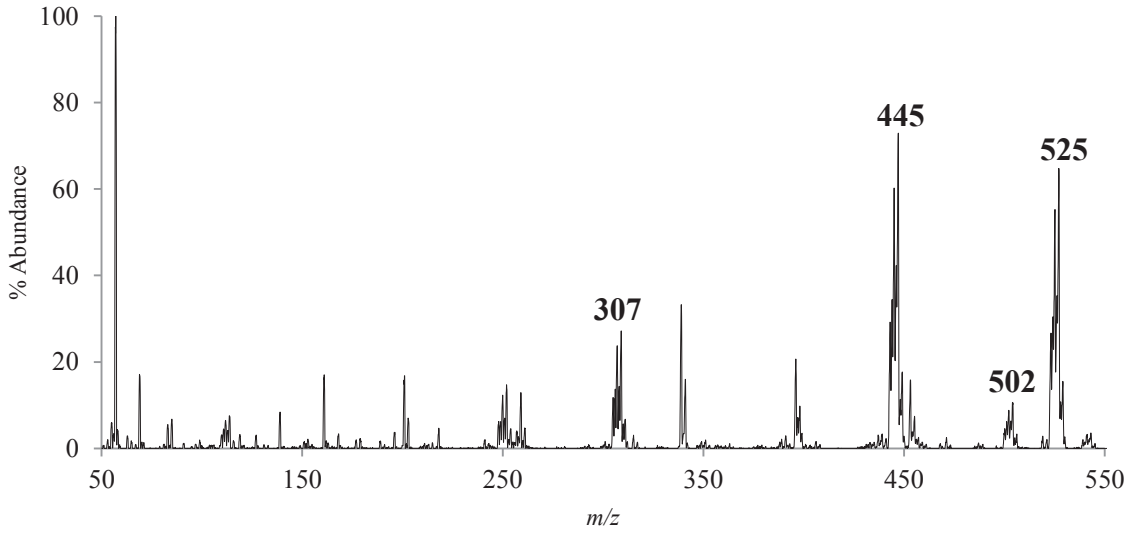

Figure 6.6: The 70 eV positive mass spectrum of $Cd(tftm)_2$.

Species	*m/z*	Relative Abundance
$[Cd(tftm)_2 + Na]^+$	525	89
$[Cd(tftm)_2]^+$	502	15
$[Cd(tftm)(tftm - tBu)]^+$	445	100
$[Cd(tftm)]^+$	307	37

Table 6.6: The relative abundances of the fragmentation species of $Cd(tftm)_2$ as presented in Figure 6.6.

Chapter 7: Conclusions and Future Work

The results presented in Chapters 4 and 5 show strong evidence for gas-phase ligand exchange involving palladium trifluorotrimethylacetylacetonate with various other metal β-diketonate ligands. These conclusions along with the mechanisms proposed in Chapter 4 were made on the basis of concrete mass spectral analysis with careful monitoring of the relative ion intensities associated with each reaction.

Though each of the reactions investigated in Chapters 4 and 5 differ in metal and ligand content, the selective reactions provide evidence for gas-phase ligand exchange. Some reactions showed only partial exchange, some showed the formation of mixed ligand metal complexes, and some reactions even provided evidence for complete ligand exchange. Since Pd is much more isotopically rich than Ni, Cu, or Zn, determination of Pd containing compounds via mass spectral analysis was possible due to the distinct isotopic peak pattern each of those compounds possessed. The selective reactions of $Pd(tftm)_2$ cations with neutral Ni containing β-diketonate complexes in the collision cell provide the best evidence for particular reaction pathways. Regardless of how the species were introduced, whether via co-sublimation gas-phase reactions or selective gas-phase reactions, there was a vast amount of evidence in support of ligand exchange.

Though there has been much progress in this study as a whole, this research is still in its infancy stages. One of the first steps in future research should be attempting these same experiments with new compounds. By selecting a second row transition metal (Pd) as opposed to the previously studied first row transition metals, the reaction behavior differed noticeably. Since some Mg containing compounds have already been

synthesized in this study, as shown in Chapter 6, these can easily be co-sublimed with $Pd(tftm)_2$ or any other previously studied metal β-diketonate for that matter to search for gas-phase ligand exchange. There is a multitude of possibilities with regard to the synthetic approach of novel complexes given the combinations of ligands with transition metals, alkali metals, alkaline earth metals, or maybe even metalloids.

New selective reactions within the collision cell should also be a priority in future studies. The selective reactions in the collision cell offer insight as to how these gas-phase reactions may occur mechanistically. The observation of these reactions involving different metal and/or ligand precursors can show either differences or similarities among the gas-phase reaction properties of these and future compound combinations. Another idea to consider is performing a co-sublimation reaction with two different metal β-diketonate complexes, but with the introduction of a reactive gas such as ammonia in the collision cell. Observations can then be made on whether or not the introduction of these gases prevents, complicates, or even facilitates in the fragmentation and formation of the mixed ligand species, or even if the gas molecules can become incorporated into the structure.

Another area of interest with this work involves performing these gas-phase reactions in anionic mode as opposed to the positive cationic mode in this study. The set-up for this investigation would be identical to the set-up of the one in this study, however, the instrument will recognize anionic fragments as opposed to cationic ones. This data could offer an entirely new perspective on the gas-phase ligand exchange reactions of all metal β-diketonates.

References

1. Condorelli, G.G., Malandrino, G., Fragala, I.L., *Coordination Chemistry Reviews* **2007** 251, 1931 – 1950.
2. Burtoloso, A.C., *Synlett* **2005** 18, 2859 – 2860.
3. Mac Leod, T.C.O., Kopylovich, M.N., Guedes da Silva, F.C., Mahmudov, K.T., Pombeiro, A.J.L., *Applied Catlaysis A: General* **2012** 439 – 440, 15 – 23.
4. Sheikh, J., Juneja, H., Ingle, V., Ali, P., Hadda, T.B., *Journal of Saudi Chemical Society* **2013** 17, 269 – 276.
5. Raman, N., Jeyamurugan, R., Usha Rani, R., Baskaran, T., Mitu, L., *Journal of Coordination Chemistry* **2010** 63, 1629 – 1644.
6. Kumar, R., Jain, S.K., Misra, R.K., Kachchwaha, M., Khatri, *International Journal of Environmental Science and Technology* **2012** 9, 79 – 84.
7. Divya, V., Reddy, M.L.P, *Journal of Material Chemistry* **2012** 1, 160.
8. Tong, M., Chen, H., Yang, Z., Wen, R., *International Journal of Molecular Sciences* **2011** 12, 1756 – 1766.
9. Fragoza-Mar, L., Olivares-Xometl, O., Dominguez-Aguilar, M.A., Flores, E.A., Arellance-Lozada, P., Jimenez-Cruz, F., *Corrosion Science* **2012** 61, 174 – 184.
10. Wyatt, M.F., Harvard S., Stein, B.K., Brenton, A.G., *Rapid Communications in Mass Spectrometry* **2008** 22, 11-18.
11. Sloop, J.C., Baumgarder, C.L., Washington, G., Loehle, W.D., Sankar, S.S., Lewis, A.B., *Journal of Fluorine Chemistry* **2006** 127, 780 – 786.
12. Suslov, D.S., Bykov, M.V., Belova, M.V., Abramov, P.A., Tkach, V.S., *Journal of Organometallic Chemistry* **2014** 752, 37 – 43.

13. Kukkola, J., Mohl, M., Leino, A.R., Maklin, J., Halonen, N., Shchukarev, A., Konya, Z., Jantunen, H., Kordas, K., *Sensors and Actuators B: Chemical* **2013** 186, 90 – 95.

14. Watson, W.H., Lin, C.T., *Inorganic Chemistry* **1965** 5, 1074 – 1077.

15. Zheng, B., Goldberg, C., Eisenbraun, E.T., Liu, J. Kaloyeros, A.E., Toscano, P.J., Murarka, S.P., Loan, J.F., Sullivan, J., *Materials Chemistry and Physics* **1995** 41, 173 – 181.

16. Lerach, J.O. Investigations into the Gas-Phase Rearrangements of Some Transition Metal β-Diketonate Complexes, MS Thesis, Youngstown State University, August 2008.

17. Hunter, G.O. The Examination of the Stability and Reactivity of Select Transition Metal β-Diketonate Complexes during Gas-Phase Ligand Exchange Reactions, MS Thesis, Youngstown State University, December 2009.

18. Lerach, J.O., Leskiw, B.D., *Rapid Communications in Mass Spectrometry* **2008** 22, 4139 – 4146.

19. Hunter, G.O., Lerach, J.O., Lockso, T.R., Leskiw, B.D., *Rapid Communications in Mass Spectrometry* **2010** 24, 129 – 137.

20. Hunter, G.O., Leskiw, B.D., *Rapid Communications in Mass Spectrometry* **2012** 26, 369 – 376.

21. Wyatt, M.F., Harvard, S., Stein, B.K., Brenton, A.G, *Rapid Communications in Mass Spectrometry* **2008** 22, 11 – 18.

22. Dean, L.K.L., DiDonato, G.C., Wood, T.D., Busch, K.L., *Inorganic Chemistry* **1988** 27, 4622 – 4627.

23. Pierce, J.L., Busch, K.L., Cooks, R.G., Walton, R.A., *Inorganic Chemistry* **1982** 21, 2597 – 2602.

24. Bartlett, M.G., Bruce, D.A., Busch, K.L., *Applied Spectroscopy* **1997** 51, 1757 – 1760.

25. Westmore, J.B., *Chemical Reviews* **1976** 76, 695 – 715.

26. Takats, Z., Wiseman, J.M., Cooks, R.G., *Journal of Mass Spectrometry* **2005** 40, 1261 – 1275.

27. Brotons, J.A., Olea-Serrano, M.F., Villalobos, M., Pedraza, V., Olea, N., *Environmental Perspectives* **1995** 608-612.

28. Blaum, K., *Physics Reports* **2006** 425, 1 – 78.

29. Cornett, D.S., Reyzer, M.L., Chaurand, P., Caprioli, R.M., *Nature* **2007** 4, 828 – 833.

30. Plumb, R.S., Stumpfl, C.L., Gorenstein, M.V., Castro-Perez, J.M., Dear, G.J., Anthony, M., Sweatman, B.C., Connor, S.C., Haselden, J.N., *Rapid Communications in Mass Spectrometry* **2002** 16, 1991 – 1996.

31. Rosman, K.J.R., Taylor, P.D.P, *Pure Applied Chemistry* **1999** 71, 1593 – 1607.

Appendix A

Operational Instructions for the TSQ 7000 Triple Quadripole Electron Impact Mass Spectrometer

I. Quad 1 Full Scan Analysis

a. To run a single sample for mass spectral analysis, the following steps must be completed.

i. To begin, make sure that the mass spectrometer is on and ready to run. The switch on the probe should also be turned to the 'power on' position.

ii. In the TSQ tune quadrant windows, locate the screen labeled as 'valve'.

iii. Make sure that the source temperature is set at 160^{o}C and the manifold temperature is 80^{o}C. These can be adjusted on the lefthand side using either the +10 or -10 buttons.

iv. For this type of run, also be sure that the collision cell gas is turned off. If any of the 'x's around valve lines are highlighted in yellow, double click them to turn them green, indicating that the collision gas is no longer flowing.

v. While in the 'valve' window, type 'analysis' on the bottom of the screen.

vi. In the upper lefthand corner of the screen, click the button that says 'file' and name the upcoming spectral file as anything pertaining to the sample. For instance, if running $Ni(acac)_2$, it would be advisable to save the file with the same name. If any other name or code is used other than the name of the sample, this must be indicated in the laboratory notebook.

vii. Locate the window labeled as ‘guide’ and click on the ‘old main’ button.

viii. Next, click on the button labeled as ‘scan’ to change the scan parameters.

ix. For a full scan analysis, click the button labeled ‘Q1MS’ in the top lefthand corner.

x. Click ‘scan’ on the left.

xi. Observe the current conditions. For an ideal run, these conditions should be as follows from left to right:

1. First mass = 50 (FM 50)
2. Last mass = 650 (LM 650)
3. Scan time = 1.2 (ST 1.2)
4. Scan rate = 500 (500 U/S)

xii. If any of these need to be changed, simply click the corresponding button and input the correct value. Once these parameters have been set, click ‘OK’ and you will be brought back to the main screen.

xiii. Click ‘OLD MAIN’ once again.

xiv. This time, click ‘ACQU’ on the top line to prepare for data acquisition to the disk.

xv. In the lower righthand corner, click on ‘NEW’ to set up for a new sample.

xvi. The top button should say ‘POS’, indicating the instrument is in the positive ion mode. The second button should be toggled to ‘PROF’ to properly observe isotopic patterns in the resulting spectra. Click ‘OK’.

xvii. Click the middle button with the above title of ‘edit filament-on delay time’ and set this time to ‘0 MIN’. Click ‘OK’.

xviii. In the top lefthand corner, change the electron multiplier to run at 950 V. Then, change the filament current to 500 UA. You are now prepared to run a sample.

b. Instrument preparation.

i. On the instrument itself, if the direct insertion probe is currently inside the vacuum chamber, gently twist the circular guard to the left to loosen the grip, and pull the probe to the first stop on the plastic guide.

ii. Press the ‘inlet valve’ button and wait for the ‘cycle’ and ‘open’ lights to turn off.

iii. Gently pull the probe fully out of the vacuum and place it on the rest next to the chamber.

iv. For a single sublimation, a single-looped probe filament is sufficient. If a co-sublimation is necessary, then the single-looped probe filament must be replaced with a double-looped probe filament.

1. To change a filament, obtain a pair of tweezers and gently grasp the white rubber part of the filament and pull. Place this filament in a provided, labeled container.
2. Pick up a new filament with the tweezers and insert it into the probe by aligning the two metal prongs into the two holes in the probe.

v. Once the filament is prepared, load approximately 1 μL of a 0.025 M sample onto the loop using either a micropipette or a graduated syringe.

vi. Place the probe back into the guide in front of the vacuum to the first stop, tighten the wheel to the right, and press the 'inlet valve' button.

vii. Wait for both the green 'cycle' light to illuminate as well as the red 'open' light. The 'open' light will turn on once the ball drops inside the vacuum chamber, which will also make a clicking noise.

viii. The wheel can now be loosened, the probe pushed all of the way into the chamber, and then tightened again.

ix. Return to the computer and find the 'analysis' screen.

x. At the bottom of the screen, type 'start'.
    1. The instrument should automatically turn on as well as the electron current and electron multiplier.

xi. In the guide screen, type 'probe' to observe the probe heating up.

xii. Wait for the full 10 minute scan and ensure that the instrument is turned off.

xiii. Data can now be viewed under 'QualBrowser' under the file name chosen for that sample.

xiv. Repeat the above steps in order to run subsequent samples.

II. Collision Induced Dissociation Analysis

a. Begin by clicking 'OLD MAIN' in the 'GUIDE' window

i. Click 'SCAN'

ii. Click 'DAU' for daughter scan mode

1. Click 'PARENT' and select a new parent mass (i.e. the fragment to be selected and analyzed from the first quadripole).

2. Enter that value in the box and click 'OK'.

b. In the 'VALVE' window, the 'X' labeled '8' will be illuminated in yellow, indicating that the collision gas chamber is open.

i. Before beginning analysis, double click the 'X' labeled '9' and wait at least 30 seconds.

1. This action backflushes any residual collision gas or atmospheric gas from the inside of the chamber, only allowing the collision gas of interest to be present in the cell.

ii. Double click the 'X' labeled '8' again to close the forepump valve and re-open the collision cell chamber.

c. Type ‘ANALYSIS’ in the ‘VALVE’ window.

    i. Click ‘FILE’ in the upper lefthand corner.

        1. Enter an appropriate file name and click ‘OPEN’.

d. The sample of interest may now be loaded as previously mentioned in Section b of the Quad I Full Scan analysis.

e. Type ‘START’ to begin analysis.

Appendix B

Scanning Electron Microscopy (SEM) and Energy Dispersive Spectroscopy (EDS) Identification of $Pd(tftm)_2$ Formation

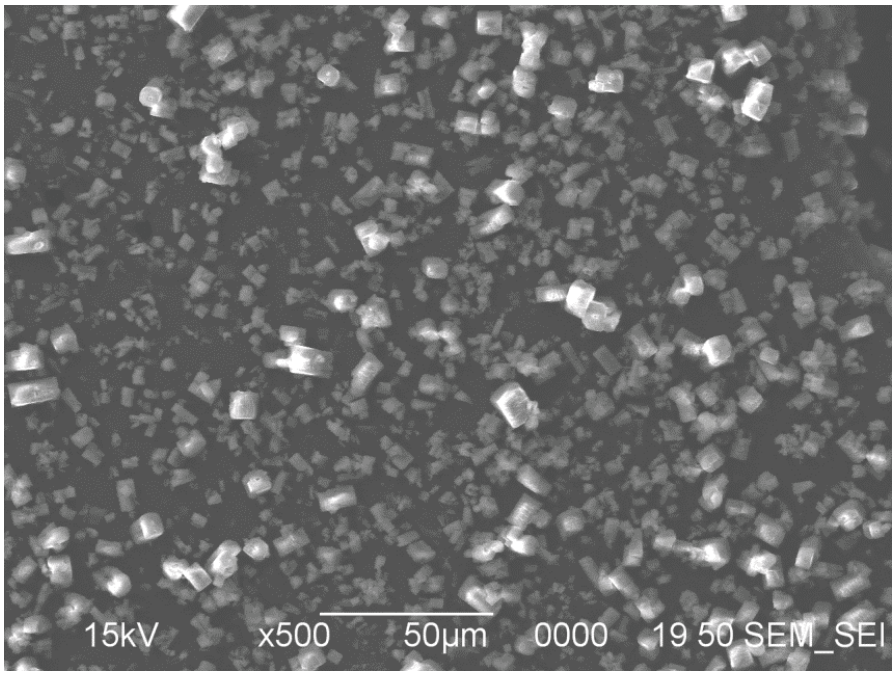

Figure B.1: 15 kV SEM_SEI image of $Pd(tftm)_2$ powder at 500x magnification.

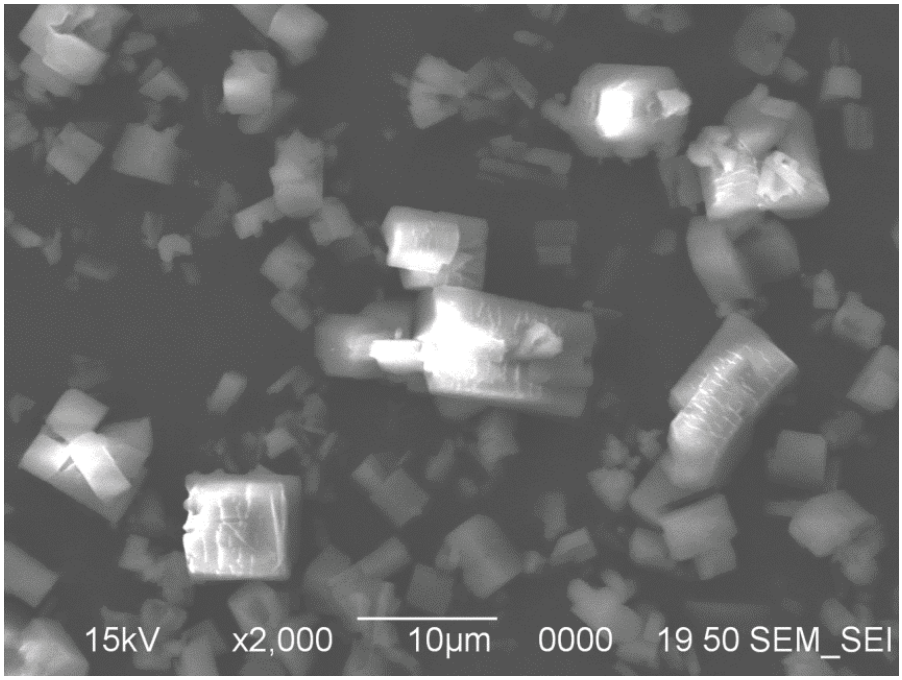

Figure B.2: 15 kV SEM_SEI image of $Pd(tftm)_2$ powder at 2,000x magnification.

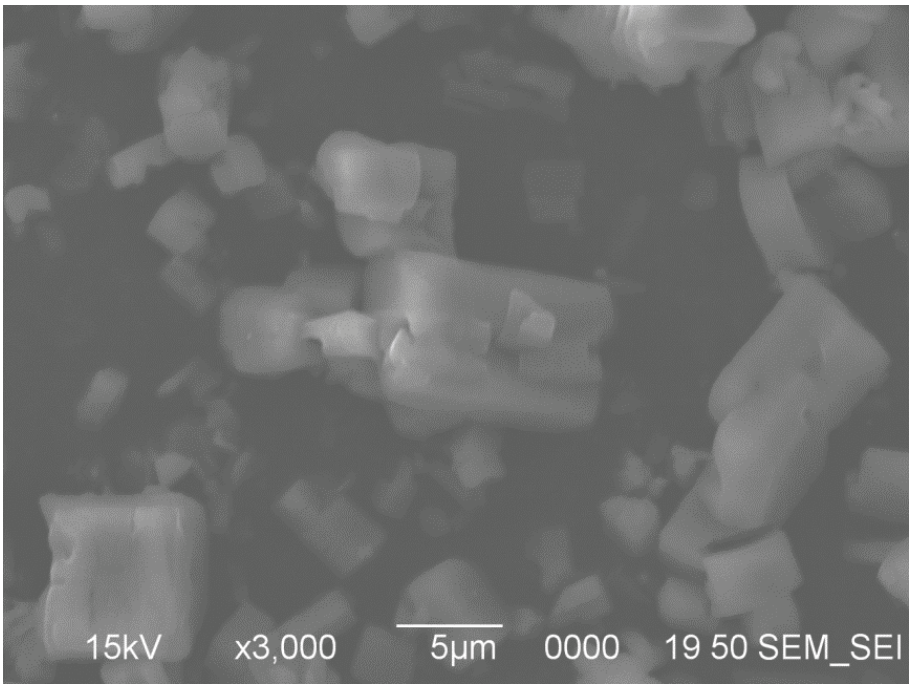

Figure B.3: 15 kV SEM_SEI image of $Pd(tftm)_2$ powder at 3,000x magnification.

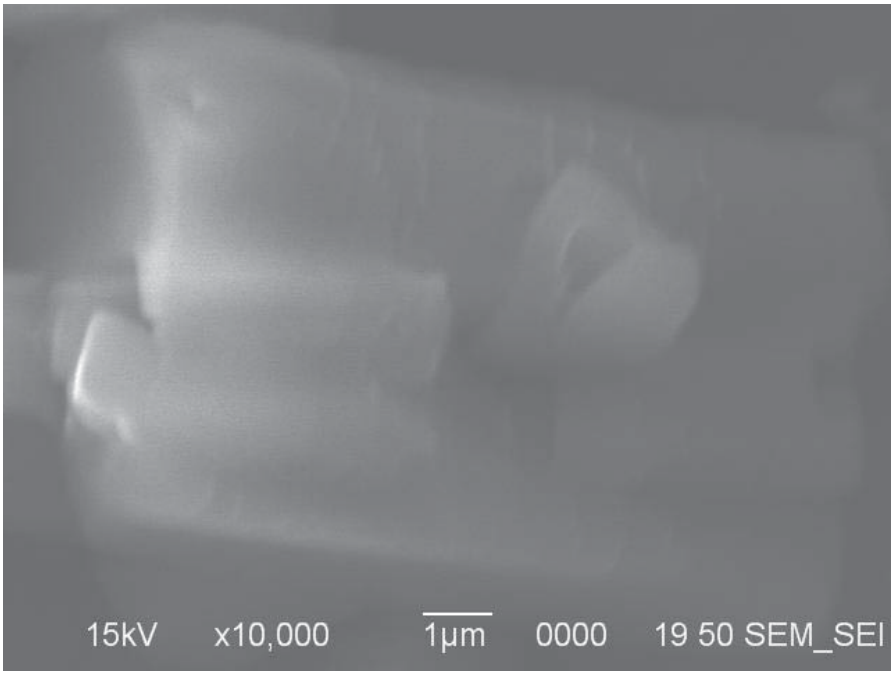

Figure B.4: 15 kV SEM_SEI image of $Pd(tftm)_2$ powder at 10,000x magnification.

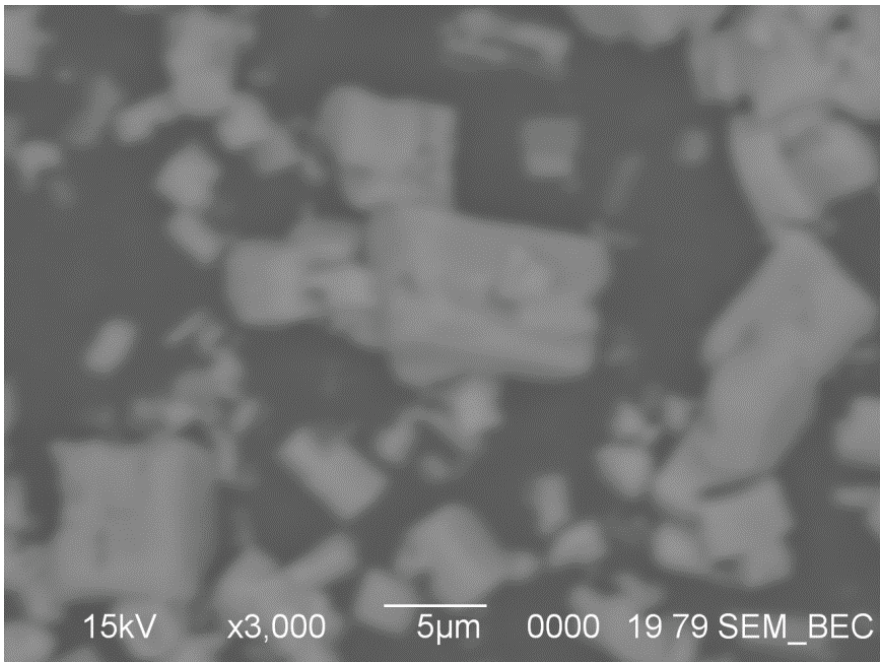

Figure B.5: 15 kV SEM_BEC image of Pd(tftm)2 powder at 3,000x magnification.

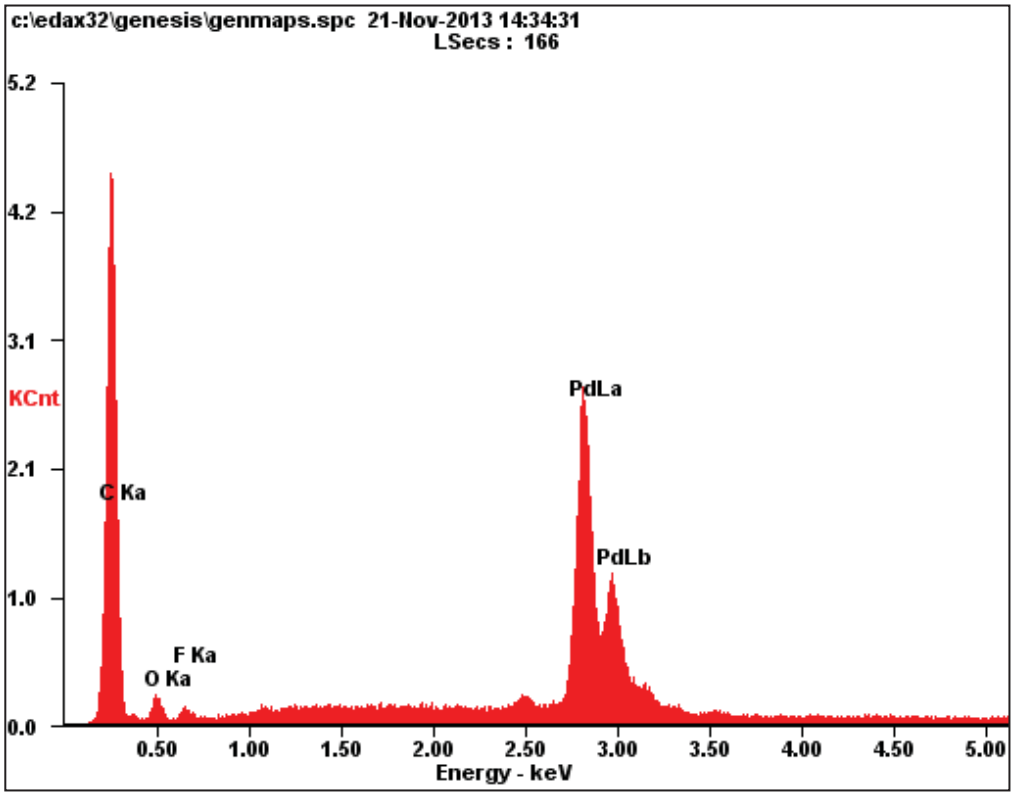

Figure B.6: EDS Spectrum of $Pd(tftm)_2$ chemical composition.

Element	Wt %	At %
CK	39.25	77.29
OK	05.73	08.47
FK	01.97	02.45
PdL	53.05	11.79
Matrix	Correction	ZAF

Table B.1: The weight percentage and atomic percentage of each element in $Pd(tftm)_2$ determined by EDS as presented in Figure B.6.